TENSILE, LOW-CYCLE FATIGUE AND SUBSEQUENT PITTING CORROSION BEHAVIOUR OF SS 304L STEEL

A thesis submitted in partial fulfilment of the requirements for the award of the degree of

Master of Technology in Material Engineering

Faculty of Engineering and Technology
Jadavpur University

Submitted by

AJUTAJIT BHATTACHARYA
Examination Roll No: M4MAT24006
Registration No: 163734 of 2022-23

Under the Guidance of

Dr. Md. Basiruddin Sk.
Assistant Professor
Dept. of Metallurgical and Material Engineering
Jadavpur University, Kolkata-700032

Prof. Pravash Chandra Chakraborti
Dept. of Metallurgical and Material Engineering
Jadavpur University, Kolkata-700032

DEPARTMENT OF METALLURGICAL AND MATERIAL ENGINEERING
FACULTY OF ENGINEERING AND TECHNOLOGY
JADAVPUR UNIVERSITY
KOLKATA
May 2024

DEDICATED

TO MY BELOVED PARENTS AND SISTER

CERTIFICATE

This is to certify that the thesis titled "**TENSILE, LOW CYCLE FATIGUE AND SUBSEQUENT PITTING CORROSION BEHAVIOUR OF SS 304L STEEL**" has been carried out by **Mr. Ajutajit Bhattacharya (Class Roll No: 002211303007 and Registration No: 163734 of 2022-23)** under our guidance and supervision and accepted in partial fulfilment for the degree of Master of Technology in Material Engineering from the Department of Metallurgical and Material Engineering of Jadavpur University. To the best of our knowledge the contents of this thesis or any parts thereof have not been previously submitted for the award of any degree.

……..
Supervisor
Dr. Md. Basiruddin Sk.
Assistant Professor,
Department of Metallurgical and Material Engineering
Jadavpur University,
Kolkata-700032

……..
Co-Supervisor
Prof. Pravash Chandra Chakraborti
Professor,
Department of Metallurgical and Material Engineering
Jadavpur University,
Kolkata-700032

……..
Head of the Department
Dr. Sathi Banerjee
Department of Metallurgical and Material Engineering
Jadavpur University,
Kolkata-700032

……..
DEAN
Faculty of Engineering and Technology
Jadavpur University,
Kolkata-700032

DECLARATION OF ORIGINALITY AND COMPLIANCE OF ACADEMIC ETHICS

I hereby declare that the thesis "**Tensile, Low Cycle Fatigue and subsequent Pitting Corrosion behaviour of SS 304L**" contains literature survey and original research work that has been carried out by myself, as a part of my Master of Technology Degree in Material Engineering during the academic year 2022-2024. All the information in this document has been obtained and presented in accordance with academic rules and ethical conduct. As per the rules and regulations I also declare that, I have fully cited all the reference materials and given due credit to their respective authors for any data or information that are not original to this work.

Name: Ajutajit Bhattacharya
Class Roll No: 002211303007
Registration No: 163734 of 2022-23

Thesis Title: **Tensile, Low Cycle Fatigue and subsequent Pitting Corrosion behaviour of SS 304L**

Place: Kolkata
Date: Signature

CERTIFICATE OF APPROVAL

*The foregoing thesis, entitled as "**Tensile, Low Cycle Fatigue and subsequent Pitting Corrosion behaviour of SS 304L**" is hereby approved by the committee of final examination for evaluation of the thesis as a creditable study of an engineering subject carried out and presented by Mr. Ajutajit Bhattacharya (Registration No: 163734 of 2022-23) in a manner satisfactory to warrant its acceptance as a prerequisite to the degree of Master of Technology in Material Engineering. It is understood that by this approval, the undersigned do not necessarily endorse or approve any statement made, opinion expressed, or conclusion drawn therein, but approve the thesis only for the purpose for which it is submitted.*

Committee of final examination for evaluation of thesis –

…….. ……..

…….. ……..

ACKNOWLEDGEMENT

I would like to take this opportunity to express my heartfelt gratitude to the people who have supported me throughout this research project. I owe a deep sense of gratitude and reverence to my respected thesis supervisor(s) ***Dr. Md. Basiruddin Sk****, Assistant Professor, Department of Metallurgical and Material Engineering, Jadavpur University and* ***Prof. Pravash Chandra Chakraborti****, Professor, Department of Metallurgical and Material Engineering, Jadavpur University for their esteemed guidance and encouragement throughout this work. Without their generous support and motivation this endeavour would not have been successful. It was a great privilege and experience to work under them.*

I am greatly indebted to ***Dr. Sathi Banerjee****, Head of the Department of Metallurgical and Material Engineering, Jadavpur University for providing me with the facilities and support during the course of investigation.*

I am also thankful to all the faculty members, Research Scholars, and my peers at the Department of Metallurgical and Material Engineering, Jadavpur University who have provided me their moral support, help and cooperation throughout the duration of this project.

I also express my heartiest gratitude and acknowledgement to my parents and sister for being a constant source of motivation and encouragement, without their guidance my journey would have been incomplete. Finally, I take this occasion to thank all my friends and classmates who have accompanied me throughout this journey and have devoted their precious time in providing me with valuable suggestions.

*Above all, I thank '****God Almighty****' for providing me with mental fortitude, perseverance, determination without which this work would have certainly been incomplete.*

Date: ……..

Ajutajit Bhattacharya
Department of Metallurgical and Material Engineering
Jadavpur University, Kolkata-700032

CONTENTS

ABSTRACT

In this study, monotonic and cyclic deformation of 304L steel were carried out at room temperature and the results suggested that there was a strong correlation between deformation induced martensite formation and the amount of deformation that was applied in terms of prestrain or strain amplitude values. Analysis of the stress strain hysteresis loops revealed that the steel deviated from ideal masing behavior, especially at higher strain amplitudes. Evaluation of the cyclic stress response unveiled that significant secondary hardening took place at strain amplitude levels of $\pm 0.5\%$ and above. A bilinear nature of the cyclic stress strain curve was obtained, implying that the deformation mechanism changed for specimens which were cycled at strain amplitudes higher than $\pm 0.5\%$. Furthermore, subsequent pitting corrosion tests performed on the prestrained or precycled specimens revealed a distinct pattern in the variation of pitting potential values with the amount martensite that formed at that level of prestrain or strain amplitude of cycling.

Keywords: *Deformation Induced Martensite, Secondary hardening, Cyclic stress strain curve, Masing behavior, Pitting corrosion*

Chapter 1

Introduction

Stainless steels are one of the most versatile materials that are used across the globe today. Various types of stainless steels possess their unique combination of mechanical properties such as strength, ductility and toughness that make them suitable candidates for various applications starting from their use as structural members in buildings, construction and housing to critical applications such as fast breeder nuclear reactors, heat transport piping systems, boilers, reactor vessels, heat exchangers, condenser tubes etc. where constant thermal fluctuations, extreme temperature conditions and high thermomechanical stresses prevail.

Apart from having desirable mechanical properties, stainless steels possess excellent corrosion resistance which prevents them from environmental attack and degradation, making them suitable for use in hostile and reactive environments. The material response of these materials is of vital importance especially for forming operations such as forging, rolling, extrusion etc in which compressive loads are applied to shape the final products from metal ingots. The calculation of the load and the power consumption in production units are all intimately linked to the stress response and work hardening characteristics of these materials under load at various strain rates along with the extent to which these materials can be deformed.

It is therefore necessary to carry out a systematic study in order to understand the mechanical and corrosion properties of these materials under various conditions to find their suitability in real world applications.

The current study focuses on the tensile and cyclic deformation behavior of stainless steel 304L at room temperature including its tensile properties, work hardening behavior, cyclic stress response, masing characteristics, etc.

Additionally, the role of deformation induced martensite, and its effect on tensile, fatigue and pitting characteristics have been studied in detail, and attempts have been made to correlate this effect with the cyclic stress response, the work hardening behavior and the pitting corrosion resistance of the steel under ambient conditions.

Chapter 2

Literature review

Stainless steels are high alloy steels having excellent corrosion and oxidation resistance combined with good ductility and strength. They are extremely versatile and are almost ubiquitous in application, being used in critical applications like nuclear power plants, power generating units and substations ,food processing units, paper manufacturing plants, petrochemical industries, automobile industries, and most importantly as a structural material for building and construction.

2.1 Classification of stainless steels

Stainless steels may be categorized into four main groups, they are as follows --Ferritic stainless steels, Martensitic and precipitation hardening stainless steels, Austenitic stainless steels and Duplex stainless steels.

i) Ferritic stainless steels: The standard ferritic grades are alloyed with chromium (11.2–19%), but contain minute or little to no amount of nickel [1]. These steels are often much cheaper than their high Ni counterparts and does not suffer from price volatility . Often the addition of Molybdenum improves the corrosion resistance, while alloying with niobium and/or titanium improves its weldability. The ferritic grades are magnetic due to their ferritic microstructure.

In addition to these grades, certain grades of ferritic stainless steels are used in high temperatures in the temperature range of 800^0C -1150^0 C in Sulphur containing atmospheres. These grades typically contain more carbon to increase its creep strength and are often alloyed with Si and Al to impart oxidation resistance.

ii) Martensitic and precipitation hardening stainless steels: The martensitic grades have higher carbon content in comparison to other grades, thereby having improved strength and hardenability. These grades too contain sparse quantities of nickel. And although addition of Nitrogen further accentuates strength, a major drawback of these grades is their poor weldability, which may be improved by addition of Ni or by reducing the percentage of carbon , but not without comprising its strength. Addition of Sulphur is found to improve machinability. These steels are air hardenable allowing for their final microstructure to be predominantly martensitic due to the 'nose' of the TTT diagram being shifted to longer times.

iii) Duplex stainless steels: Duplex stainless steels are formed by extending the narrow $\alpha+\gamma$ region surrounding the closed gamma loop illustrated in the Fe-Cr phase diagram in **Fig 2.1**. This can be achieved through the addition of various alloying elements in optimum proportions so that a proper balance is maintained between the α stabilizing and the γ stabilizing elements and the final microstructure at room temperature contains equal volume fractions of ferrite and austenite.

Duplex grades therefore combine many of the beneficial properties of ferritic and austenitic stainless steels. The high strength and high resistance to stress corrosion cracking are attributed to the dual phase microstructure. Duplex stainless steels have high chromium content (20.1–25.4%), but low nickel content (1.4–7%) in comparison to the austenitic grades. Molybdenum (0.3–4%) and nitrogen are often added to improve the corrosion resistance and to stabilize the microstructure. Manganese added in some grades, not only serves as a replacement for nickel, but also increases the solubility of nitrogen in the matrix.

Owing to their dual phased microstructure, these steels have superior mechanical strength, toughness and corrosion resistance in comparison to their single phase counter parts. Though these steels have a host of desirable properties they are not without flaws as the usage of these steels is restricted to temperatures above 280^0 C due to the precipitation of sigma and chi phases which severely impair their ductility and performance at lower temperatures.

Duplex stainless steels along with martensitic and ferritic stainless steels also undergo a phenomenon commonly referred to as the 475 ℃ embrittlement. This implies that these steels suffer a drastic decrease in toughness and are embrittled when they are exposed, or heat treated in the temperature range of 400℃ to 500℃. Believed to be the result of a spinoidal decomposition transformation, fine chromium rich precipitates of α' phase are formed which deteriorates the toughness property in these steels [2]. The miscibility gap encountered in the Fe-Cr system **Fig 1** drives this transformation and transformation is facilitated when chromium is present in large quantities (15-75wt.%).

Miscibility gaps like these arise from the fact that a single phase is not stable at that temperature owing to the convex-concave or undulating nature of its free energy vs composition curve. As a result, for certain alloy compositions the parent phase splits into two phases of different compositions.

iv) Austenitic stainless steels are the most widely used stainless steels, accounting for more than 50% of the global stainless steel production The austenitic grades may be divided into five sub-categories, Cr-Mn grades, Cr-Ni grades, Cr-Ni-Mo grades, high performance austenitic grades and high temperature austenitic grades. The austenitic grades bring in a plethora of desirable properties from excellent corrosion resistance, to good formability and weldability. They also possess good impact strength at low temperatures, making them suitable candidates for cryogenic applications[3]. They are non-magnetic in the solution annealed condition due to their austenitic microstructure and do not undergo phase transformation with temperature. Thus, these steels are predominantly strengthened through cold working, which may be followed by stress relief annealing. A characteristic of these steels is when they are heated in the temperature range of 425-870℃ chromium carbide precipitates at the austenitic grain boundaries.

This poses a few a problems, notably the formation of chromium carbide depletes adjacent austenite matrix of chromium, making it susceptible to corrosion. This phenomenon is referred to as sensitization [4][5][6][7] and it can be circumvented or remedied in the following ways:

i) Performing solution annealing heat treatment in the temperature range of 1050^0C-1100^0C effectively dissolves the carbides formed, after holding for a specific period of time the steel is cooled rapidly (quenched) to avoid precipitates from reappearing during the cooling stage.

ii) By using a stainless steel of lower carbon content the chances of precipitate formation automatically reduces, thereby avoiding this issue altogether.

iii) Introduction of elements having higher affinity for carbon than chromium like Ti, Ta etc. results in the preferential formation of carbides of these elements and reduces the likelihood of chromium carbide formation. These are especially used in stabilized austenitic steel grades such as 321 or 347 which aid in mitigating the problem of intergranular corrosion that is very much prevalent in these steels.

iv) Delaying the sensitization time to longer periods by adding elements like Molybdenum which can affect the reaction kinetics of $M_{23}C_6$ carbides.

In addition to chromium carbide, Cr-rich sigma phases are known to precipitate in duplex stainless steels in the temperature range of 700^0C-900^0C. These phases have a detrimental effect on the mechanical properties of such steels and are known cause a precipitous drop in the ductility and toughness values [8][9] along with a significant reduction in general corrosion resistance. The most commonly encountered sigma phase, the Fe-Cr phase has a hardness value of 68 in the Rockwell C scale as reported by Griffith and Bain and is extremely brittle with specimens fracturing during the test itself. [10]

The formation of these intermetallic compounds are further promoted by addition of alloying elements like Si , Ti and Mo .Thus highly alloyed stainless grades are more prone to sigma phase formation.
Sigma phase formation in AISI 300 stainless steels is known to be extremely slow or sluggish, often requiring hundreds or even thousands of hours of holding time at the above temperature range to form.[11]

These steels can thus be used over a broad range of temperatures from cryogenic conditions to elevated temperatures of about 760^0C for working conditions.

Apart from carbides, sigma phases, Ni_3Al or the γ' phase is another intermetallic phase which is encountered in austenitic stainless steels, Ni base alloys and super alloys. This phase has an ordered fcc structure with Ni atoms occupying the face center positions while the Al atoms lie at the corners of the lattice. The γ' phase is known to form in stable austenitic stainless steels such as 20Cr25Ni [12] and particularly those having combined weight percentages of Al and Ti exceeding 1%. Unlike the sigma or laves phases Ni_3Al precipitates are desirable due to the fact that they have similar lattice parameters in comparison to the base matrix and are therefore coherent with it.

2.2 Role of Alloying Elements in Stainless Steels:

A large number of alloying elements may be present in steels and each of them influences the iron-carbon equilibrium phase diagram in their own unique ways. Some of which are discussed as follows:
Alloying elements may be broadly divided into two categories based on the manner in which they influence the equilibrium phase diagram:

Alloying elements that expand the austenite phase field by making the gamma phase stable over a wider range of temperatures and compositions are known as austenite or gamma stabilizers. Alloying elements such as Mn, Ni, Cu belonging to this category all have FCC

(Face Centered Cubic) crystal structure. In addition to shifting the critical points to increase the gamma phase field they also lower the eutectoid temperature as well as the eutectoid composition. A mere 3% addition of Ni is found to decrease the eutectoid temperature by almost 30 ^{0}C.
The other group are the ferrite stabilizers, and their addition reduces or shrinks the austenite phase field. These elements possess a Body Centered Cubic (BCC) crystal structure similar to the ferritic phase of iron. Some common ferrite stabilizers are W,V, Mo, Cr, Si.

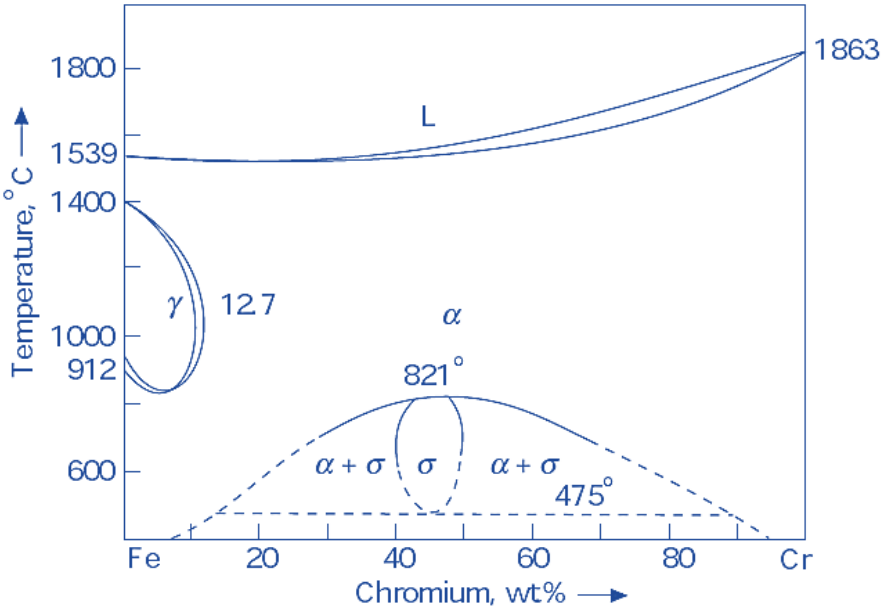

Fig 2.1 ***Fe Cr phase diagram showing the distinctive γ loop*** **[12]**

As is evident from **Fig 2.1**. that an addition of about 12.7 wt.% Cr makes the austenite phase field disappear, the ferritic phase fields of the alpha and delta iron merge to become one continuous phase which remains stable from room temperatures and upto the melting point. Austenitic stainless steels despite having higher percentages of chromium still have austenite as the stable phase due to the effect of alloying with Ni which makes the austenite phase reappear. For instance, when 2% Ni is alloyed with 18% Cr the steel becomes heat treatable, while at still higher percentages austenite is the only stable phase.

The same effect can be observed when over 1 wt.% Ti or 7 wt.% Mo is present.

Addition of nitrogen is known to enhance mechanical properties such as yield strength in austenitic stainless steels [13][14]. Nitrogen is also a much more potent austenite stabilizer and is about as much as twenty times stronger than that of an equivalent amount of Ni [14]. Additionally, Nitrogen improves resistance to creep and fatigue, and is also known to inhibit the formation of strain induced martensite in metastable grades [15][16].

Alloying elements can influence the gamma phase field in the following way:

They may form an i) open γ -field like Mn, Co, Ni, Ru, Rh, Pd, Os, Ir, Pt ii) An expanded γ -field like C, N, Zn, Au iii) Closed γ -field like Be, Al, Si, Ti, V, Cr, Ge, As, ,Mo, Sn, Sb, W and iv) Contracted ϒ-field like B, Nb, Ta, Re. [17]

Carbon and Nitrogen are known to expand the γ -field due to the larger interstitial voids present in FCC structures in comparison to BCC structures. Carbide forming elements like Ti, Cr, Ta having strong affinity for C reduce the γ phase field by significant proportions due to the fact that it is thermodynamically much more favorable for carbon to diffuse out and form alloy carbides rather than remaining the austenite matrix as an interstitial. Many tool steels have a broad γ + carbide phase field due to this reason.

In 18%Cr-8% Ni stainless steels the γ -α phase boundary is reached at 650^{o}C, as a result of which the diffusion of alloying elements which is essential to produce an equilibrium concentration of ferrite is slow and insignificant. Thus, upon air cooling austenite remains as a metastable phase at room temperature.[18]

Certain steels such as Hadfield austenitic manganese steels are cheaper than their Ni containing counterparts and although complete replacement of Ni poses difficulties in hot working these steels containing about 12% Mn and 1%C possess superior toughness and wear resistance properties due to the metastable austenite phase which forms after water quenching from 1000℃. Their remarkable toughness is extensively utilized in railway cross-overs and rock-crushing equipments.

The role of individual alloying elements is briefly discussed as follow:

Chromium: It is one of the chief alloying elements that imparts the property of corrosion resistance in stainless steels. All stainless steels contain a minimum of 10.5 wt.% Cr in order to resist corrosion and to impart improved oxidation resistance property at elevated temperatures.

Nickel : It imparts ductility and toughness to stainless steels, improves weldability in martensitic grades, and forms intermetallic compounds in precipitation hardening grades, causing a substantial increase in strength. However, a downside to Ni addition is that Ni is known to reduce resistance to Stress Corrosion Cracking (SCC) as demonstrated by Copson [19] for an Fe-20Cr alloy in a Cl environment. Ni additions have an effect of reducing the Ductile to Brittle Transition Temperature (DBTT) in high Cr ferritic stainless steels [20].

Molybdenum :It Increases both uniform and localized corrosion resistance in stainless steels. Mo present in austenitic stainless steels provides resistance against pitting corrosion[21], especially in seawater and chloride solutions. Mo also promotes the formation of sigma(σ) [22]and chi (χ) phases in ferritic, austenitic and duplex stainless steels. Mo effectively increases the room temperature yield point and tensile strength in steels while simultaneously improving stress rupture and creep properties in the high temperature regime.

Manganese : Increases hot ductility in stainless steels, increases the solubility of nitrogen in duplex and austenitic stainless steels [23][1], acts as an austenite stabilizer. Mn additions prevent hot shortness, a form of solidification cracking attributed iron sulphide constituents having low melting points or eutectics. Mn having higher affinity for Sulphur than Fe circumvents this problem by forming stable Manganese Sulphide (MnS).

Titanium : Titanium increases the resistance to intergranular corrosion in austenitic stainless steels, improves toughness, formability and corrosion resistance in ferritic grades. It also increases the resistance to tempering and decreases the hardness of the martensite phase in martensitic stainless steels.

Silicon : Silicon improves oxidation resistance at high temperatures and in strongly oxidizing solutions at lower temperatures. It is also known to promote fluidity of molten steels, enabling it to effectively counter the sluggish flow rates in certain steel grades[3]. It also serves as a ferrite former at concentrations exceeding 1wt. %.

Cobalt : Cobalt serves as a solid solution strengthener in steels. It is also known to increase the Martensite Start Temperature (M_s) ,for which it is added in martensitic grades to facilitate martensite formation [24].

Sulphur :Addition of Sulphur along with Lead and Selenium improves the machinability of steel grades, thereby making provision for higher machining speeds as well as improving tool life.

Carbon : Carbon is present as an interstitial element in all steels. A higher percentage of carbon is known to widen the closed γ loop that is typically seen when alloying elements like chromium are present. Thus carbon ,like nitrogen is an austenite stabilizer. Fully austenitic microstructures are possible at room temperature when carbon is present in excess of 0.4wt.% for commonly encountered stainless steels containing 18 wt.% Cr. Another important effect of carbon is to form carbides[25]. Higher carbon percentages significantly increases strength while reducing ductility and toughness in both ferritic and martensitic stainless steels. Higher carbon percentages also poses the risk of intergranular corrosion.
Based on the extent to which important alloying elements influence the formation of different phases in stainless steels a diagram known as the Schaeffler diagram can be constructed which

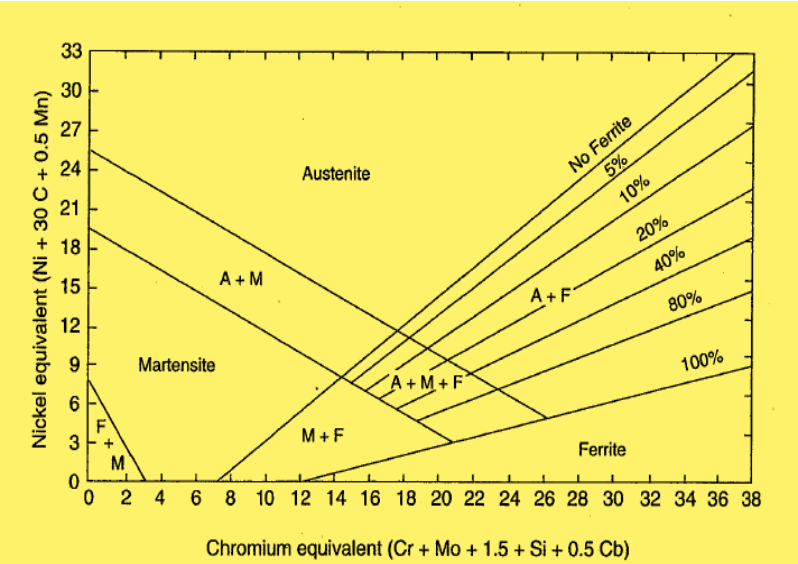

Fig 2.2 *Schaeffler diagram* (1949) [25]

indicates the stable phase(s) which would be present for a stainless steel of a given composition at room temperature.

It may be noted from **Fig 1.2** that while the diagram is solely based on the Nickel and Chromium equivalents[3], the role of important alloying elements are accounted for while calculating their values. This is based on the premise that most alloying elements behave either akin to Ni or Cr in stabilizing one phase or the other.

Other elements: Elements such as Tungsten present in duplex stainless grades impart resistance against pitting corrosion. Al may be present in certain low chromium ferritic grades for improving the general corrosion resistance.

Al along with Cu, Ti and Mo are present in precipitation-hardenable (PH) grades to form precipitates. Certain martensitic grades are known to possess yield strengths in excess of 1375 MPa at room temperature as a result of these additions[3]. Austenitic stainless steel grades that are precipitation hardenable are usually alloyed with Al or Ti in order to obtain coherent Ni_3Al and Ni_3Ti precipitates similar to those encountered in Ni base superalloys. Cu precipitates in pure form also provide hardenability in martensite steel grades such as 17-4PH.

The alloying elements present in steel may be further classified as i) carbide forming elements such as Cr, Mn, Mo, W, V, Ti, Zr which are capable of forming stable carbides in steels and ii) non-carbide forming elements such as Ni, Si, Co, Al, Cu, N which do not demonstrate carbide formation. The elements belonging to the latter category that do not form carbides does not interfere with cementite formation as a consequence of which the microstructure remains unaltered. In the former category cementite is replaced by alloy carbides of Mo, Cr, W, and even more so in presence of Nb, Ti and V with alloy carbides forming preferentially with as low as 0.1wt.% concentration of these elements.

It has been found that the stability of alloy carbides decreases on traversing from left to right of the periodic table, with elements like Ti which lie towards the beginning of a long period tending to form very stable carbides of the form MC.

MC carbides like TiC and NbC form fine dispersions and this property is ingeniously exploited in dispersion strengthened austenitic stainless steels (grades 321 and 347) enabling them to retain high strength at temperatures in excess of 500℃. These carbide dispersions also provide creep resistance in some grades of austenitic stainless steels, making them suitable for high temperature applications.

2.3 Mechanical Properties of Austenitic Stainless Steels

Austenitic stainless steels have good work hardening capabilities along with the fact that they also possess substantial ductility, with elongations exceeding 50%. They have yield strengths of around 250 MPa (0.3% proof strength) and their tensile strengths lie in the range of 500-600MPa depending upon the composition gradient.

These steels have UTS to YS ratios in excess of 1.4, indicating that they undergo cyclic hardening. A general criterion is that a ratio greater than 1.4 indicates cyclic hardening, a range of 1.2 to 1.4 indicates no significant changes in hardness values while a value of 1.2 or less dictates that the material would undergo cyclic softening. Usually a high UTS to YS ratio or a low value of yield ratio is desirable since the material would then be expected to have good formability on account of the large uniform deformation that it would undergo before reaching the UTS which corresponds to the point of tensile instability.

Several empirical relationships developed by *Pickering* [26] and *Irvine* [27] illustrate the dependency of tensile properties on the microstructural constituents of austenitic stainless steels.

Two important relationships are given as follows:
0.2% proof strength
$=15.4\{4.4+23C+1.3Si+0.24Cr+0.94Mo+1.2V+0.29W+2.6Nb+1.7Ti+0.82Al+32N+0.16(\delta\text{-ferrite})+0.46\, d^{-1/2}\}$ (2.1)
Tensile strength
$=15.4\{29+35C+2.4Si+1.2Mo+5Nb+3Ti+1.2Al+55N+0.14(\delta\text{-ferrite})+0.11Ni+0.82\, t^{-1/2}\}$ (2.2)

where the element symbols represent their weight percentages
d = mean linear intercept of grain diameter
t = twin spacing
The equations clearly emphasize that both the tensile strength and the 0.2% offset yield strength increases with increase in carbon percentage.

It has been observed that interstitial solutes like carbon and nitrogen impart the greatest solid solution strengthening effect in steels leading to a marked increase in both the yield strength and the UTS as is evident from the high coefficient values of carbon and nitrogen in both the equations. Their strengthening effect is superior to that of the ferrite forming substitutional solutes such as Mo, V, W. While austenite forming elements like Ni, Mn, Cu have very little influence or contribution towards enhancing strength through solid solution strengthening.
Austenitic stainless steels have a propensity to form martensite when the parent austenite phase is deformed below the M_d temperature, which is defined as the maximum temperature below which martensitic transformation can occur as the steel is plastically deformed. As a matter of fact, higher concentrations of alloying elements depresses both the Ms and the M_d temperatures. The M_S and M_{d30} temperatures are given by the following empirical relationships

$Ms = 502 - 810C - 1230N - 13Mn - 30Ni - 12Cr - 54Cu - 46Mo$ (Pickering's formula) [28] (2.3)

$Md,30 = 413 - 462(C+N) - 9.2Si - 8.1Mn - 13.7Cr - 9.5Ni - 18.5Mo$ (Angel's formula) [29] (2.4)

The strain induced transformation of martensite significantly influences the mechanical properties in austenitic stainless steels. Some well-known consequences of a such transformation are secondary hardening during completely reversed low cycle fatigue tests, increase in UTS with increasing in strain rate, accompanied by a decrease in total elongation, and improvement of fatigue life in cases where secondary hardening had occurred.

2.4 General Deformation Behaviour of fcc metals

Tensile Behavior of fcc metals is found to progress through three distinct stages. In stage I, as the shear stress value reaches the critical resolved shear stress value, slip occurs in the most favorably oriented planes. The first stage is characterized by the easy glide of dislocations in which dislocations can move over relatively large distances unhindered. Only a single slip system, particularly the one with the highest Schimdt factor becomes operative at this stage.

In stage II slip activates on multiple slip systems owing to the large number (12 in total) of slip systems in fcc crystals the phenomenon of double glide or duplex slip is frequently encountered. As the tensile axis remains fixed, the slip planes unable to glide freely, rotate

around the tensile axis and eventually reach a stage during which multiple slip systems become active. This in turn results in the formation of Lomer-Cottrell barriers on intersecting {111} planes which impedes dislocation motion, causing them to pile up .This causes the material to strain harden rapidly and the stress strain curve rises. Duplex slip is common in fcc metals where two separate slip systems become active. One example commonly encountered in literature is when the tensile axis lies inside the unit triangle defined by the [001]-[$\bar{1}$11]-[011] directions in the stereographic projection of the crystal normal to the (001) plane. As the specimen elongates, due to the rotation of the slip planes the tensile axis reaches the [011]-[$\bar{1}$11] boundary. Thereafter the conjugate slip system ($\bar{1}\bar{1}$1)[011] becomes active in addition to the primary slip system (111)[$\bar{1}$01] as conditions for slip become favorable in both these systems and duplex slip occurs [30]. In general, stage-II is dependent on the orientation of the single crystal and remains unaffected by other variables.

In stage III the strain hardening rate decreases and dynamic recovery occurs due to the high stresses which aid in the cross-slip of dislocations which are piled up at the barriers [30]. Thus, the internal stress field resulting from dislocation pileups is severely reduced. Several authors have reported the temperature dependence of the stress at which stage III commences. In metals like Aluminium the stage II is relatively short, this is attributed to its high stacking fault energy (SFE ~ 200 mJ m^{-2}) which promotes easy cross-slip, thereby reducing dislocation pileups.

2.5 Tensile behavior of stainless steels

The tensile behaviour of austenitic stainless steel is influenced by the strain rate, prior history of cold work and the temperature at which the test is performed. The tensile test parameters such as the Ultimate Tensile Strength (UTS), percentage elongation in length (%EL) the percentage reduction in area (%RA) are all influenced by the aforementioned parameters up to a certain degree. Although tensile tests are performed at strain rates of the order of 1x 10^{-5} to 1 x10^{-1} s^{-1} which is sufficiently less to be considered as quasi-static as has been noted by many, owing to the poor thermal conductivity of austenitic stainless steels a major portion of the heat of deformation is retained inside the material, yielding similar results.

The flow stress in tension strongly depends upon the strain rate at which the test is conducted and the testing temperature. A closely related parameter is the strain rate sensitivity of a material which describes the material's behavioural response to strain rate. The flow stress usually bears a power-law relationship with strain rate which may be represented as $\sigma = C(\dot{\epsilon})^m$, this relationship is obtained from the tensile plots of the material at different strain rates at a particular temperature. The flow stress corresponding to a particular strain is then plotted on a logarithmic scale the slope of which gives the value of n. Strain rate sensitivity values can be readily determined from strain rate change tests.

The strain rate sensitivity values are indicative of the deformation behaviour of a material as a direct relationship can be established between its values and the exponent of the true stress-dislocation velocity relationship given by $v = A\sigma^{m'}$ [30].The strain rate is directly related to the dislocation velocity as $\dot{\epsilon} = \boldsymbol{b}\rho v$, where, $\boldsymbol{b}$ is the Burgers vector of the crystal lattice, ρ is the density of mobile dislocations and v is the dislocation velocity.
Clearly, the relationship $m' = \frac{1}{m} - \frac{\partial ln\rho}{\partial ln\sigma}$ may be established between the two. If the mobile dislocation density is assumed to remain constant with increasing stress, the relation simplifies to $m' = \frac{1}{m}$.

The value of strain rate sensitivity is low < 0.1 for steels and other metals at room temperature and may increase or decrease with increasing temperature as have been noted by many [30].

2.5.1 Effect of temperature on tensile behaviour:

It has been demonstrated that for austenitic stainless steels the nature of the stress strain curve changes as the test temperature is varied from room temperature to all the way down to cryogenic values . Room temperature tensile tests display curves of a parabolic nature , but at increasingly lower temperatures sigmoidal (S-shaped) curves begin to form [31] . These curves possess a plateau region characterized by easy deformation , at low strain values. According to Gunter and Reed [32] ε-martensite , bearing an orientational relationship of (111) γ//(00.1) ε forms in this region due to the low stacking fault energy of the austenite matrix. In contrast to this at higher strains, rapid strain hardening is observed that stems from α-martensite formation.

Decreasing the test temperature has an effect of increasing the yield strength and UTS while simultaneously reducing the elongation at fracture in ASS. Cryogenic tensile tests conducted by Zheng and Yu [33] on SS 304 in the temperature range of 20K to 77K have shown a marked increase in both the YS and UTS values in this temperature range. The primary reason for such an abrupt increase lies in the Martensite start (Ms) temperature of ASS which is around 110K. Reaching this temperature almost immediately leads to an athermal transformation of austenite to martensite. However a distinction is to be made in this regard, as this transformation occurs prior to the test, as considerable time is needed for the specimen to cool down to sub-zero temperatures before the test is commenced ,and it is during this period that martensitic transformation takes place as opposed to DIM which forms during the course of the test. The Ms temperature which is crucial for the transformation to occur is sensitive to the chemical composition of the steel in question and is empirically expressed as 546exp (- 1.362C) -30.4Mn 17.7Ni -12.1Cr -11Si, where the element symbols are representative of their corresponding weight percentages. [33]

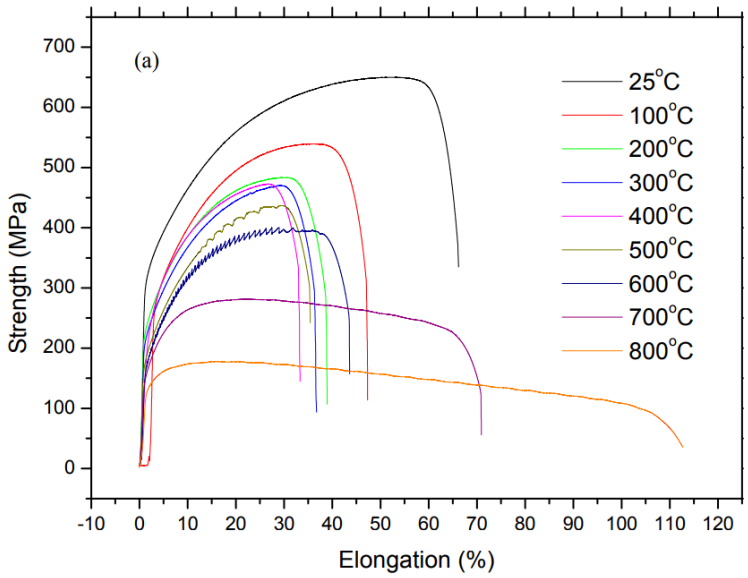

Fig 2.3 ***Tensile curves of 316L austenitic stainless steel showing DSA phenomenon (serrated flow behaviour) at 500***℃ ***and 600***℃ **[34]**

2.5.2 Dynamic Strain Aging in stainless steels

DSA refers to the appearance of serrations at elevated temperatures in the tensile curves of certain metals or alloys such as plain carbon steels, HSLA steels and stainless steels notably of 316 and 304 types.
Serrated flow at elevated temperatures is the result of interaction between solute atoms and dislocations. At sufficiently high temperatures, due to their higher diffusivity and effectively small size ,solute atoms such as C and N, are able to catch up with mobile dislocations. Upon encountering a dislocation they successfully 'pin' it by condensing into the high energy dislocation core [35]. This 'pinning' of dislocations is overcome when the local shear stress barrier is surmounted and the dislocations are subsequently torn away from the impeding solute atoms. This process continues, resulting in the pinning and unpinning of dislocations and this is in principle what causes local peaks or humps to appear in their flow curves.

2.5.3 Deformation induced martensite (DIM) formation

It has been well established that in some grades of austenite stainless steels the metastable austenite matrix phase changes to the Body Centered Cubic (BCC) α'-martensite phase on plastic deformation. Results have shown that with increased plastic deformation the volume fraction of martensite phase increases, influencing mechanical properties such as the tensile strength, the yield strength and the ductility of the material. Martensite being a hard phase increases the work hardening capability and the tensile strength of the material, though its hardness primarily depends on the percentage of carbon present in the steel as an interstitial. Experiments have shown that with increase in strain rate the volume fraction of martensite decreases, many researchers have rationalized this phenomenon based on the premise that an increased strain rate leads to greater adiabatic heating inside the material followed by a substantial increase in temperature which inevitably lowers the volume fraction of martensite formed due to deformation [36].

The transformation to α'-martensite can either proceed directly or indirectly via a transitional phase as has been discussed below-

The presence of elements such as Mn lowers the stacking fault energy of the austenite base matrix. In such cases ε-martensite having hcp crystal structure forms as an intermediate phase owing to the lowering of stacking fault energy (SFE) of the alloy. The low SFE of the fcc matrix phase in essence makes it energetically closer to an alternate hcp structure, as a result of which it becomes easier for ε-martensite to nucleate first as an intermediate phase followed by the eventual formation of α'martensite. This intermediate phase forms as parallel plates and is often misinterpreted as annealing twins which are also commonly encountered in these in steels. However, several authors [37] have reported that γ - α' transformation with ε-martensite forming as an intermediate phase is favoured only when the SFE of the base matrix is $<$ 18mJ/m^2. Whereas SFE values $>$ 18mJ/m^2 seem to favour direct transformation of γ to α'.

TEM studies on austenitic stainless steels show that the α'-phase preferentially nucleates at shear bands, shear band intersections, twin boundaries and grain boundaries.

According to Brooks [38], in low carbon austenitic stainless steels such as 304L martensite can form directly from dislocation pileups on $\{111\}\gamma$ slip planes.

Others have speculated that initially ε-martensite forms from intrinsic stacking faults, however with continued deformation this transformation comes to a halt and all the ε-martensite being formed gets completely consumed at relatively low strains. Thereafter direct transformation from γ to α' takes place at high strain levels.

Hecker [39] has shown that in case of a monotonically loaded specimen, the number of shear band intersections increase with an increase in strain rate. While this intuitively suggests that martensite formation should increase with strain rate, in reality this effect only dominates for strain values of 25% or less. Thereafter adiabatic heating suppresses this transformation by increasing the austenite stability.

Other studies have found that the flow stress varies linearly with the square root of the α'phase content [40]. It is well known that the flow stress bears a similar relationship with the dislocation density which remains unaltered even when martensitic transformation occurs. Researchers have therefore come to the logical conclusion that formation of strain induced martensite causes dislocations to accumulate in the austenite phase on account of which the flow stress increases.

Interestingly, there exists a critical martensite volume fraction of 0.3 beyond which the slope of the line representing the variation of true stress with the square root of martensite phase fraction changes abruptly, indicating that the mechanism by which the flow stress interacts with martensite formation changes. This change has been explained on the basis of percolation theory [40].

The extent to which martensite forms is not only dependent on the strain rate, SFE or temperature but also depends on the mode of deformation. Experiments conducted on 304 stainless steels by Iwamoto and his co-workers [40] have shown that the volume fraction of martensite in compression was higher than that of tension during the initial stages of deformation but the trend reversed at higher strain values.

Hecker [39] also found that balanced biaxial tensile tests yielded more martensite in AISI 304 stainless steels than what was obtained during uniaxial tensile tests.

Existing literature and published experimental results of low cycle fatigue tests conducted on austenitic stainless steels highlight that the percentage of martensite being formed due to deformation increases with an increase in strain amplitude. Raman and Padmanabhan [42] have reported that a linear relationship exists between the volume fraction of martensite being formed and the applied strain amplitude, on the basis of their experimental work on 304LN stainless steels.

2.6 Work hardening behaviour of Austenitic Stainless Steels

Work hardening refers to the increase in flow stress with plastic deformation due to various interactions which hinder the movement of dislocations such as the cutting of dislocation forests, creation of jogs and kinks in dislocation lines, an increase in friction stress resisting the movement of glissile dislocations, dislocation pileups, development of dislocation cell structure etc. In this context it is clear that plastic deformation introduces several changes to the material microstructure and the material response evolves in accordance with it. Several

work hardening models have been proposed in order to capture the material behavior during plastic deformation. A few of them are discussed as follows:

2.6.1 Hollomon relationship

The Hollomon relationship developed by J.H. Hollomon [43] is used to describe the general work hardening behavior of metals. The relationship can be expressed mathematically as

$$\sigma = K(\varepsilon_p)^n \tag{2.5}$$

Where K is the strength coefficient, σ is the true stress, ε_p is the true plastic strain and n is the strain hardening exponent.
This power law relationship when plotted on a double logarithmic scale is yields a straight line whose slope and intercept (when extrapolated) determine the values of n and K respectively.

This relation albeit being simple, is able to predict the plastic flow behaviour of 18-8 stainless steels in a fairly accurate manner. Low and Garofalo [44] have suggested that deviations observed from this behavior are likely due to phase changes occurring with deformation.
It has been well established that for fcc metals and alloys like austenitic stainless steels which possess sufficiently low values of SFE, the Hollomon relationship holds good at high values of plastic strain whereas significant deviation from linearity is observed at low strain values.

Based on this observation alone, Ludwigson [45] modified the Hollomon relation and came up with the expression $\sigma = K_1(\varepsilon)n_1+\exp(K_2+n_2\varepsilon)$ through experimental data fitting. This modified expression delineates the general flow behaviour of low SFE materials. It has been contemplated that the second term of this expression which dominates the flow behaviour at low strain values represents the condition of planar slip which occurs during the early stages of deformation, whereas the first term accounts for cross-slip and cell formation, prevalent at the later stages. The strain at which the deformation behaviour transitions from planar glide to cross slip $\varepsilon_L$is evaluated by setting the ratio of the exponential term to the power term equal to an arbitrary small value r (usually 0.02). This strain value decreases for metals having higher SFE values such as Cu or Ag., until it almost vanishes for Ni or Al, indicating that these materials do not deviate from linearity even at low strains.

Experiments on Austenitic Stainless Steels show that the entire flow behaviour of the material cannot be adequately expressed by a single pair of n and K values. Researchers [46] have identified three different stages in the flow curve for ASS instead, which can be described by three distinct sets of n and K values. There exists a transition region for intermediate strain values, which lie between the high strain and low strain regimes.

2.6.2 Ludwik Analysis

The is yet another empirical relation proposed by Ludwik [47] in order to describe the plastic flow behaviour of metals. While maintaining the same power-law relationship as Hollomon and retaining the same set of parameters n and K, an additional term is introduced into the equation which corresponds to the true value of yield stress. Thus, Ludwik relation takes the form

$$\sigma = \sigma_0 + K(\varepsilon_p)^n \tag{2.6}$$

Direct parallels can be drawn between the ludwigson relation and the Ludwik relation in the sense that both involve an additional term which relates to the stress at which the material starts to yield. For the Ludwigson relation the value of stress at which ε=0 corresponds to the proportional limit and is given by e^{K_2}.Comparison of experimental e^{K_2} values with test records of stainless steels have shown that both are in good agreement with each other.

2.6.3 Kocks-Mecking Analysis:

The hardening behaviour of fcc metals in general, can be portrayed by three distinct stages characterised by the mechanism of deformation. Experiments on Ni and Cu single crystals conducted by Haasen [48] and Seeger [49] have unveiled the nature of flow curve in fcc single crystals, which can be generalised to polycrystals.

The flow stress τ consists of two components τ_S and τ_G, where τ_S represents the contribution due to dislocation cutting processes and is temperature sensitive, while τ_G denotes the stress component arising from elastic interactions between dislocations. It has been established through rigorous experiments that τ_G varies directly with the square root of the dislocation density and is given by the expression $\tau_G = \alpha G b\sqrt{N}$, where G is the shear modulus, b is the burger's vector, N is the dislocation density expressed in cm^{-2}, and α is a constant of the order of 10^{-1}.

The hardening rate expressed by $\theta = d\sigma/d\varepsilon$ is independent of the strain rate and temperature in stage II, but is strongly affected by the orientation of the crystal. In stage II, it is dependent on the extent of stage-I, which usually terminates after secondary slip systems become active. In general, single crystal Θ-σ curves is found to behave as follows, they possess an initial athermal portion in which Θ increases with stress when deformation proceeds via single slip but the reverse is true in case of multiple slip. This is followed by a region of constant hardening which gains prominence at lower temperatures. And finally, stage-III is found to be temperature dependent and approximately follows a linear behaviour.

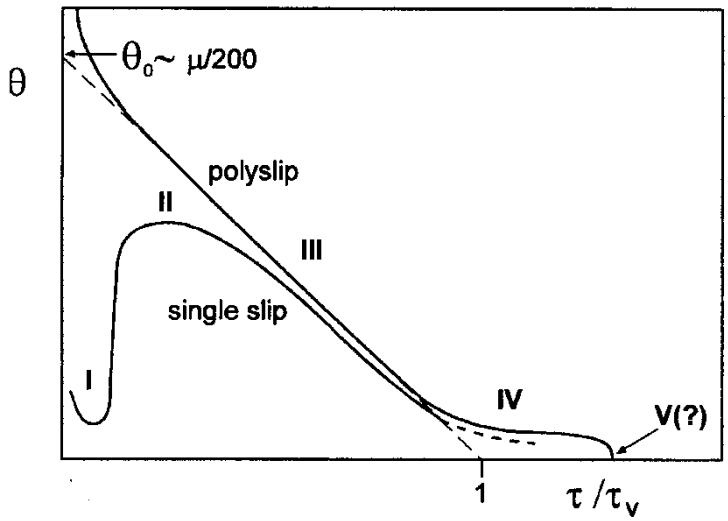

Fig 2.4 Illustration of the different work hardening stages in a polycrystal (upper curve) vs a single crystal (lower curve) **[50]**

For polycrystals the same analogy can be drawn, but the additional effects of grain size and texture (favoured orientation) come into play. Stage-II is absent in polycrystals, and stage-III

behaviour is followed by a stage-IV which is identified by a sharp kink in the Θ-σ curve. According to Rollet [51] this is a characteristic feature of two phase alloys in which the hardening rate further decreases before eventually reaching zero. Although this is true in general, some researchers label stage-IV as linear, and all negative deviations from linearity are attributed to a new stage-V. Steels display this kind of hardening behaviour.
Thus, a plot of Θ-σ (Kocks-Mecking plot) captures the general hardening behaviour of fcc metals.

2.7 Ductile fracture under monotonic deformation

It is well known that fcc metals including austenitic stainless steels fail through ductile fracture across a wide spectrum of temperatures (including at ambient conditions). Ductile fracture involves three distinct events commencing with microvoid nucleation, void growth and void coalescence to form a crack, before finally ending in fracture [52]. Voids are known to nucleate at precipitates, inclusions, second phase particles, shear bands, or even at dislocation pileups.
The mechanism of void nucleation may involve the decohesion of second phase particles or the shearing of particles depending on the particle size, volume fraction, and interfacial bond strength [53].

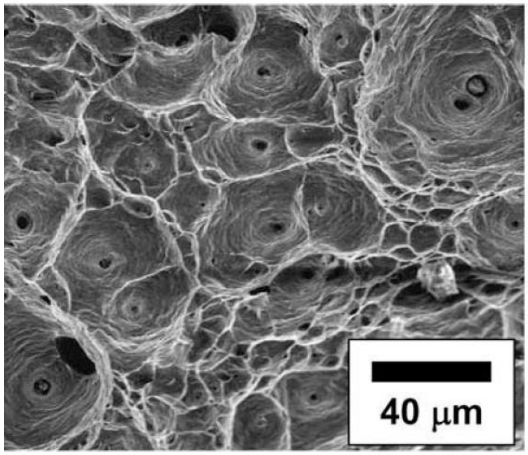

Fig 2.5 ***Tensile fracture surface of SS 304LN tested at a strain rate of*** $\mathbf{10^{-4}s^{-1}}$ ***at 285***℃**. [54]**

Das et al. [54] based on his detailed studies on void morphology had found that the diameter of voids appearing on the fracture surface of SS 304LN increased and their number fraction decreased with increasing strain rate.

2.8 Fatigue behaviour of stainless steels

Fatigue refers to the progressive damage that accumulates in a material when it is repeatedly stressed under cyclic loading, eventually leading to failure at nominal stress levels that are lower than the yield strength of the material. Failure due to fatigue occurs abruptly and without any prior warnings, almost always resulting in a brittle type of fracture. Due to the fact that fatigue damage is not easily detected, it has been estimated that fatigue alone is responsible for 90 percent of all mechanical component failures while in service conditions [30].

Fatigue damage occurs under repeated loading and unloading under alternating stress conditions from surface cracks that are initiated at regions of high stress concentrations such as notches, and sharp corners. Microscopic cracks start to propagate when the stress intensity

factor exceeds a threshold value ΔK_{th} with ΔK being defined as, $\Delta K = (\sigma_{max} - \sigma_{min})\sqrt{\pi a}$. Where, a is the initial crack length, and $\sigma_{max} - \sigma_{min}$ is the stress range.
A characteristic feature of fatigue failure are the ring-like beach marks appearing on the fracture surface, that progress inwards from the point of initiation.

Cyclic deformation may proceed under the influence of loads that produce nominal stresses which lie in the elastic region. At these low stress levels fatigue failure occurs after a large number of cycles (>10^5 cycles) and is termed as High Cycle Fatigue (HCF).
Similarly, when these stresses are large enough to produce plastic deformation, the fatigue life of a component is significantly reduced, and fatigue lives of the order of 10^5 cycles or less fall within the category of Low Cycle Fatigue (LCF).
LCF conditions arise due to stresses that are thermal in origin, such as those encountered in nuclear power plants, gas turbines etc. Since these stresses themselves originate from the thermal expansion of metals at high temperatures, LCF is actually associated with cyclic strains rather than cyclic stresses.

2.8.1 Bauschinger effect:

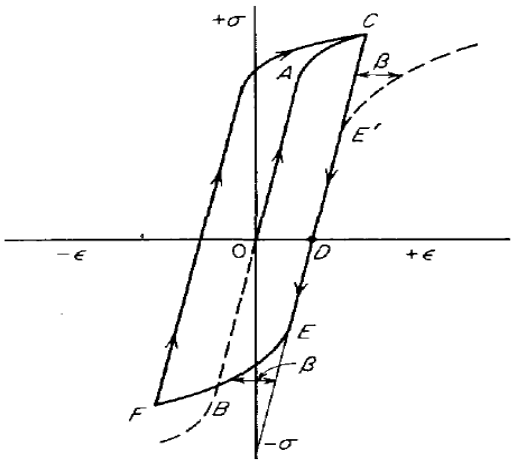

Fig 2.6 ***Bauschinger effect and hysteresis loop (G.E. Dieter)*** **[30]**

Another interesting phenomenon is observed when a material is plastically loaded in tension, followed by which it is unloaded and immediately reloaded in the reverse direction. The yield strength in compression is then found to be less than that of tension, and this directionality of yield stress or flow stress is known as Bauschinger effect [30]. The decrease in flow stress is attributed to the back stress which develops as a result of dislocation pileups in the forward loading direction that aid in the movement of dislocations when the loading direction is reversed. The difference between the forward and reverse loading curves can be quantified by means of the Bauschinger strain, which is defined as the amount of plastic strain in the reverse direction required to attain a desired stress level (which is usually the prestress level in the forward direction although, many researchers use the reverse plastic strain corresponding to 75% of the prestress value.) Mathematically $\beta = R\Delta\varepsilon_p$, where R is a function of the cyclic hardening exponent given by $R = (0.875)^{-n}$, and $\Delta\varepsilon_p$ is the plastic strain range. It has been found that β bears a linear relationship with plastic strain range for metals which exhibit masing behaviour.

2.8.2 Cyclic response:

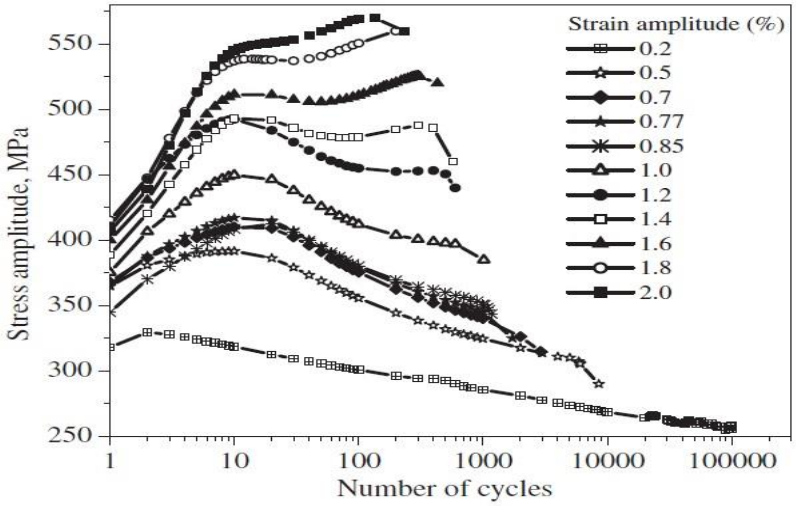

Fig 2.7 ***Cyclic stress response of SS 304LN at different strain amplitudes showing hardening and softening behaviour (Paul et. al)*** **[55]**

As plastic deformation is irreversible in nature, the cyclic stress or strain response depends upon the accompanying microstructural changes, the loading scheme, and the test temperature. A material may undergo cyclic softening or hardening or retain its cyclic stability depending upon how the material microstructure evolves with cyclic deformation. For strain controlled LCF tests a plot of maximum stress σ_{max} or the stress amplitude σ_a versus the number of cycles captures the material response against cyclic deformation (as illustrated in **Fig 6**). As the material hardens, the peak stress reached for a constant strain amplitude increases in magnitude with each passing cycle. Similarly, in case of cyclic softening, a decrease in the peak stress value is observed with the increasing number of cycles.

This material behaviour is also influenced by the prior loading history of the material, as well as the strain amplitude, as is evident from the works of Xie et al. [56] on cold drawn 316 Austenitic Stainless Steels. Experimental results point towards the existence of a threshold strain (0.35%) over which the material displayed a continuous softening behaviour, and below which the initial hardening was followed by a region of stability, after which cyclic softening occurred.
The amount of cyclic softening or hardening can be quantified by means of a factor known as the degree of hardening (H_e) which is mathematically expressed as

$$He = \frac{\Delta\sigma s - \Delta\sigma 1}{\Delta\sigma 1} \quad (2.7)$$

for strain-controlled tests, where $\Delta\sigma_1$and $\Delta\sigma_s$ are the stress amplitudes corresponding to the first cycle and saturation respectively.

$H_e>0$ for materials which cyclically harden, whereas for cyclically softening materials $H_e<0$. A strong dependence of the degree of hardening on strain amplitude has been observed in austenitic stainless steels of type 304L and 316 [57].

However, for stress-controlled conditions the corresponding stress amplitudes become strain amplitudes in the expression for H_e, and therefore while this parameter serves as a mathematical

tool for measuring the magnitude of hardening or softening, it is certainly inadequate when stress-controlled and strain-controlled test results are to be compared.

To overcome this difficulty a single hardening factor was introduced which could express the hardening or softening behaviour of materials without suffering from ambiguities due the method of test control. It is well known that during cyclic plastic deformation a stress-strain hysteresis loop is obtained whose shape continuously changes with cycle depending on the hardening or softening characteristics of the material. All hysteresis loops possess a definite geometry, with the loop width being equal to twice the plastic strain amplitude $\Delta\varepsilon_p$, and the loop height being double that of the stress amplitude $\Delta\sigma$.
As the stress amplitude is proportional to the elastic strain amplitude (following Hooke's law), the hysteresis loop geometry can be expressed by the ratio of the plastic and elastic strain amplitudes, and this ratio is known as the strain ratio (SR)

$$\text{S. R.} = \frac{\Delta\varepsilon_p}{\Delta\varepsilon_e} \tag{2.8}$$

From this definition it is evident that a decrease in strain ratio with the number of cycles reflects an increase in stress amplitude, indicating cyclic hardening whereas an increase in the strain ratio represents cyclic softening.
Using this definition of strain ratio, Paul et al [55] introduced the concept of the hardening

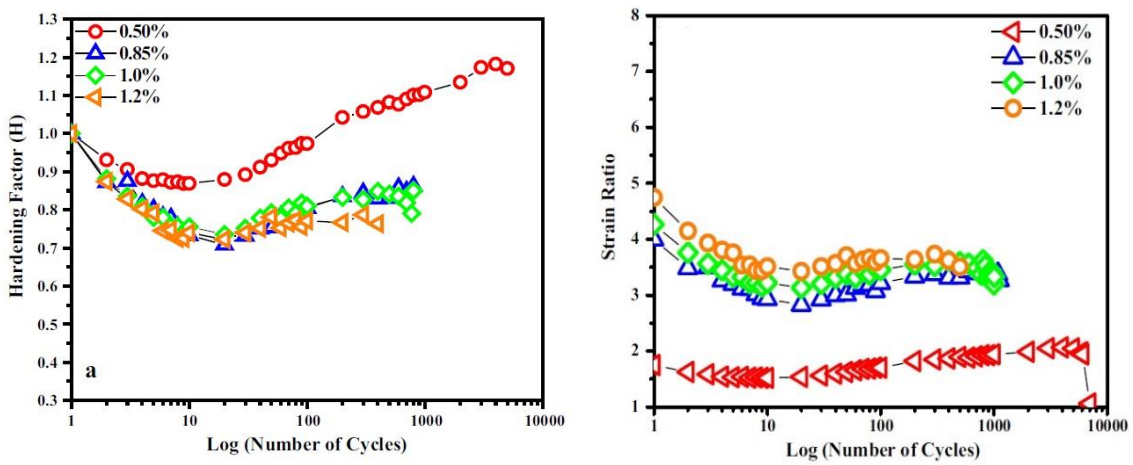

Fig 2.8 ***Variation of a) Hardening Factor b) Strain Ratio with the number of cycles at RT for SS 304LN*** **[58]**

factor (H) which could effectively be used for both strain-controlled and stress-controlled conditions. This factor is described as the ratio of the strain ratio at saturation to the strain ratio of the first cycle

$$H = \frac{S.R._S}{S.R._1} \tag{2.9}$$

H>1 is interpreted as cyclic softening, while H<1 indicates cyclic hardening.

2.8.3 Cyclic Stress-Strain Curve

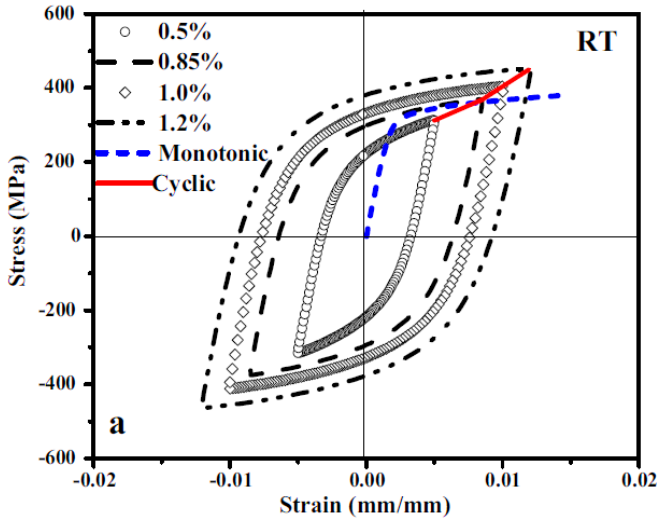

Fig 2.9 ***Monotonic tensile and cycle stress strain curves for SS 304LN at RT*** **[58]**

The cyclic stress-strain curve is obtained by connecting the tensile tips of stable hysteresis loops, or by equivalently plotting the peak stress against the strain amplitudes corresponding to the hysteresis loops at half-life cycle ($N_f/2$). It is usually assumed that the material response becomes stable after 100 cycles, but for cases where saturation is not obtained the maximum stress amplitude for hardening or the minimum stress amplitude for softening may be utilised. The cyclic stress strain curve can be described by the equation $\frac{\Delta\varepsilon}{2} = \frac{\Delta\sigma}{2E} + \left(\frac{\Delta\sigma}{2K'}\right)^{1/\acute{n}}$, where K′ is the cyclic strength coefficient, and n′ is the cyclic strain hardening exponent.
In general, cyclic hardening behaviour is to be expected when the cyclic stress strain curve lies above the monotonic tensile curve, and cyclic softening will occur when it lies below. Whereas, the material will demonstrate a stable behaviour if both of these curves are alike (when a constant difference between the curves is maintained). In general, an annealed metal or alloy would tend to display a cyclic hardening behaviour due to multiplication of dislocations. On the other hand if the material is quenched, prestressed or prestrained it will tend to soften due to the rearrangement of dislocation structures (similar to polygonalisation) in a manner that would decrease its resistance against further deformation.

According to Smith and his co-workers [59] a material exhibits cyclic hardening/softening behaviour depending upon the ratio of its tensile strength to its 0.2% offset yield strength. For $\frac{\sigma s}{\sigma y} \leq 1.2$, it cyclically softens, for $\frac{\sigma s}{\sigma y} \geq 1.4$ it cyclically hardens, and for intermediate ratios $1.2 < \frac{\sigma s}{\sigma y} < 1.4$ it displays both. It is important to mention that while the above criterion may be used as a general rule of thumb, the actual behaviour can only be observed by conducting the appropriate tests.

2.8.4 Strain life equations

The strain life equations can be used to predict the life or survivability of a component under fatigue. Depending upon the range or magnitude of stresses involved their forms vary. For low stresses that accompany elastic strains, the fatigue life is expressed as a function of stress

amplitude through the Basquin relation [60], and such conditions are simulated in High Cycle Fatigue (HCF) tests. For stresses of higher magnitudes which cause significant plastic deformation of the material, the Coffin-Manson (CM) relation [61][62] is used to predict the fatigue life. Primarily these stresses are of thermal origin and in turn originate from thermal strains. Such high magnitude stresses are encountered in strain controlled Low Cycle Fatigue (LCF) tests.

For the high cycle or low strain regime the Basquin relation describes the dependence of fatigue life on stress amplitude as

$$\frac{\Delta\sigma}{2} = \sigma_a = (\sigma_f)'(2N_f)^b \quad (2.10)$$

Where, σ_a is the stress amplitude, being the average of the maximum and minimum stresses of the cycle, $\sigma_f'$is the fatigue strength coefficient which approximately equals the true fracture stress in a tensile test, $2N_f$ is the number of reversals to failure and b is the fatigue strength exponent. For most metals b ranges from -0.05 to -0.12.
Thus, a plot of stress amplitude versus the number of reversals to failure is predicted to be linear on a double logarithmic scale.
For the low cycle, high stress regime a strain life based approach is followed and the following equation due to Coffin and Manson is used to predict the fatigue life under such conditions

$$\frac{\Delta\varepsilon p}{2} = \varepsilon\acute{f}(2Nf)^c \quad (2.11)$$

Here, $\frac{\Delta\varepsilon p}{2}$ is the plastic strain amplitude, ε_f' is the fatigue ductility coefficient and c is the fatigue ductility exponent whose value lies in between -0.5 and -0.7 for many metals

Though the distinction between the high cycle and the low cycle fatigue regimes is made upon the magnitude of stresses involved, a transition life N_t exists that separates the two. This can be obtained by equating the elastic and plastic strain amplitudes given by the Basquin and CM relations and the value of $2N_f$ satisfying both the equations simultaneously gives the transition life. From equations (2.10) & (2.11) $2N_t$ comes out to be $\left(\frac{\varepsilon f' E}{\sigma f'}\right)^{1/(b-c)}$.For $N_f < N_t$ the plastic strain amplitudes dominate and ductile materials perform well under such conditions, whereas for $N_f > N_t$ elastic strains overshadow the influence of plastic strains and strong materials having high rupture stress values are favourable under such conditions.

Sivaprasad et al [63] concluded by studying the cyclic behaviour of SS 304LN that the cyclic stress-strain curve (CSSC) was dependent upon the loading scheme and the response varied depending on whether the loading was carried out in decremental steps, incremental steps or through multi-specimen tests at different strain amplitudes.

2.8.5 Masing characteristics

Masing refers to the similarity of the loading or unloading branches of the stable hysteresis loops of a material at different strain amplitudes. The masing behaviour can be identified by translating the compressive tips of the loops to a common origin and observing whether the loading branches fall into a single curve. It is well known that masing behaviour is not displayed universally by engineering materials, and while some materials may exhibit masing

behaviour others may not. Masing behaviour is also dependent on the loading path and the prior loading history of the material. 304LN stainless steels are known to exhibit non-masing behaviour for various loading schemes at room temperature, but according to Padmanabhan [64] the same steels after being 30% cold-rolled displayed masing behaviour. It has been found that masing behaviour is intimately related to the phase stability and the formation of a stable dislocation cell structure. With this line of reasoning the non-masing behaviour of 304LN can be justified based on EBSD and TEM results which provide conclusive evidence that the microstructure of such steels are not stable and deformation induces martensitic transformation. Furthermore, the dislocation cell aspect ratios (L/W) are also found to change consistently with the variation of strain amplitude. It has also been emphasized that the distribution of second phase particles and their mode of interaction with dislocations play a crucial role in controlling the Masing characteristics. Masing behaviour is favoured in presence of hard unshearable particles that are in close proximity to one another, while this behaviour becomes non-masing as the interparticle spacing increases.

In order to find out the magnitude of deviation from masing behaviour, the stable hysteresis loops at different strain amplitudes are translated along their elastic portions (with the loop having the minimum proportional range being fixed as reference) until their ascending branches overlap into a single curve.
The expansion of the linear portion which corresponds to an increase in proportional limit gives the value of the non-masing stress ($\delta\alpha_0$).
An equation for this new curve with respect to the origin of the translated axes is as follows

$\frac{\Delta\varepsilon^*}{2} = \frac{\Delta\sigma^*}{2E} + \left(\frac{\Delta\sigma}{2K^*}\right)^{\frac{1}{n}^*}$, where the asterisk signifies that the quantity is measured w.r.t the translated coordinate axes.

Another interesting observation was made by Yadav et al [65], as he along with his co-workers found that the master curve could not be Fig

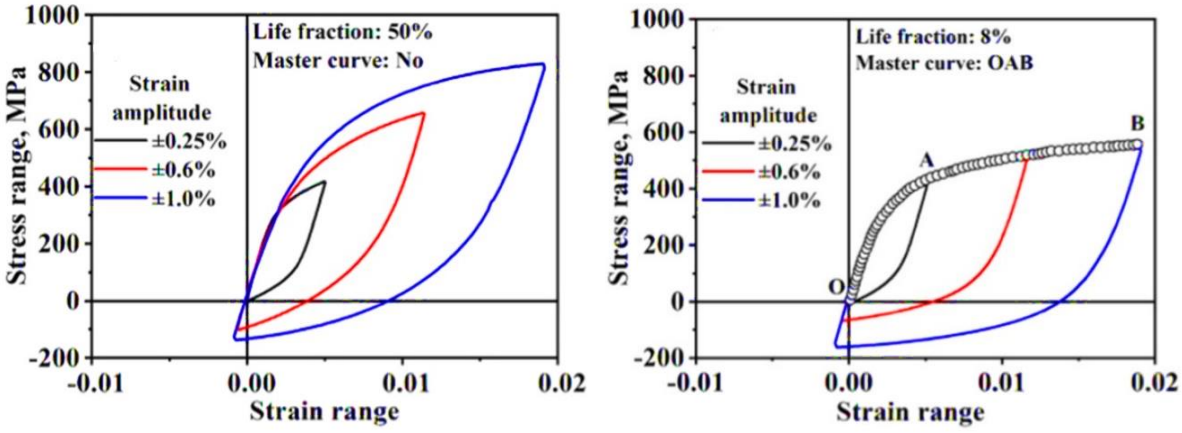

2.10 a) Type-I non-masing behaviour and master curve construction, b) Type-II non-masing behaviour [65]

constructed for certain materials like SS 304L, AISI 321 and BLY160. Based on the impossibility of a master curve construction, they classified
these materials as displaying a Type-II non-masing behaviour alongside the Type-I non-masing materials whose master curve construction was possible.

Although as has been pointed out previously a material can switch between masing and non-

masing behaviours when the test conditions or the loading path is altered, these materials can switch between Type-I and Type-II masing behaviour based on the fraction of the total fatigue

life at which the hysteresis loops are constructed.

As an evidence supporting this fact, Yadav et al [64] found that SS 304L seemed to switch to Type-II non-masing behaviour above 10% of its fatigue life from its initial Type-I behaviour.

2.8.6 Cyclic Plastic Strain Energy

During LCF tests, most of the plastic strain energy is dissipated as heat while the remaining portion is absorbed. Morrow and Felter [66] were the first to suggest that energy has a great impact on the fatigue life of a component. Both the average strain energy absorbed by the material per unit volume per cycle (plastic strain energy density), and the cumulative (total) plastic strain energy absorbed by the specimen over its entire fatigue life are the decisive factors controlling the life of a component. Mathematically the plastic strain energy absorbed can be determined from the area of the stable hysteresis loop given by $\Delta Wp = \int \sigma \, d\varepsilon$.

Assuming that the material displays a masing behaviour, the cyclic plastic strain energy absorbed by the specimen per cycle can be expressed by the Manson-Halford equation

$$\Delta W_{\mathrm{p}} = \frac{(1-n')}{(1+n')} \Delta\sigma \Delta\varepsilon_{\mathrm{p}} \tag{2.12}$$

where n' is the cyclic strain hardening exponent, $\Delta\varepsilon_{\mathrm{p}}$ is the plastic strain range and $\Delta\sigma$ is the stress range

A similar relation was derived by Quesnel [67] based on the assumptions that the cyclic stress strain curve of the material can be expressed by a power law and that the CM equation is obeyed:

$$\Delta W_{\mathrm{p}} = \frac{4K'}{(1+n')} \Delta\sigma \Delta\varepsilon_{\mathrm{p}} \tag{2.13}$$

where the symbols bear their usual meanings.

LCF studies on A-516 Gr70 carbon steels by Lefebvre and Ellyin [68] revealed that the ΔW_{p} of materials which displayed a non-masing behaviour could not be predicted accurately by using the Halford equation, due to its non-masing characteristics. This led to a further modification of the relation to account for the increase in proportional limit with increasing strain amplitude. The modified equation being given as follows:

$$\Delta W_{\mathrm{p}} = \frac{(1-n')}{(1+n')} \Delta\sigma \Delta\varepsilon_{\mathrm{p}} + \frac{2n\prime}{(1+n')} \Delta\varepsilon_{\mathrm{p}} \delta\alpha_{\mathrm{o}} \tag{2.14}$$

Xiaoyan [69] reported that the cyclic plastic strain energy does not show appreciable variation with the number of cycles for fully reversed strain-controlled tests.
It has been suggested that ΔW_{p} remains constant for the majority of the fatigue life, forming the crack initiation phase in which micro-cracks start to nucleate. As the number of cycles increase the plastic strain energy absorbed by the material starts to accumulate and a critical value is reached beyond which the cracks start propagating. This phase is identified by a

precipitous drop in the ΔW_p value leading to the diminishment of the load bearing capacity of the material, followed by subsequent failure.
Another important parameter is the total energy absorbed by the specimen throughout its fatigue life that serves as a measure of its fatigue resistance and is appropriately termed as the fatigue toughness (W_f). The W_f value can be obtained by multiplying the number of cycles to failure with the average plastic strain energy obtained from the hysteresis loop at half-life.

$$\Delta W_f = N_f \, \Delta \overline{W}_p \tag{2.15}$$

Studies show that $\Delta \overline{W}_p$ is related to the number of reversals to failure by a Coffin-Manson type relationship that is expressed as

$$\Delta \overline{W}_p = W_f'(2Nf)^{\omega} \tag{2.16}$$

Where W_f' represents the fatigue toughness coefficient, and ω stands for the plastic strain energy exponent which is related to the exponents b and c as $\omega = b + c$

A general trend which has been reported by several authors including Li et al.[70] is that the average plastic strain energy $\Delta \overline{W}_p$ decreases in a linear fashion with the number of cycles to failure when plotted on a double logarithmic scale, indicating that the loop area increased with increasing strain amplitude.

2.9 Fatigue fracture Morphology of Austenitic Stainless Steels

Typically, a sequence of three distinct stages have been identified that lead to fatigue fracture. During stage-I, crack initiation occurs at persistent slip bands (PSBs) and deepening of initial cracks occur on planes having high shear stresses. During stage-II, crack growth occurs normal to the direction of the maximum tensile stress. Propagation of stage-II cracks occupy a sizeable portion of the fatigue life of a component in low cycle fatigue. During stage-III the cracks grow to a critical length beyond which the material cross-section becomes incapable of withstanding any further load, ultimately leading to fracture.

The initiation of fatigue cracks is often represented by the Wood's model [30], according to which slip takes place on favourably oriented planes during the increasing part of the loading cycle, whereas during the reverse part of the cycle slip occurs in the opposite direction but on different planes which are parallel to the initial slip planes. Movement along the initial slip planes is hindered either due to strain hardening or because oxidation of the newly formed surface. In this manner, each cycle creates intrusions or extrusions on the material surface. With increasing number of cycles, the depth of intrusions along with height of extrusions increase, with the intrusions giving rise to fatigue cracks.

A characteristic feature of a fatigue fracture surface is the presence of striations. Fatigue striations are caused by the repeated blunting and re-sharpening of the crack tip during the tension and compression cycles, with new a striation mark being added during each cycle.
It is known that the striation spacing increases with increasing strain amplitude [71].

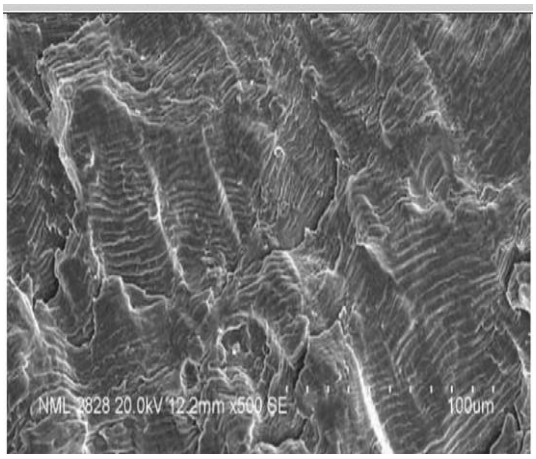

Fig 2.11 ***Fatigue fracture surface showing striation marks in SS 304LN cycled at SA*** $\pm 0.7\%$ **[71]**

2.10 Types of Corrosion & Corrosion behavior of stainless steels

Corrosion is a general term which refers to the environmental degradation of a metal through electrochemical interactions with its surrounding environment. The pervasive effect of corrosion cannot be eliminated in its entirety but it can be mitigated through various means. The detrimental effects of corrosion including the loss of efficiency of a component, economic loss, contamination etc. if not checked can lead to catastrophic end results, often resulting in the loss of human lives. The bridge collapse at Pt. Pleasant in West Virginia 1967 serves as a testament and a grim reminder that corrosion if left unchecked can claim the lives of many [72].

Corrosion is inherently electrochemical in nature, requiring electronic charge transfer between the corroding metal surface and its environment.

The various forms of corrosion have been briefly summarized as follows:

i) Uniform corrosion: Uniform corrosion is characterized by the uniform removal of metal from its surface. This is one of the most commonly encountered form of corrosion but it requires the metal to be uniform in its composition, furthermore the environment should have access to all parts of the corroding metal surface. In practical scenarios this is rarely the case and some degree of non-uniformity is always present.

ii) Galvanic corrosion: Galvanic corrosion occurs when two dissimilar metals are in mutual contact in presence of an electrolyte. A metal that occupies a position higher in the series(the one with a more positive electrode potential) gets protected while a metal having a lower reduction potential gets preferentially corroded. This principle is used in underground pipelines using stainless steels in order to protect them from damage due to corrosion.

iii) Crevice corrosion: Crevice corrosion is a form of localized corrosion usually occurring between two dissimilar metals and is focused on a small area of contact formed by the metal-metal interface. This situation is frequently encountered in riveted joints where the contact region between the bolt metal surrounding the base metal plate gets corroded. Stainless steels are known to undergo crevice corrosion in aerated salt solutions.

iv) Pitting corrosion: This is yet another localized form of corrosion characterized by the formation of pits. In stainless steels this type of corrosion is quite prevalent, as the corrosion resistance of these steels depend on the stable passivating layer of oxides (usually of Chromium, Aluminum) that is deposited over the metal surface. These oxide films are especially susceptible to chloride environments and any form of localized environmental attack leads to a local breakdown of this layer accompanied by the subsequent formation of pits.

v) Intergranular corrosion: This type of corrosion as mentioned earlier occurs due to chemical segregation or depletion of elements such as chromium from the grain boundaries. The result is a deficiency of passivating elements like chromium at the grain boundaries and their surrounding regions, making them vulnerable to corrosive attack from the environment. This problem is central to steels containing less than 10 wt. % chromium and is aggravated due to chromium carbide precipitation in the temperature range of 425℃ to 815 ℃.

vi) Environmental Induced Cracking: Apart from the different forms of corrosion that are commonly encountered, the damage incurred due to the effect of corrosion gets amplified when a material is stressed in a corrosive environment. Three distinct forms of failure which occur due to the combined effect of stress and environmental interaction are described as follows:

vii) Stress Corrosion Cracking: Stress corrosion cracking occurs in metals which are subjected to static tensile stresses in particular environmental conditions. The effect of SCC is profound in alloys whereas pure metals remain relatively unaffected by it [72]. Specific environmental conditions are required to initiate stress corrosion cracking such as hot chloride solutions for stainless steels, presence of nitrates for carbon steels. It has been demonstrated that dissolved oxygen levels along with halide ion concentration plays a crucial role in SCC. The problem is further aggravated at elevated temperatures, but the existence of a temperature threshold below which the susceptibility to SCC is reduced is yet to be ascertained. However practical results suggest that pitting and crevice corrosion dominate at lower temperatures especially if chloride ion concentrations are low. SCC culminates into brittle fracture in metals.

viii) Hydrogen Induced Cracking: Hydrogen induced cracking occurs due to the diffusion of atomic hydrogen into the alloy lattice in absence of an applied stress field. Existing cracks start propagating as the internal pressure begins to mount after the solubility limit of hydrogen is exceeded locally and molecular hydrogen starts to precipitate at potential sites of crack initiation such as foreign inclusions, inhomogeneities or defects. This phenomenon is more pronounced in environments containing H_2S which serves two crucial purposes, the first of which is to act as a source of hydrogen and the second one is to prevent atomic hydrogen from recombining into their stable diatomic form, which can then diffuse easily into the alloy lattice. HIC is however remains a greater concern for non-austenitic steels.

Another closely related phenomenon is that of hydrogen embrittlement, which commonly refers to the loss in ductility manifested by metals due to the entrapment of atomic hydrogen into the metal lattice. Though HIC and Hydrogen Embrittlement may be similar in certain terms there are subtle differences which distinguish them both. The first one is that the effect of the latter can only be detected in presence of an applied stress and the second one is the fact that hydrogen embrittlement is reversible nature, which implies that if the entrapped hydrogen is purged or driven out of the metal lattice it's ductility gets restored [73].

Experiments conducted on 304L tensile specimens have shown that specimens which were cathodically charged in 1 N H_2SO_4 suffered a steady decline in % elongation or ductility as the charge time was progressively increased. Also, those which were charged for 24 hours regained

their original elongation values when they were retested after being subjected to chemical milling at room temperature. This further attests that hydrogen embrittlement is reversible in nature, and is limited by the diffusion of hydrogen into a thin surface layer which upon being removed restores the ductility of the metal[74].

ix) Corrosion Fatigue Cracking: Corrosion Fatigue Cracking occurs in presence of cyclic or fluctuating stresses in a corrosive environment. The fatigue life of a component gets reduced due to the combined effect of alternating stress and environmental degradation. One of the prerequisites of CFC is that a tensile component of the alternating stresses must be present. The CFC cracks are known to initiate from corrosion pits and the corrosion products usually accumulate within the cracks. High frequency rotating bending fatigue tests conducted in NaCl solution of varying concentrations on 12% stainless steels have unveiled that the fatigue life decreases when the concentration of NaCl is increased. In the high cycle regime about 75% reduction in fatigue strength have been reported in 3 wt.% NaCl aqueous solutions in comparison with the test results in air. [75]
Stainless steels show an active-passive corrosion behavior, owing to the stable film of chromium and iron oxide that forms in oxidizing conditions. In the active region, corrosion

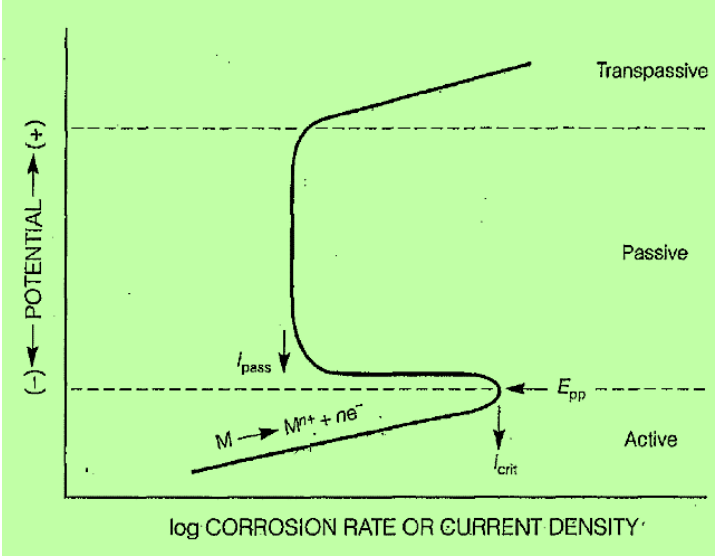

Fig 2.12 ***Anodic polarization curve of a material displaying active-passive behavior*** **[72]**

rate determined from the anodic current density increases with increase in potential. As the steel is further polarized, a point is reached beyond which the current density starts to decrease, this is commonly referred to as the primary passive potential Epp. Increasing potential values above Epp results in a stark decline in current density often by several orders of magnitude, and a stable passive oxide layer forms. From this point onwards the current density remains constant with increasing values of potential and the steel enters the passive region. At higher values of polarization this passive film suffers a local breakdown and pits are formed. The potential at
which the initiation of pitting occurs is termed as the pitting potential E_{pit},for once this potential is reached the current density starts to increase once again and the material enters the transpassive region.

2.11 Mechanism of pitting corrosion

The pitting corrosion resistance of an alloy depends on several parameters including the pH and temperature, with high values of pitting potentials suggesting nobility or inertness to pitting corrosion. The presence of Cl^- lowers the pitting potential of an alloy, and the pitting reaction is proposed to proceed in the following manner based on corrosion studies on iron. In absence of Cl- ions the breakdown of the passive layer is a slow and prolonged process in which the hydrated oxide layer gradually breaks down ,yielding ferric ions .The presence of halide ions such as chloride Cl^- catalyzes the breakdown of the passive layer by reacting with and substituting the hydrated passive film ($FeOOH$) and forming an intermediate $FeOCl$ complex which easily breaks down to give ferric ions. This causes the preferential thinning of oxide film at an heterogeneity or an inclusion site, gradually removing it layer by layer until the bare metal gets exposed. The metal in contact with the surrounding media then anodically dissolves to give Fe^{2+} ions and a local pit is generated. [72]

Pits are found to nucleate at preferential sites containing inhomogeneities or inclusions (most often sulphide inclusions). The grain boundaries of a sensitized stainless steel often serve as initiation sites for pits to develop and grow.

2.12 Role of alloying elements in corrosion of steels:

Chromium: Chromium increases the resistance to corrosion in stainless steels over a broad range of potentials and pH. Therefore, duplex stainless steel grades are considerably more resistant to corrosion owing to the greater percentage of chromium (in excess of 20%) present in them.

Nitrogen: Nitrogen enhances resistance against localised corrosion such as pitting and crevice corrosion. A mechanism put forward by Osozawa and Okato [76] suggests that ammonium ions are created locally around pits which acts as a buffer to restrict and regulate the pH values within tolerable limits. Addition of Nitrogen has been found to increase the region of passivity in steels, thereby delaying the onset of pitting. Stainless steel grades containing Nitrogen such as 316LN have higher pitting potentials at all temperatures when compared with the 316 or 316L variants which do not contain Nitrogen.

Molybdenum: The presence of Mo retards the growth of pits. This fact has been experimentally validated by Tomashov [77] on 18Cr-14Ni steels, which show that both the diameter and depth of pits increased at much slower rates in steels containing Mo in comparison with those which did not contain Mo.

Other elements: Addition of elements like V, Si, Re have shown to increase the corrosion resistance of steels by stabilizing the passive oxide layer. Elements like Boron and Carbon can have different effects depending on whether they are present in solid solutions in their elemental state or as compounds in the form of borides or carbides. When present in solid solutions boron has beneficial effects on corrosion resistance while carbon has little to no perceptible effect. Carbides on the other hand are known to have harmful or deleterious effects and deteriorates the corrosion resistance in steels. Rare earth metals, Te and Se are conducive to the formation of harmful telluride and selenide precipitates. Whereas Re additions help in strengthening pitting corrosion resistance.

The effect of main alloying elements like Cr, Mo and N on the corrosion resistance of stainless steels can be cumulatively expressed by a number known as the Pitting Resistance Equivalent Number (PREN)[78],the mathematical expression for which is $\%Cr + 3.3\%\, Mo + (16\%\ or\ 30\%)\ N$. The coefficient of Nitrogen is either taken as 30 if the steel is an austenitic stainless steel or 16 if the steel has a duplex microstructure.

Titanium: Addition of Ti in small quantities helps in achieving pitting potential values which are nobler than those observed in Ti free alloys and steels, thereby increasing their resistance against pitting [79]. A possible explanation for the above lies in the fact that Ti owing to its good affinity for carbon and nitrogen binds with them prevents them from forming harmful chromium carbides and nitrides which causes depletion of chromium from the base matrix making it vulnerable to corrosion attack.

Copper: The influence of copper on the pitting corrosion behaviour of stainless steels is controversial, with several experiments on SS 301 steels reporting beneficial effects when minute additions of copper were made, such as in increase in wt. percentage from 0.2% to 0.5% [80]. Larger additions of copper (>1%) produced no discernible effect. Later studies have hinted that addition of Cu in excess of 1.5% was undesirable, whereas concentrations below 0.8% showed an intermediate behaviour characterised by the initiation and repassivation of small pits or the creation of metastable pits.

Silicon: The addition of Si has a positive impact on the pitting corrosion resistance of stainless steels. Experimental works of Wilde [81] on 18Cr-8Ni stainless steels have explicitly demonstrated that Si increases the Critical Breakdown Potential (E_c) which marks as the potential beyond which the material enters a transpassive zone, distinguished by increasing anodic current densities after passivity breaks down and pitting ensues. Increased Ec values imply that the passive region in which the current density almost remains constant gets extended, signifying an improved corrosion resistance of the material.

2.13 Corrosion test parameters and their measurements

Corrosion of a conducting surface such as a metal dissolving in an acid solution implies that both the oxidation of metal and reduction of H^+ ions to H_2 occurs on the same surface. The oxidation and reduction reactions represent two half-cell reactions. However different electrode potentials corresponding to the two reactions cannot exist simultaneously on a conducting surface. Upon consideration that there is no accumulation of charges, both the reactions must proceed at a common potential known as the corrosion potential (E_{corr}) and the associated current is referred to as the corrosion current (I_{corr}).

Both the E_{corr} and I_{corr} values can be determined from linear polarization tests (which may be galvanostatic, potentiostatic or potentiodynamic depending on whether the current or potential is controlled during the tests). Both potentiodynamic or potentiostatic tests can be conducted in a potentiostat attached to three electrodes dipped in an electrolytic chamber. An external overvoltage is applied, between a standard electrode and the metal to be tested (acting as the anode), and the current passing through the counter electrode (cathode) and the metal is recorded as a response. The coordinates of the intersection point of the linear cathodic and anodic branches (known as Tafel's plots) of the polarization curve thus obtained gives the required parameters.

The corrosion current density i_{corr} is related to the rate of corrosion (or metal loss) as

$$r = \frac{0.129\ a\ j_{corr}}{n\rho} \tag{2.17}$$

where r is the corrosion rate in mils per year (1 mil=0.001 inch), ρ is the density of the material in g/cm^3, i_{corr} is the corrosion current density in μA/cm^2 and a is the atomic weight in g.
Implying that materials possessing low j_{corr} values along with high E_{corr}values have higher corrosion resistance.

Resistance against pitting corrosion on the other hand is evaluated on the basis of pitting potential (E_{pit}), which is the potential above which the anodic current density dramatically increases due to pit formation and propagation. As a consequence, the higher the E_{pit} value the more resilient is the material against pitting corrosion attack. As mentioned before, pitting corrosion becomes a concerning factor in chloride containing environments.

An interesting phenomenon observed in materials like SS 304 which are susceptible to pitting corrosion is that in cyclic polarization tests when such a material is polarized into the transpassive region following which the direction of polarisation is reversed, the material follows a more active path which is different than the initial polarization curve (hysteresis). The point at which the reverse polarization curve intersects the initial curve marks the protection potential E_{prot}, below which existing pits cannot grow, and pitting corrosion is arrested [72]. Between these two values existing pits can continue to grow but pitting initiation ceases.

The effect of intergranular corrosion (IGC) in stainless steels can be quantified by double-loop electrochemical potentiokinetic reactivation tests (DL-EPR) tests. Prior to conducting the tests the test samples are first solutionised at temperatures in excess of 1100℃. After which sensitization heat treatments are performed at 550℃- 850℃ for various exposure times.
The tests are now conducted by polarizing the sensitized specimens upto a potential within the passive region, from which reverse polarisation was carried out to all the way to the cathodic region. The degree of sensitization (DOS) is then obtained as the ratio of peak reactivation current (I_r) to the peak activation current (I_a) expressed as a percentage. A low DOS value signifies more resistance to IGC.[82]

2.14 Weldability of stainless steels:

i) *Austenitic stainless steels*

Austenitic stainless steels are known to possess good weldability, but factors such as impurity levels of Sulphur and Phosphorus, composition of base and filler material play a pivotal role during the solidification of weldments. Problems such as weld solidification cracking have been known to occur in Austenitic Stainless Steels. While high levels of S and P increases the likelihood of solidification cracking, the composition of the base metal or more specifically the Cr_{eq} /Ni_{eq} value exercises control over this phenomenon [3]. It has been shown that when the primary solidifying phase is austenite the susceptibility to solidification cracking is the greatest whereas when ferrite is the primary solidifying phase, solidification cracking is largely suppressed.

ii) ***Ferritic stainless steels***

Ferritic stainless steels are generally less prone to solidification cracking, but presence of alloying elements such as Ti and Nb is known to promote solidification cracking in such steels. One of the more concerning problems encountered during the welding of these steels is that they undergo High Temperature Embrittlement (HTE) in the Heat Affected Zone (HAZ). High levels of interstitial elements such as C and N coupled with coarse grain sizes increase chances of HTE. [3]
HTE results in a loss of tensile ductility and toughness due to the intragranular precipitation of chromium carbides, nitrides or carbonitrides during cooling of the weldments.

iii) ***Martensitic stainless steels***

Martensitic stainless steels are prone to Hydrogen Induced Cracking (HIC) due to the presence of untempered martensite. Thus, welding of martensitic stainless steels is usually accompanied by pre or post weld heat treatments. Another problem that is encountered frequently is that of reheat cracking which occurs due to cyclic heating triggered by multiple weld passes or post weld heat treatments. Presence of Mo along with impurities such as S, Pb, Sb, Sn, B and Cu have been associated with this type of cracking.

iv) ***Duplex stainless steels***

Duplex stainless steels are resistant to both HIC and solidification cracking, but the presence of high amounts of Cr and Mo results in the precipitation of intermetallic compounds (sigma and chi phases) in the temperature range of 570 ℃ - 1000℃ causing substantial loss in ductility and toughness of the weld metal. Some portions of the weld metal including the HAZ are inevitably exposed to this temperature range during the welding, cooling and reheating cycles. To combat this problem a step annealing post weld heat treatment (PWHT) procedure has been adopted [83].

2.15 Summary of literature review:

1. Work hardening behaviour of stainless steels can be described by several semi-analytical equations which have their own applicability and limitations.

2. Cyclic hardening/softening behaviour of a material is an indication of the microstructure/sub-structure changes of the material due to cyclic deformation. Depending on the initial state, a metal may undergo cyclic hardening, cyclic softening, or remain cyclically stable. Cyclic hardening/softening behaviour of the material can be analyzed by strain ratio (SR) and Hardening factor (H, He).

3. Martensitic transformation occurs in austenitic stainless steels due to the metastable nature of the austenite phase. This transformation significantly affects the cyclic strain response and the work hardening behaviour of the material.

4. Depending on the Stacking Fault Energy (SFE) of the steel strain, induced α'martensite transformation can occur directly or via an intermediate ε -martensite phase.

5. Both the test temperature and the strain rate have a great impact on the amount of martensitic transformation that occurs for a steel of a given composition. The poor thermal conductivity of austenitic stainless steels is responsible for causing adiabatic heating at high strain rates, which lowers the amount of martensite being formed.

6. Alloying elements influence the phase stability, and have their own unique ways of controlling the corrosion properties in stainless steels, the effectiveness of which depends on the amount and the synergy between the different alloying elements present.

7. The masing behaviour is not an universal phenomenon in engineering materials as it depends on the prior loading history in addition to the path of loading.

8. The nature of the tensile flow curve in austenitic stainless steels change as the testing temperature is varied from cryogenic values to room temperatures.

9. DSA phenomenon or the appearance of serrations in the tensile flow curve is observed at elevated temperatures.

OBJECTIVE OF THE PRESENT WORK

The objective of the present investigation is to study the Tensile deformation behavior and the Low Cycle Fatigue behavior of Austenitic Stainless Steel 304L at room temperature. The analysis encompasses the variation of tensile test parameters with strain rate, hardening or softening characteristics of the material with cyclic deformation, comparisons between the monotonic tensile curve and the cyclic stress strain curve, it's masing characteristics, energy analysis and calculation of fatigue resistance, and quantitative analysis of deformation induced martensite using various characterization techniques. Furthermore, the corrosion behavior of the material has been studied and attempts have been made to correlate the effect of strain or deformation on the corrosion rate, the region of passivity and the pitting potential E_{pit} value of the steel.

Chapter 3

Experimental Details

3.1 Chemical Composition

The chemical composition of the austenitic stainless steel AISI 304L used for this study is given below:

Element	C	Mn	Si	S	P	Ni	Cr	Mo	Ti	Cu	N
wt. %	0.025	1.49	0.385	0.017	0.029	8.18	18.26	0.073	0.0046	0.51	0.037

3.2 Heat Treatment

Industrially procured cylindrical samples having 120 mm length and 16 mm diameter were subjected to solution annealing heat treatment in a tube furnace. The samples were heated inside the furnace from room temperature to 1100^{o}C at a slow heating rate and were held at that temperature for 45 min with a 10 min stabilization time. The temperature displayed by the furnace was monitored by a K type (Chromel-Alumel) thermocouple to which cold junction correction was applied to account for the effect of ambient temperature. After the soaking period was over the samples were removed from the furnace and quenched in water at an ambient temperature of 28 ^{o}C. This was accompanied by steady stirring to prevent oxide scale formation during the initial period.

3.3 Optical Microstructure

1.5 inch thick samples were sectioned off from the solution annealed blanks using the Struers Secotom-20 abrasive cutter for the purpose of studying the optical microstructure. The samples were subjected to metallographic polishing using the Struers Labopol-5 polisher equipped with coarse and fine grades of emery paper. After paper polishing, the specimen were cloth polished and Al_2O_3 paste (grit size 0.25 μm) was applied during polishing to obtain a scratch free mirror-like finish.
Subsequently, the polished surface was etched using glyceregia (HCl 40 vol%, HNO_3 20%, glycerol 40 vol%) and then viewed under an optical microscope (LEICA DM2700 M). Micrographs were obtained by using a digital camera interfaced with a personal computer.

3.4 Hardness Measurement

The Vickers Hardness value of the sample in solution annealed condition was obtained as an average of 20 readings. The tests were carried out in the micro-forces range under a load of 300gf and a dwell time of 10s using the Matsuzawa Vickers microhardness tester (AMT-X7BFS). The machine was coupled with a personal computer and was operated using the AMT-WIN software.

3.5 Uniaxial tensile tests

Uniaxial tensile tests were carried out on cylindrical tensile specimens machined from the solution annealed blanks. The dimensions of the specimen conformed to the ASTM E8 standard. The specimen geometry being given follows:

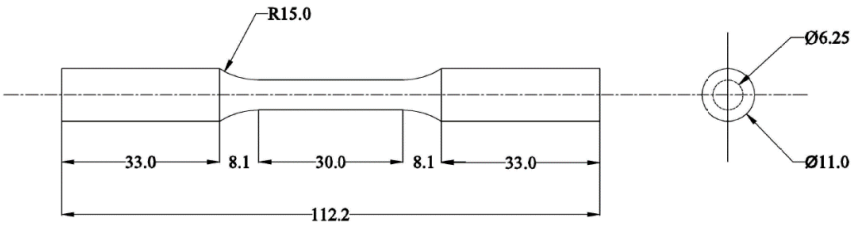

Tensile specimen geometry, all dimensions are in mm

Strain controlled tensile tests were carried out till fracture on a servo-electric Universal Testing Machine (Instron 8862) having ± 100 kN load capacity, under the strain rates of $10^{-3}s^{-1}$ and 10^{-4} s^{-1}.A 25 mm gauge length extensometer was used to measure the strain imposed on the specimen during the test. The machine was linked to a computer console through a controller which could read and record data. Test parameters were controlled with the help of Bluehill software, and about 4000 data points were recorded in each test.

3.6 Interrupted tensile tests

A total of four interrupted tensile tests were carried out at a strain rate of 10^{-3} s^{-1}, which involved straining the samples to engineering strains of 16.18%, 28.4%, 41.9% and 56.8% respectively, following which they were unloaded. The tests were carried out under strain control until the desired strain value was reached, this was followed by a load-controlled step in which the load was gradually brought down zero. The step change was made with the help of Instron Wavematrix software.

3.7 Low cycle fatigue tests

Completely reversed strain-controlled low cycle fatigue tests were performed under a strain rate of $3 \times 10^{-4}s^{-1}$. Test specimens having 14mm gauge length and 8 mm gauge diameter were prepared in accordance with the ASTM E606 standard.
Fig … illustrates the specimen geometry

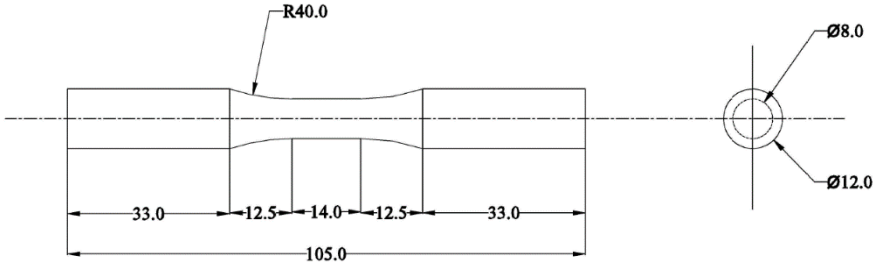

Low cycle fatigue test specimen, all dimensions are in mm

Multi-specimen LCF tests were conducted till failure for a total of seven different strain amplitudes ranging from $\pm 0.35\%$ to $\pm 1.2\%$. The tests were carried out with the help of Instron LCF 3 software, with the data being digitally recorded in a personal computer. Approximately 300 data points were sampled per cycle. A symmetric triangular waveform with a constant strain rate of $3 \times 10^{-4}s^{-1}$ was used as the input for cyclic straining. The frequency f at which the specimen were cycled was adjusted to match the strain rate $\dot{\varepsilon}$ and strain amplitude ε_a, according to the relation
$f = \dot{\varepsilon} \,/\, (4\varepsilon_a)$.
A 12.5 mm gauge length static extensometer ($\pm 20\%$ travel)was used to measure the strain, and all the tests were repeated for better reproducibility.

3.8 Ferritoscope Measurements

After conducting uniaxial tensile and LCF tests at room temperature, ferritoscope measurements were taken throughout the gauge length of the specimen in order to determine the fraction of α'-martensite phase (ferromagnetic) being formed at various strain levels. The ferritoscope was calibrated against standard samples of δ-ferrite prior to measuring, and an average of 300 readings were taken in each case to obtain a reasonable estimate of the Ferrite Number (FN). The FN values were then converted into the corresponding weight percentages by multiplying a factor (talonen's correlation factor) of 1.7.

3.9 Corrosion tests

Electrochemical measurements were conducted on 8 mm long samples that were sectioned off from the gauge length of the specimen after carrying out LCF and interrupted tensile tests at room temperature. The samples after being cut, were subjected to the usual metallographic polishing before they were tested. Potentiodynamic linear polarization tests were carried out in a potentiostat by using three electrodes, with the specimen acting as the anode, a graphite rod working as the counter electrode and a saturated calomel electrode (SCE) acting as the reference with respect to which the potential values were measured. The specimen were carefully suspended in a 3.5 wt% NaCl solution which was used as an electrolyte. Only the area at cross-section remained exposed whereas the rest of the specimen was carefully wrapped in teflon in order to prevent any current contribution from the adjacent areas. The tests were performed at a scan rate of 0.0005 Vs^{-1} over scan range of -0.7V to 1V, starting from the OCP (Open Circuit Potential) values that were measured after 10 min. External overvoltage was impressed upon the circuit from which the corresponding current (i_{app})was recorded as the difference between anodic and cathodic currents. The characteristic active-passive polarization curves were obtained and the E_{corr} and I_{corr} values were established by using the coordinates of the intersection point of the linear cathodic and anodic branches of the curve.

3.10 SEM (Scanning Electron Microscopy)

Fractographs of the fractured tensile and LCF specimens were obtained on a HITACHI SU 3800 Scanning Electron Microscope under secondary electron imaging mode. Before imaging, 4mm long samples containing the fracture surface were extracted from the gauge length of the specimen, after which they were ultrasonically cleaned for 10 min in an acetone bath. A Rivotek Ultrasonic Cleaner was used for the cleaning procedure. The operating voltage of the tungsten source was kept at 20kV.

4. Result and Discussion

4.1 Optical Microscopy:

The optical microstructure of AISI 304L stainless steel in the solution annealed condition was found to contain polygonal austenitic grains. Some grains were found to be interspersed with annealing twins, which is a characteristic feature encountered in the micrographs of many fcc metals or alloys, and austenitic stainless steels in particular. Annealing twins serve as a clear indication that the metal/ alloy was subjected to cold work or deformation prior to the annealing heat treatment. Due to the different crystallographic orientation of the twins with respect to the surrounding grains, they appear as distinct broad bands after being etched.

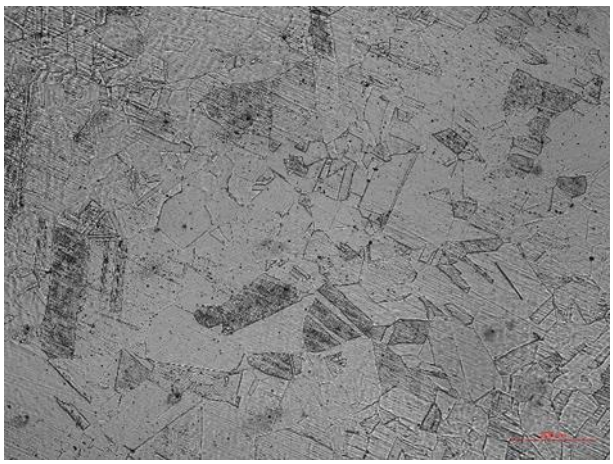

Fig 4.1 Base microstructure of 304L austenitic stainless steel after being solution annealed at 1100^0 C for 45 min.

4.2 Monotonic Tensile deformation behavior of SS 304L at RT:

Monotonic tensile tests were carried out at the strain rates of $10^{-3}s^{-1}$ and $10^{-4}s^{-1}$ respectively.

The results are tabulated as follows:

Table 4.1: Room temperature tensile properties of solution annealed 304L steel at different strain rates

Strain Rate (s^{-1})	0.2% offset Y.S.(MPa)	UTS (MPa)	Total Elongation (%)	Uniform Elongation%	Reduction in Area (%)	True fracture ductility (%)
0.0001	224	703	84	71	80	163
0.001	227	669	79	67	79	156

Upon comparing the test results for the two different strain rates it is evident that increasing the strain rate results in a marginal increase in Y.S. of the material which is accompanied by a decrease in its UTS value along with its total elongation. This is in good agreement with the findings of *Lichtenfelt* [84] on SS 304L, who reported that an increased strain rate resulted in greater adiabatic heating of the material which reduced the amount of austenite being transformed to martensite through displacive transformation ,while being deformed. The heat

of deformation is retained inside the material at higher strain rates due to the poor conductivity of austenitic stainless steels.

Thus, strain rate was found to be a major contributing factor which determined the relative stability of the austenitic phase. Martensite formation enhances the work hardening capability of the steel, and therefore increases its UTS value.

The increase in Y.S. value with increase in strain rate can also be explained on the basis of the governing equation $\dot{\varepsilon} = \boldsymbol{b}\rho v$, from which it can be inferred that for materials having similar initial dislocation densities ρ (influenced by prior thermo-mechanical history) the average dislocation velocity v should increase with the imposed strain rate, which is in turn related to the flow stress as $v = A\sigma^{m'}$ [30].

It has been pointed out that the stage at which the γ-α' transformation occurs directly affects the ductility of the specimen, such that when transformation proceeds at relatively high strain values just prior to the onset of necking, higher elongation values are obtained. Whereas, for the same transformation occurring at low strain values a loss of ductility and premature

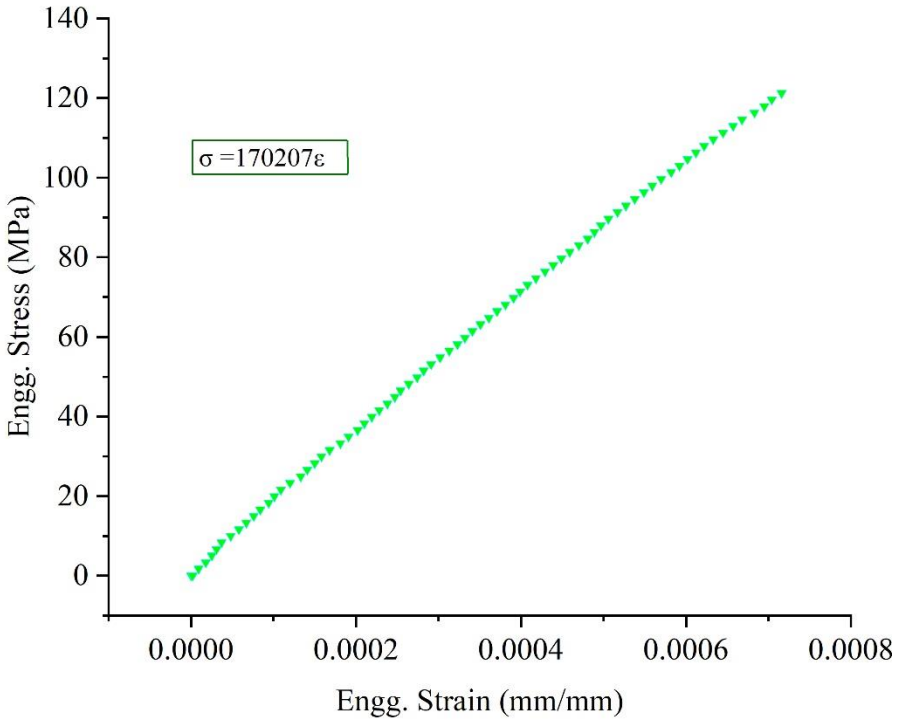

Fig 4.2 Determination of Young's Modulus

failure is observed. Thus, high values of total elongation obtained for both the cases suggest that martensite formation occurred at later stages, due to which necking was delayed.
The $M_{d,30}$ temperature, defined as the temperature at which 50% by vol. martensite formation takes place with the application of 30% true strain serves as a measure of the austenite phase stability in metastable austenitic stainless steels. The $M_{d,30}$ temperature of the present steel

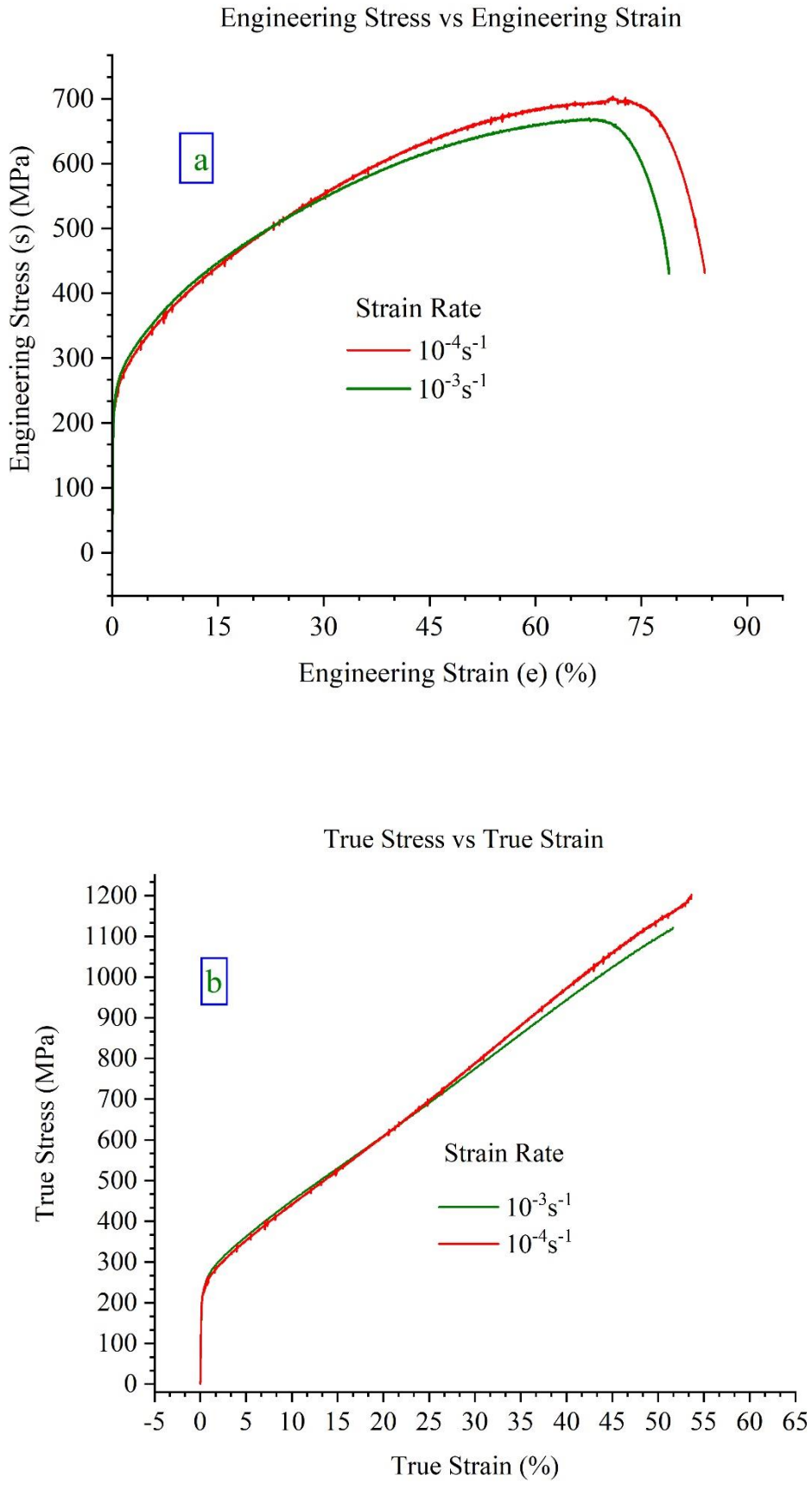

Fig 4.3 a) Engineering Stress Strain curve **b)** True Stress Strain curve of SS 304L

was calculated by using the Angel's equation (eq. **2.4**) and was found to be 39.5℃, which is well above the temperature at which the tests were carried out (~23℃), implying that substantial martensite formation had occurred during the course of the test.
The Young's modulus was determined from the slope of the linear elastic region of the tensile flow curve and the E value was found to be 170.2 GPa.

4.3 Work hardening behavior:

4.3.1 Hollomon Analysis:

The work hardening behaviour of the material has been analyzed by using the Hollomon relationship. Instead of showing a single line **Fig 4.4** delineates three distinct regions into which the curve of true stress versus true plastic strain curve can be divided. The double logarithmic plot shows multi stage work hardening behaviour that is displayed by the material. Stages-I and Stage-III have been approximated by straight lines yielding R^2>0.98 in each case. The antilogarithm of the slope and intercept of these straight lines gives the value of the strength coefficient (K) and the strain hardening exponent (n) respectively. There is a transition stage which seperates stages I and III, demarcated by the transition strains ε_1 and ε_2 respectively. This suggests that the transition between stages-I and II is not abrupt but gradual.

The transition strain values ε_1, ε_2 along the values of K and n are tabulated in **Table-4.2**.

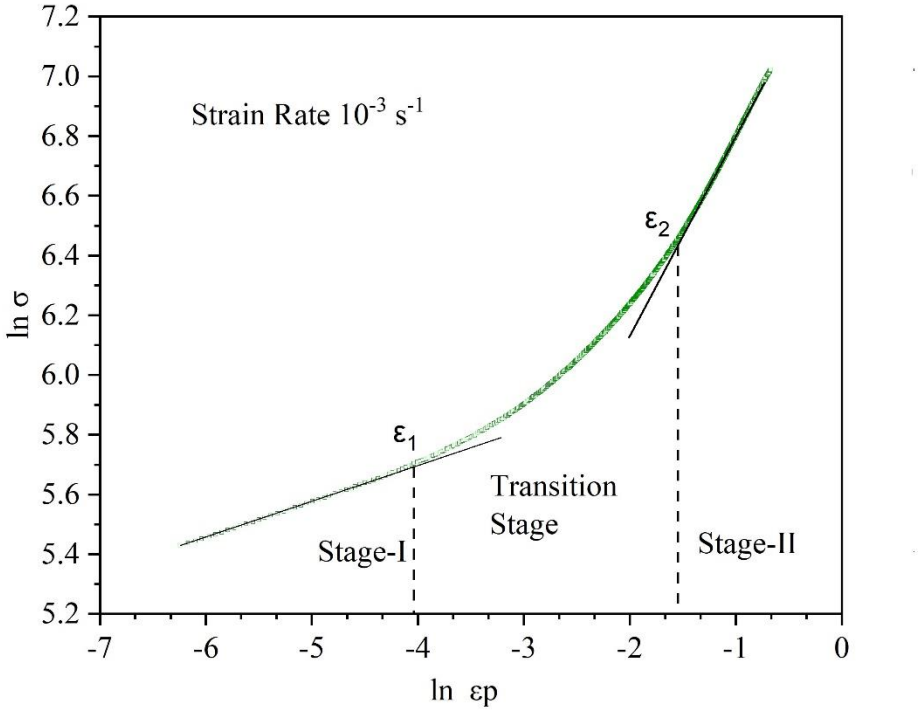

Fig 4.4 Multistage work hardening behavior of SS 304L

Table-4.2 Work hardening parameters of solution annealed AISI 304L at RT under different strain rates

Engineering Strain Rate (s^{-1})	n_1	n_2	K_1 (MPa)	K_2 (MPa)	ε_1 (%)	ε_2 (%)
0.001	0.146	0.655	550	1735	1.76	21.26
0.0001	0.137	0.675	509	1819	1.44	25.83

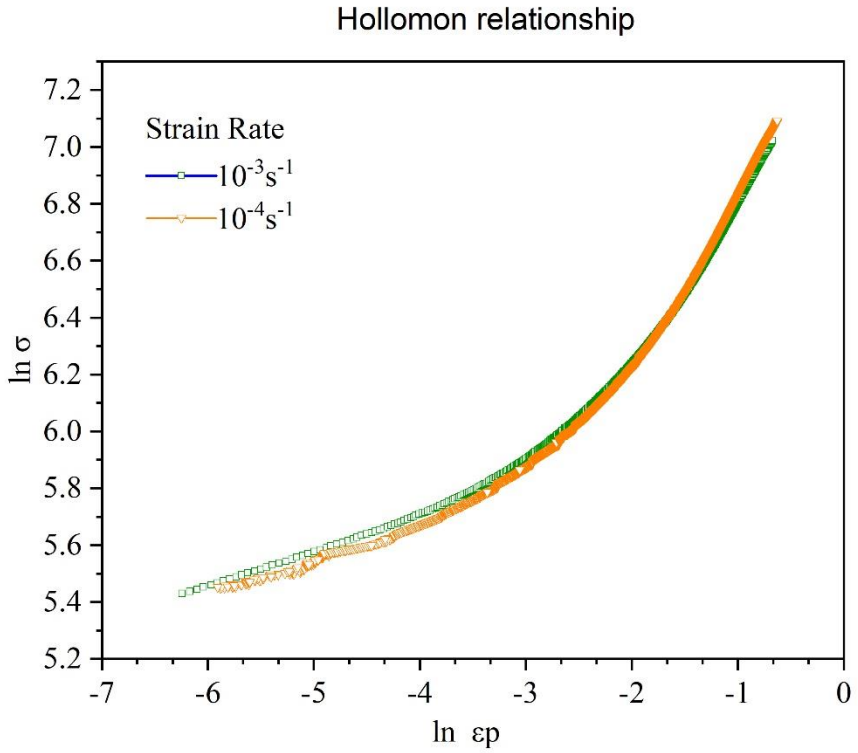

Fig 4.5 Variation of flow stress with true plastic strain at different strain rates

From the data obtained, the following observations can be made : with increasing strain rate the difference between the transition strain values for the high and low strain regimes seem to decrease in magnitude, in other words the width of the transition region $(\varepsilon_2 - \varepsilon_1)$ starts diminishing at higher strain rates. This may due to the fact that DIM formation sets in early at higher strain rates, leading to an early transition from stage-I to stage-II behaviour. The high $n_3$values obtained in region III may be ascribed to martensitic transformation which induces secondary hardening. The low n_1 values in stage-I is due to planar slip that prevails in this region due to the operation of a single slip system, bearing resemblance to the deformation behaviour of a single crystal. Conclusive evidence supporting this fact has been provided by Feaugas [85] who showed that during phase I deformation of polycrystalline 316L, majority of the grains (>50%) were found to be activated for single slip system.

During stage-II ,the rapidly increasing slope of the curve alludes to the operation of multiple slip on intersecting {111} planes and the consequent formation of Lomer-Cottrell barriers which impede dislocation motion.

4.3.2 Ludwik Analysis:

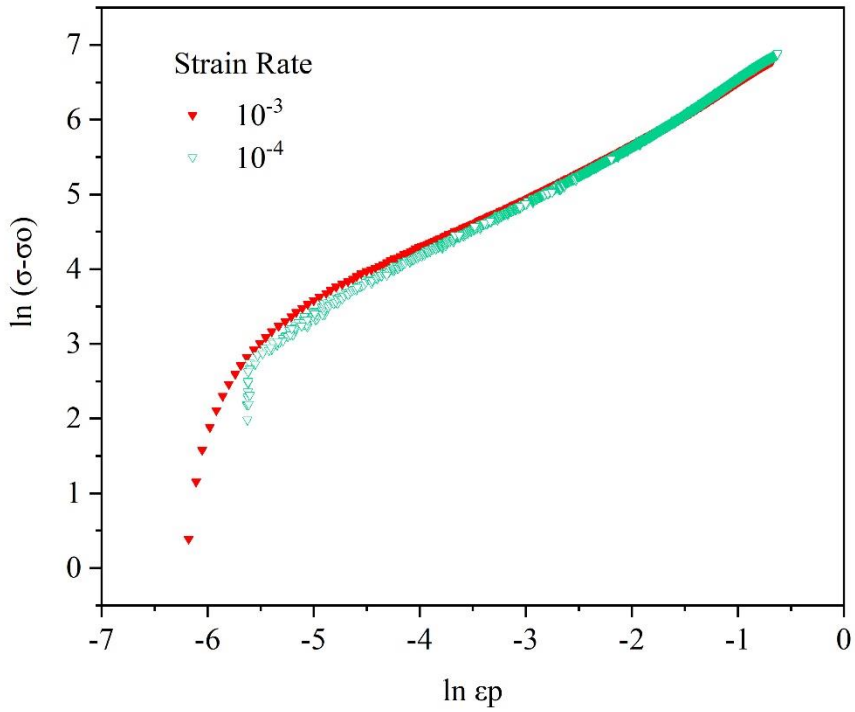

Fig 4.6 Variation of flow stress with true plastic strain as predicted by the Ludwik model

Another work hardening model is based on the Ludwik equation. **Fig 4.6** shows the plot of $\sigma - \sigma_0$ versus the true plastic strain on a double logarithmic scale, where σ_0 corresponds to the true value of the 0.2% offset yield stress obtained from the engineering stress-strain curve.
From **Fig 4.6** it is evident that the Ludwik relation is able to predict the work hardening behavior of the material satisfactorily except possibly at low strain values. Linear fitting performed for the both curves which are obtained at separate strain rates show R^2 values greater than 0.98.
The work hardening parameters obtained from the curves are presented in the following table.

Table 4.3: Work hardening parameters for the Ludwik model

Engineering Strain Rate (s^{-1})	n_L	K_L (MPa)
0.001	0.80	1477
0.0001	0.81	1513

From the table it is apparent that the strain hardening exponent predicted from Ludwik analysis remains almost constant and is insensitive to changes in strain rate.

4.3.3 Ludwigson relation:

It is evident from **Fig.4.5** that the Hollomon relation is unable to predict the work hardening behavior of SS 304L adequately, as the experimental curve shows positive deviation from linearity at low strain values. This is in general true for materials possessing low stacking fault energies such as Austenitic Stainless Steels, as has been reported by several researchers.
This positive departure from linearity presently observed in SS 304L can be attributed to its low SFE value which delays cross-slip and promotes planar glide of dislocations. This is essentially due to the larger separation distance between dissociated partials in low SFE materials which makes them difficult to recombine before they are able to cross-slip [45].
Thus, for a more accurate representation of the work hardening characteristics of the present material, the Ludwigson relation has been used to account for the experimental data throughout the entire range of strain values starting from the point of yielding upto the onset of necking.
The deviations in the Hollomon plot of the experimental data from linearity at low strain values (<0.1) are plotted against the true plastic strain in **Fig 4.7**

The dataset shows a high degree of linearity with an R^2 value of 0.999.

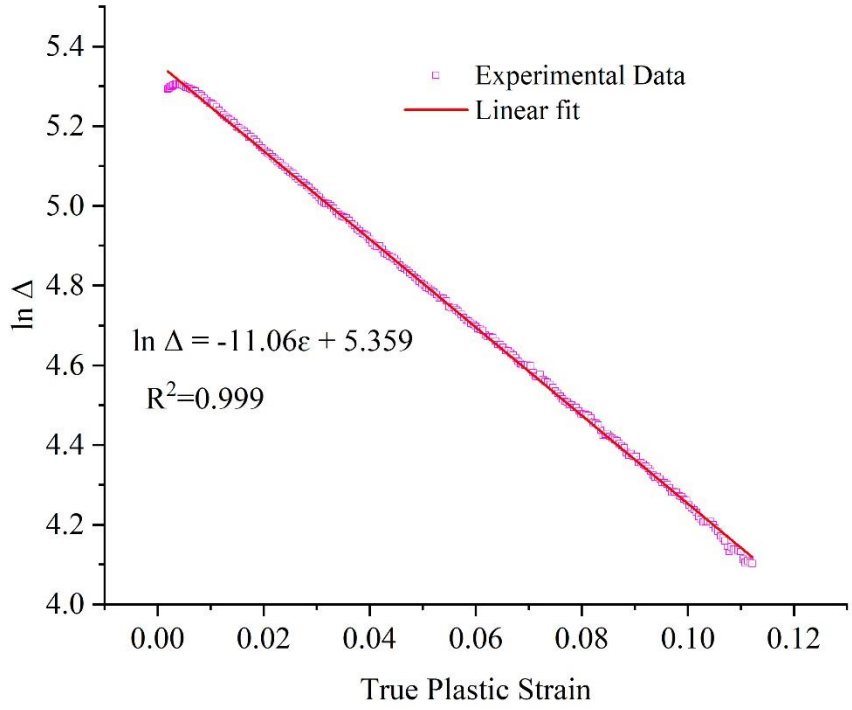

Fig 4.7 The deviations of the Hollomon behavior from linearity at low strain values (<0.1) plotted against the true plastic strain

Experimentally obtained values of all the four constants appearing in the Ludwigson relation are listed in the following table

Table 4.4: Work hardening parameters for the Ludwigson model

Engineering Strain Rate (s^{-1})	K_1 (MPa)	K_2	n_1	n_2	ε_L
0.001	1735	5.359	0.655	-11.06	0.246
0.0001	1819	5.370	0.675	-14.00	0.203

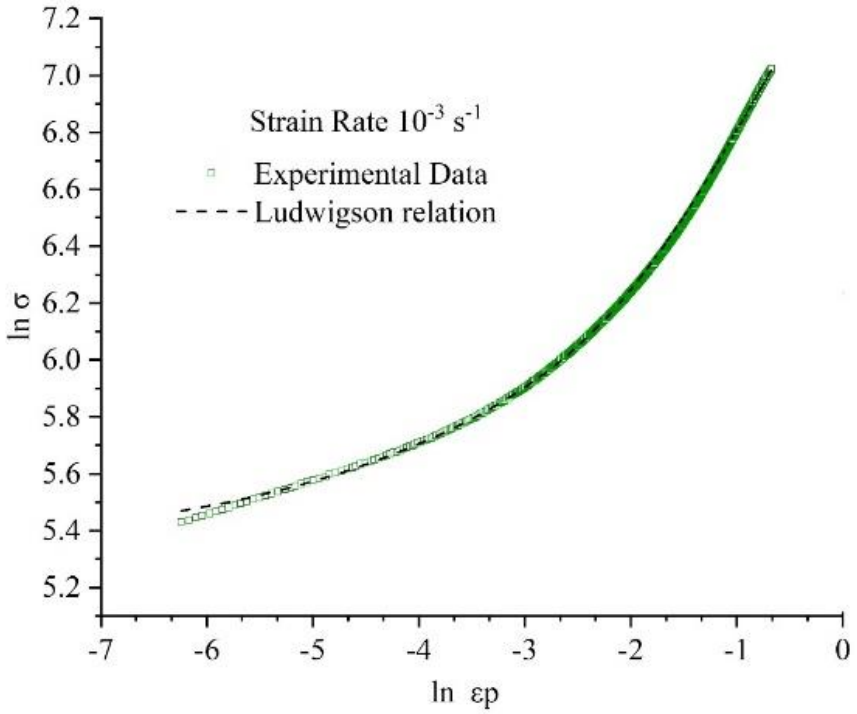

Fig 4.8 Comparison between the experimental curve and the one predicted by the Ludwigson relationship

Following Ludwigson, the transition strain value (ε_L) below which the experimental data could be satisfactorily predicted by the Hollomon relationship was obtained by setting the of $e^{(\varepsilon_L n+K_2)}/K_1{\varepsilon_L}^{n_1}$ to an arbitrary small value of 0.02.

It may noted that the K_1 and n_1 values are the same as the K_2 and n_2 values that are listed in **Table 4.2**. These represent the strength parameters for the stage-II of the Hollomon curve.

From **Fig 4.8** it can be seen that there is an excellent agreement between the experimental curve and the curve which is predicted using the Ludwigson relationship (represented by the dashed lines).

4.3.4 Differential Crussard Jaoul Analysis:

Differential C-J Analysis is based on the Ludwik relationship, where the true stress is differentiated with respect to the true plastic strain and is represented as a function of the latter on a double logarithmic scale.

From the C-J plot illustrated in **Fig 4.9**, three distinct linear portions delimited by the transition strains ε_{c1} and ε_{c2} can be discerned ,which furnish greater details on the possible deformation mechanisms that govern them.

The slope of each linear portion provides the $n_c - 1$ values, whereas the antilogarithm of the intercept at $\varepsilon_p = 0$ yields the value of the product $n_c K_c$.

While the $n_c - 1$ values for all the three regions are negative as the curve follows a downward trend, the $n_c - 1$ value for the intermediate region (Stage-II) is found to be less negative in comparison to stages I and III. No transition regions have been found that separate one stage from the next.

Table 4.5: Strain hardening exponent n_c transition strains ε_{c1} and ε_{c2} obtained from C-J analysis

Engineering Strain Rate (s^{-1})	n_{c1}-1	n_{c2}-1	n_{c3}-1	ε_{c1} (%)	ε_{c2} (%)
0.001	-0.63	-0.23	-0.94	3.59	13.04
0.0001	-0.73	-0.42	-0.73	0.7	12.88

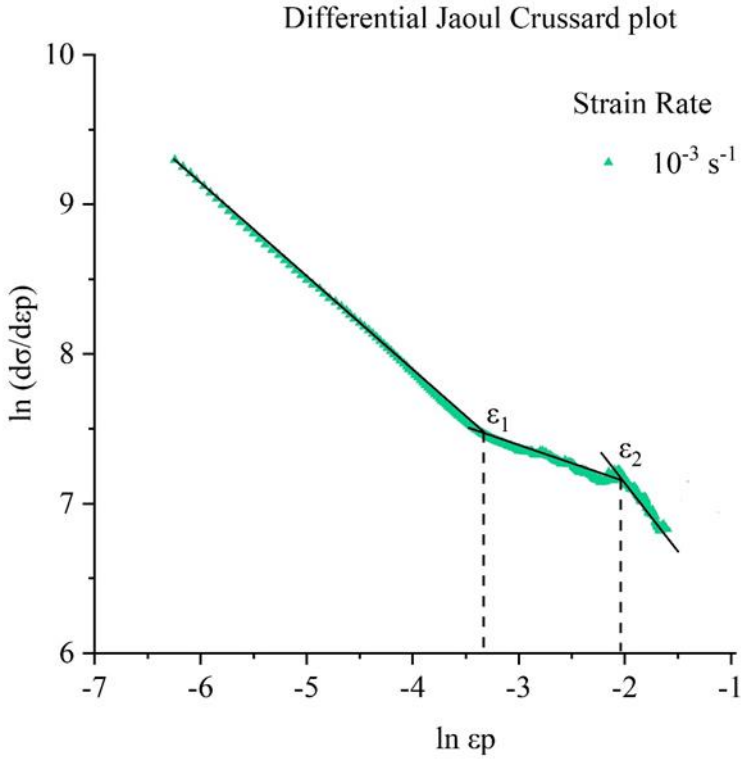

Fig 4.9 Different work hardening stages predicted by using Different Crussard Analysis

4.3.5 Kocks Mocking Analysis:

Mecking [6] pointed out that the different stages of work hardening can be better represented by the product of the work hardening rate (θ) and the true stress σ when plotted against the true stress σ.

From **Fig 4.11** it can be seen that the value of $\sigma\theta$ decreases rapidly in stage-I with increase in flow stress at low stress levels. This initial stage is often identified as a transition stage that precedes stages-II and III. During stage-II the curve gradually rises to a maxima in an almost linear fashion, before finally decreasing in stage-III.

Stage-I is a transient stage, in which both dislocation velocity and mobile dislocation density increases with true stress leading to a rapid increase in the plastic strain rate immediately after the elastic limit is surpassed.

Stage-II is associated with athermal hardening involving dislocation interactions and is insensitive to temperature.As observed by Mecking, this stage can be accurately represented by a straight line which on extrapolation may either have a negative or a positive intercept depending on whether the material being tested is a single crystal or a polycrystal . This observation holds good for SS 304L as is evident from **Fig 4.11**

During stage-III, $\sigma\theta$ decreases and starts to deviate from linearity as dynamic recovery occurs to due cross slip at room temperature.At elevated temperatures stage-III may commence early at lower stress levels to due easier cross slip. Thus, three distinct stages can be discerned from the $\sigma\theta$ versus σ plot whereas this distinction is not so apparent in the θ- σ plots.

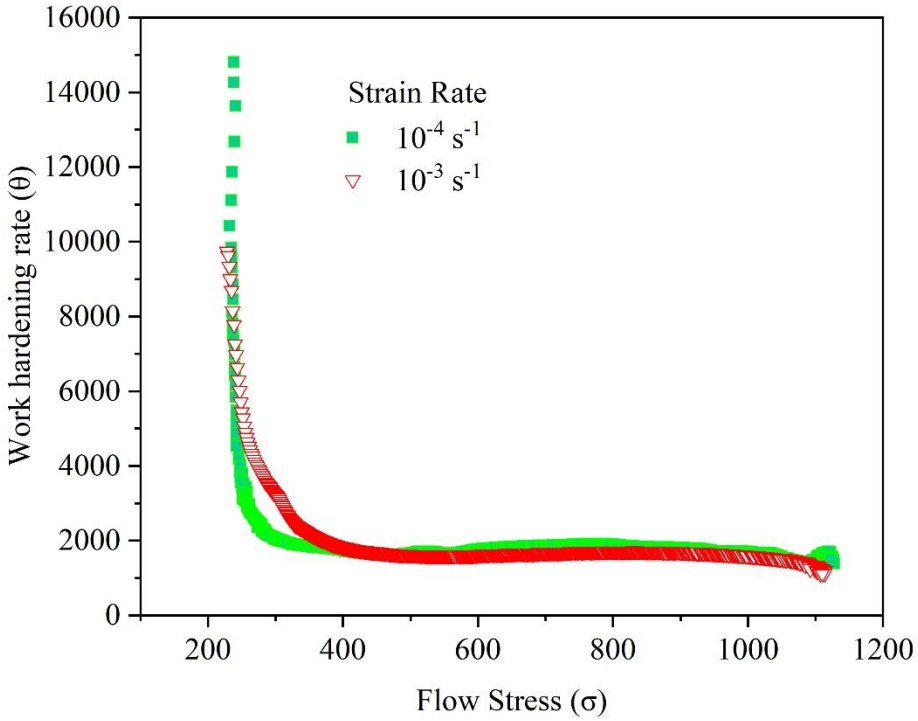

Fig 4.10 Variation of work hardening rate with flow stress at various strain rates

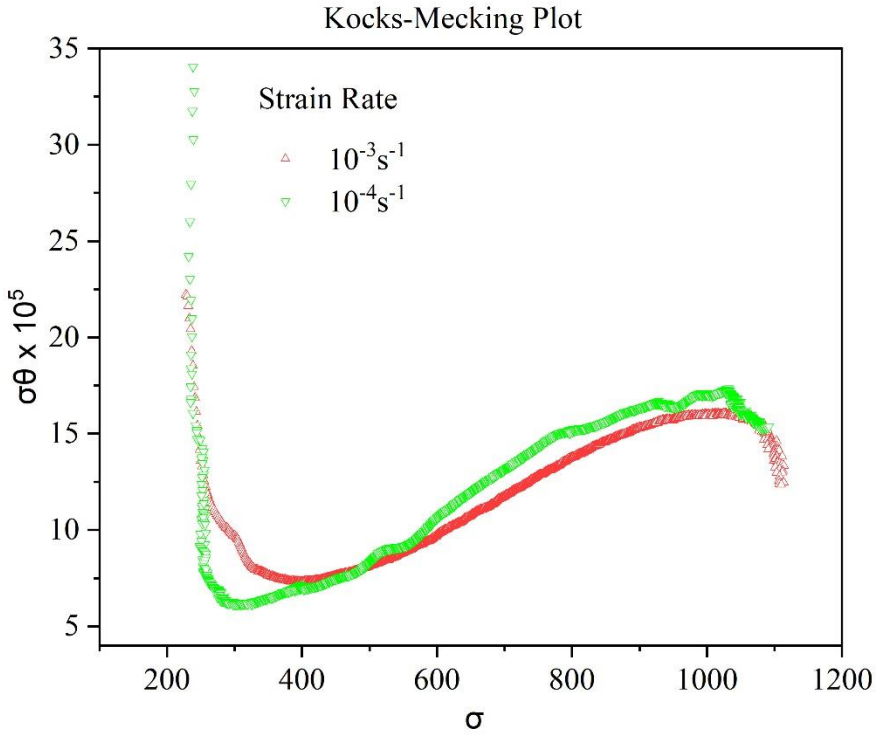

Fig 4.11 Kocks-Mecking plot of SS 304L at different stain rates

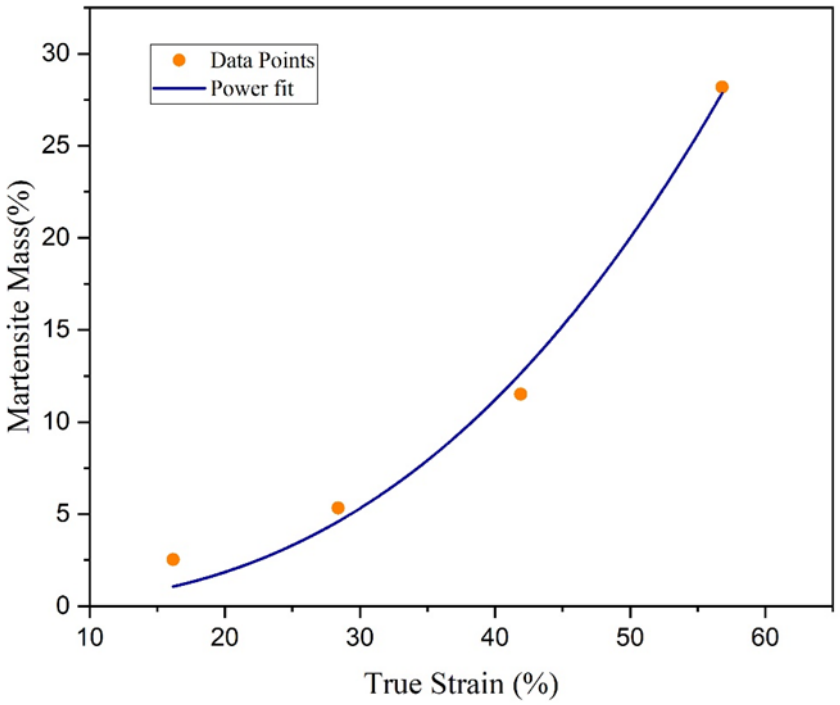

Fig 4.12 Variation in martensite mass fraction with true strain value

4.3.6 Deformation Induced Martensite (DIM) formation in monotonically deformed specimens:

Formation of Deformation induced martensite in austenitic stainless steels is well known in austenitic stainless steels , **Fig 4.12** shows that the martensite mass fraction increases rapidly in a non-linear fashion with increasing values of true strain. The mass fractions were obtained from ferritoscopic measurements after performing interrupted tensile tests in which the specimens were monotonically deformed upto a predetermined strain value followed by which they were unloaded. The increasing trend of martensite phase fractions with increasing values of true strain is similar to the observations that were reported by Talonen [40] , who found that for 304 austenitic stainless steels tested at low strain rates ($< 3 \times 10^{-3}\ s^{-1}$),the martensite phase fraction increased rapidly for strain values below the uniform strain, and did not demonstrate a sigmoidal behavior unlike other grades (such as 301LN) in which a saturation in martensite content was observed just prior to failure.

4.4 Fractography of monotonically deformed samples

SEM micrographs were obtained from the fracture surfaces of the specimens which had failed under monotonic tensile loading at different strain rates.

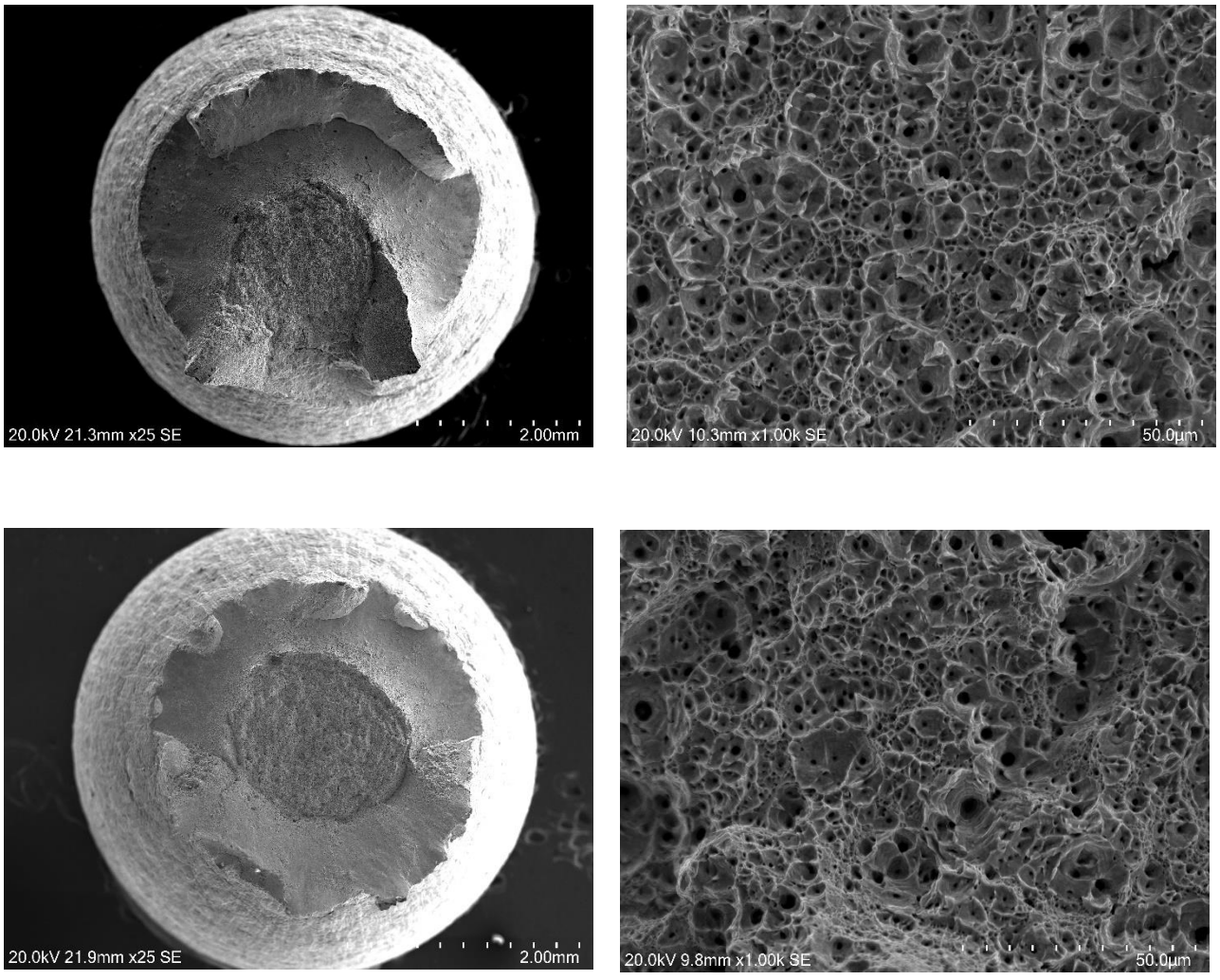

Fig 4.13 Fracture morphology of AISI 304L monotonically deformed at a strain rate of **(a)**,**(b)** $10^{-3}s^{-1}$ and **(c)**,**(d)** $10^{-4}s^{-1}$

The micrographs reaveal that the specimen had failed through microvoid coalascence at both the strain rates, which is the typical mode of ductile fracture.A closer look at the fracture morphology suggests that the average size of the dimples change with strain rate, such that at lower strain rates the dimple networks become finer, but as the strain rate is increased these fine networks are gradually replaced by larger dimples. It has also been found that a larger number of small sized dimples increases both the strength and ductility of the specimen [86]. These findings concur with the tensile test results of 304L steel which also indicate that for the specimen tested at a lower strain rate of $10^{-4}s^{-1}$ both the tensile strength and ductility values are slightly higher than the one tested at $10^{-3}s^{-1}$.

4.5 LCF behavior of SS 304L at Room Temperature:

4.5.1 Dependence of fatigue life on strain amplitude:

The fatigue lives of SS 304L at different strain amplitudes have been determined through multi-specimen low cycle fatigue tests that were carried out at room temperature. The plastic as well as the elastic strain amplitudes after the stabilization of stress response following the initial 40 cycles have been listed in **table 4.6**. From **Fig 4.16** it can be seen that the 40th cycle lies in a region of stable stress response, and was thus suitably chosen for identifying the stable hysteresis loops for the present investigation.

It has been noted that with an increase in total strain amplitude $\Delta\varepsilon_t/2$ that is imposed, the fatigue life reduces significantly, whereas the stable true stress amplitude $\Delta\sigma/2$, along with the elastic and plastic strain amplitudes $\Delta\varepsilon_p/2$ and $\Delta\varepsilon_e/2$ all increase simultaneously.

Table 4.6: Low cycle fatigue test results of 304L stainless steel at room temperature

Total Strain Amplitude $\left(\frac{\Delta\varepsilon_t}{2}\right)$	True Stress Amplitude $\left(\frac{\Delta\sigma}{2}\right)$	Plastic Strain Amplitude $\left(\frac{\Delta\varepsilon_p}{2}\right)$	Elastic Strain Amplitude $\left(\frac{\Delta\varepsilon_e}{2}\right)$	No. of cycles to failure (N_f)	No. of reversals to failure $(2N_f)$
0.0035	273	0.00198	0.00152	38575	77150
0.005	290	0.00336	0.00164	4214	8428
0.0075	333	0.00549	0.00201	880	1760
0.01	373	0.00771	0.00229	329	658
0.012	412	0.00942	0.00258	269	538

4.5.2 Cyclic stress strain behaviour

The cyclic stress strain curve (CSSC) of SS 304L has been obtained by plotting the stable cyclic stress amplitudes against the plastic strain amplitudes that are listed in **table 4.6** on a double logarithmic scale.

Fig 4.14 shows the bilinear nature of the cyclic stress strain curve as it monotonically increases with plastic strain amplitude. It can be seen that the variation in cyclic stress amplitude is greater in stage-II which is reflected in the significantly higher values of K' and n' that are obtained through curve fitting, in comparison to stage-I. This two-stage cyclic deformation behavior may be attributed to substantial martensite formation at strain amplitudes above $\pm$0.5%. Similar findings have been reported by other investigators [87] who observed a two phase Coffin-Mansion behavior in coarse grained 316 LN austenitic stainless steel. Sivaprasad et al [63] also found that a single power law relationship could not adequately represent the cyclic stress strain behavior in SS 304LN over the entire range of plastic strain amplitudes. Thus, the metastable nature of the austenite phase for the investigated steel at room temperature may be the reason for bilinearity of its CSS curve.

The values of cyclic strain hardening exponent n' and the cyclic strength coefficient K' have been determined from the slope and ordinate intercept of the straight lines fitted by the method of least squares. Their values are presented in **table 4.7**

Table :4.7 Cyclic properties of SS 304L at room temperature

Cyclic strength coefficient (K'_1) (MPa)	Cyclic strain hardening exponent (n'_1)	K'_2	n'_2
507	0.09	2125	0.35

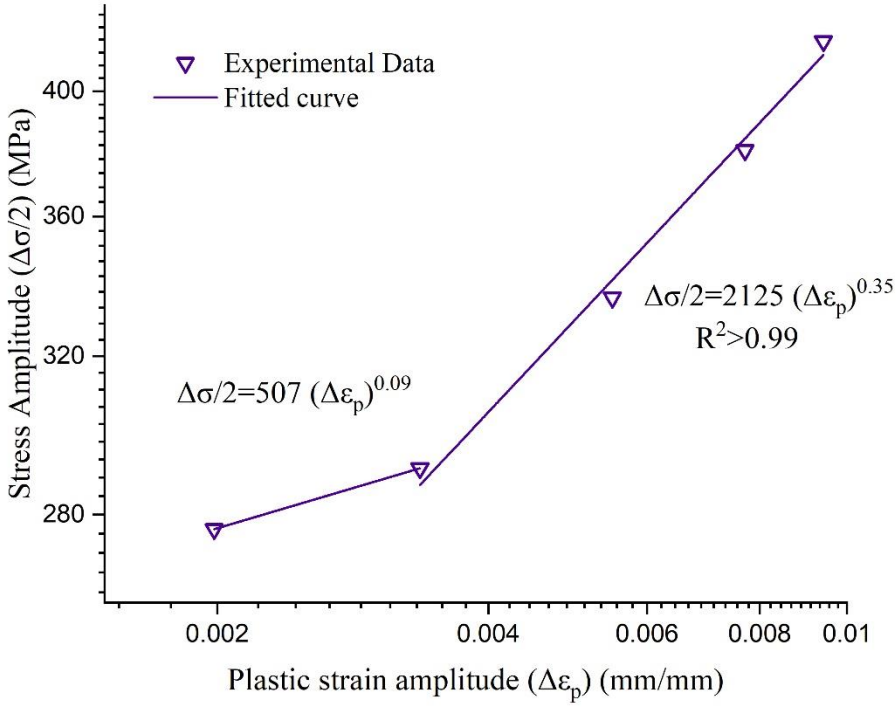

Fig 4.14: Bilinear nature of the cyclic stress strain curve (CSS) for SS 304L

4.5.3 Strain-Life Behaviour

The strain life data presented in **Table 4.6** has been analysed on the basis of Coffin-Mansion and Basquin relationships. The strain amplitude variation for the 40th cycle with the number of reversals to failure has been shown in **Fig 4.15** on a double logarithmic scale.

Both the C-M and Basquin relationships predict a linear variation of strain amplitude with fatigue life when plotted on a logarithmic scale. **Fig 4.15** clearly depicts that the fatigue life decreases with an increase in elastic as well as plastic strain amplitudes as the material closely follows both the C-M and Basquin relationships with R^2 values of 0.97 and 0.89 respectively. The cyclic properties of SS 304L, namely the fatigue strength coefficient ($\sigma_f{}'$), the fatigue strength exponent (b), the fatigue ductility coefficient ($\varepsilon_f{}'$) and the fatigue ductility exponent (c) have been calculated from the slope and intercept values obtained from the plots.

Table 4.8 : Coefficients and exponents of C-M and Basquin relationships

fatigue strength coefficient (σ_f') (MPa)	869
fatigue strength exponent (b)	-0.11
fatigue ductility coefficient (ε_f')	0.078
fatigue ductility exponent (c)	-0.35

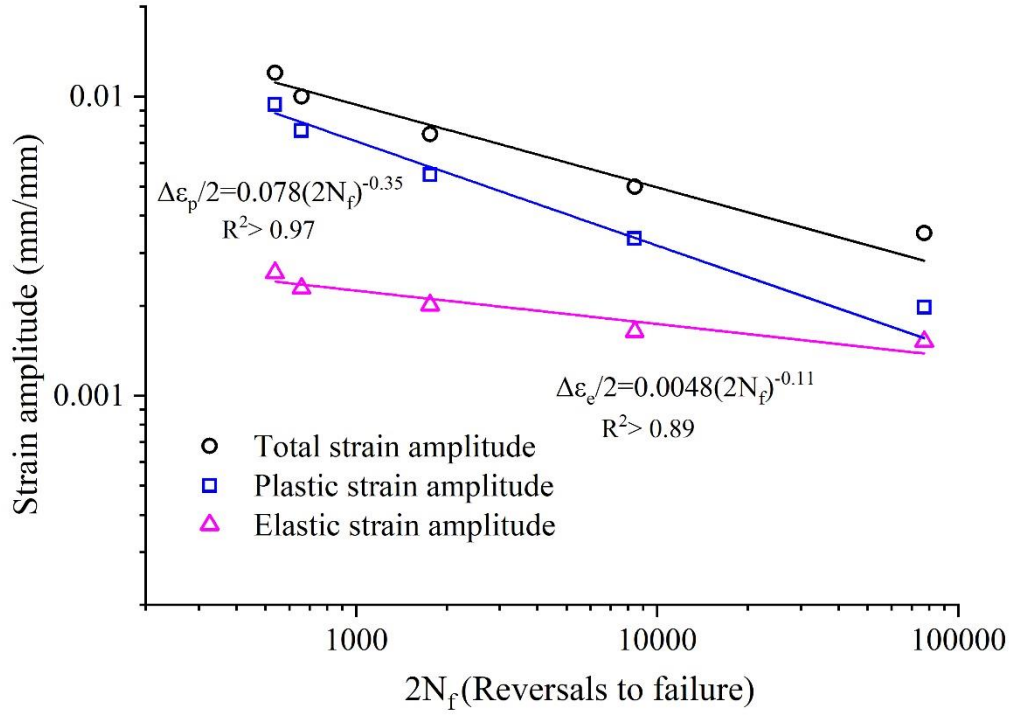

Fig 4.15: Variation of total, plastic and elastic strain amplitudes with the number of reversals to failure

4.5.4 Cyclic stress response

The cyclic stress response of the material has been analysed by plotting the peak stress values for each loading cycle against the number of cycles in a semi-logarithmic scale.

From the stress response curves, it can be seen that the material undergoes cyclic hardening (the peak stress increases) during the initial 10-15 cycles before reaching a steady state. This primary hardening occurs due to the increase in flow stress that is required to maintain the imposed strain rate. As the dislocation density in the annealed condition is generally low, the applied strain rate can only be matched if the average dislocation velocity increases, which in turn requires an increase in flow stress. After the dislocations start moving, they interact among themselves, creating new dislocations (both glissile and sessile) that act as barriers or obstacles to the movement of other dislocations and give rise to the initial hardening that is observed for all the strain amplitudes. However, for the strain amplitudes $\pm$0.35% and $\pm$0.5% the initial hardening phase is followed by cyclic softening before it finally undergoes secondary hardening due to the formation of Deformation Induced Martensite (DIM).

This cyclic softening may occur due to dislocation annihilation, or dislocation rearrangement into stable low energy configurations such as dislocation channels, vines or cells that offer less resistance to plastic deformation.

Secondary hardening is most pronounced for the strain amplitude of $\pm$1.2% followed by $\pm$0.75%, $\pm$0.5% and $\pm$1% in succession. The stress response curve for $\pm$0.35% does not show any secondary hardening and undergoes continuous softening instead. In each case, there appears to be a rapid decline in stress response after the secondary hardening phase, following which the material fails.

The region of stability observed for the strain amplitudes of $\pm$0.75% and $\pm$1% can also be attributed to martensitic transformation which suppresses cyclic softening and provides a stable stress response ,along with other contributing factors such as the formation of a low energy dislocation cell structure due to the activation of secondary slip systems. Cyclic softening is only observed at a strain amplitude of $\pm$0.35%.

The cyclic hardening or softening behaviour of a material is dependent upon its prior loading history. As a general rule of thumb, a hard material is expected to undergo cyclic softening whereas a soft material would undergo cyclic hardening.

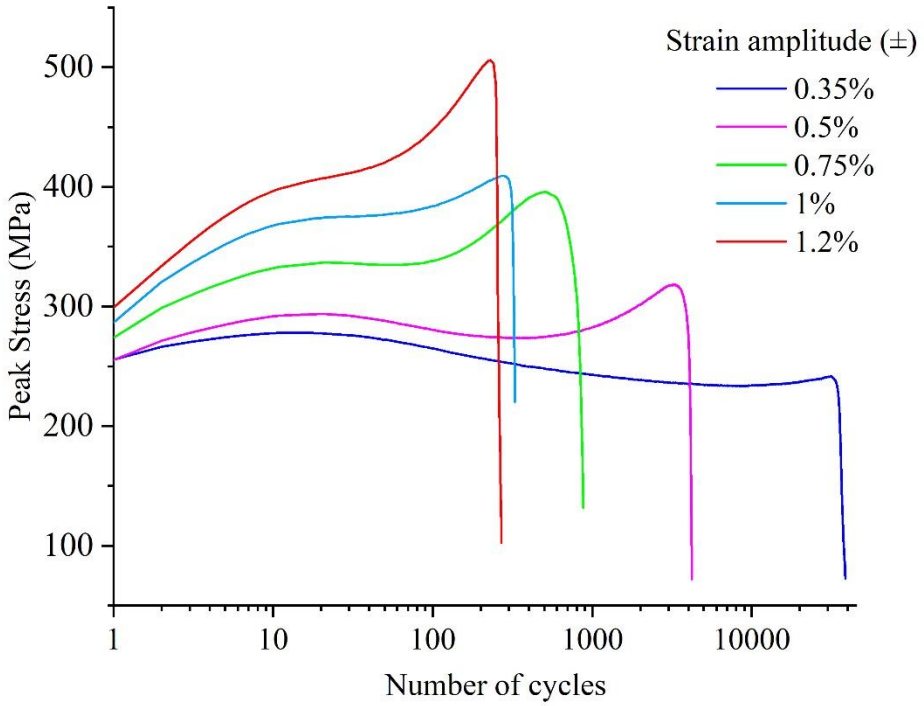

Fig 4.16: Cyclic stress response curves at various strain amplitudes

For the present analysis the degree of secondary hardening were calculated from the stress response curves of SS 304L and their values have been listed in **Table 4.8**

Table 4.9 Secondary hardening characteristics of SS 304L

Strain amplitude $(\Delta\varepsilon_t/2)$	Secondary hardening(H_s) $\sigma_{max} - \sigma_s$	Degree of secondary hardening	Rate of secondary hardening
0.012	91	0.21	0.476
0.01	36	0.09	0.150
0.0075	62	0.18	0.146
0.005	45	0.14	0.016
0.0035	8	0.03	0.033

It can seen from **Table 4.8** that the degree of secondary hardening is the highest for the strain amplitude of $\pm 1.2\%$ and declines with the decrease in strain amplitude. However, an exception to this behavior is observed in case of $\pm 1\%$,which undergoes a lesser degree of secondary hardening in comparison to $\pm 0.75\%$ and $\pm 0.5\%$. A cursory glance at the rate of secondary hardening values reveal that the hardening rates at $\pm 0.5\%$ and $\pm 0.75\%$ are almost identical, but due to the greater number of cycles taken to reach the maximum stress (at the end of the secondary hardening phase) at lower strain amplitudes, the extent of hardening is more. It can thus be stated that due to the premature failure of the specimen at $\pm 1\%$ sufficient secondary hardening was not observed. The H_s values were calculated as the difference between the maximum stress value reached at the end of the secondary hardening phase (σ_{max}) and the saturation stress that was observed after the initial hardening. The secondary hardening rates were calculated by dividing the Hs values by the number of cycles that were required to attain σ_{max} from σ_s at the stabilized condition.

4.5.5 Strain Ratio

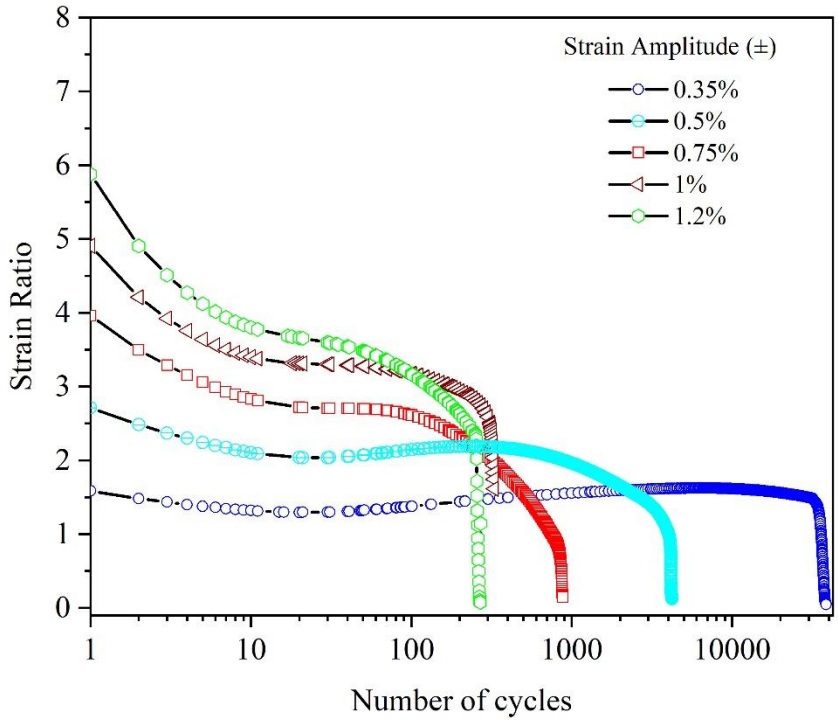

Fig 4.17: Variation of strain ratio (S.R.) with the number of cycles at various strain amplitudes

The cyclic hardening or softening behaviour of a material can also be understood from the variation of strain ratio (S.R.), which is defined as the ratio of the plastic and elastic strain amplitudes $\Delta\varepsilon_p/\Delta\varepsilon_e$ for any individual cycle as the material is cyclically strained . The concept of S.R. was introduced by Paul et al [55] who pointed out that since the elastic strain amplitude was directly proportional to the stress amplitude (in accordance with Hooke's law), any change in the latter is reflected in the strain ratio.

Fig 4.17 shows the variation of strain ratio with the number of cycles in a semi-logarithmic scale During the initial 10-15 cycles, the material underwent cyclic hardening as reflected by the decrease in strain ratio with increasing number of cycles. This can be interpreted as an increase in peak stress (or stress amplitude) value with cyclic straining. Beyond the primary hardening phase, a region of stability or saturation was noted for all the strain amplitudes and was most prominent for the strain amplitude of $\pm 0.35\%$ where the strain ratio remained almost constant. An exception to this behaviour was found for the strain amplitude of $\pm 1.2\%$ where it decreased continuously. The plateau or region of stability was followed by a sharp decline in the strain ratio due to secondary hardening.

4.5.6 Hardening factor

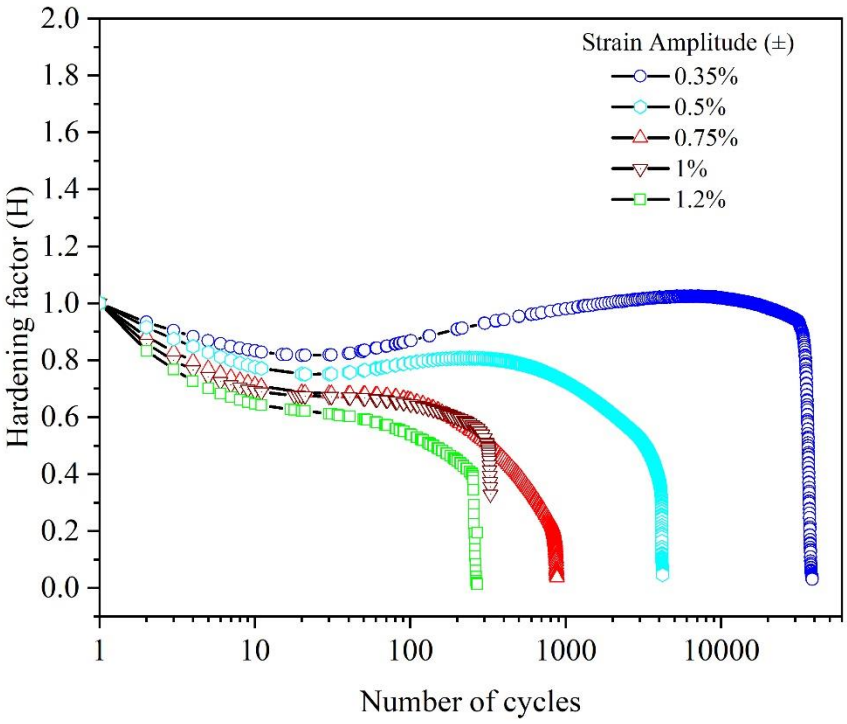

Fig 4.18: Variation of hardening factor with the number of cycles at various strain amplitudes

Another parameter that has been used to analyse the material response to cyclic straining is the hardening factor (H), which is defined as the ratio of the strain ratio corresponding to any individual cycle to the strain ratio of the first cycle $H = SR_i/SR_1$.

A hardening factor H<1indicates cyclic hardening whereas values greater than unity imply cyclic softening. The variation in hardening factor is analogous to that of the strain ratio.
During the first 10-15 cycles, the H value decreases below unity and cyclic hardening occurs for all the strain amplitudes. This is followed by an intermediate phase which is characterised by a more or less constant H value before it drastically reduces in the final stage. This intermediate phase is not displayed at $\pm 1.2\%$ as in this case the H values are found to decrease continuously.

4.5.7 Degree of hardening

Another parameter which can be used to compare the relative magnitudes of the initial hardening that occurs at different strain amplitudes is the degree of hardening (H_e) which is expressed by the relationship $H_e = (\sigma_a^s - \sigma_a^1)/\sigma_a^1$, for strain controlled tests.
Here, σ_a^s and σ_a^1 correspond to the stress amplitudes at saturation, and the first cycle respectively.

Fig 4.19 shows that there is a strong correlation between the degree of hardening and the applied strain amplitude, and a linear relationship can be established between the two. Furthermore, the degree of hardening is found to be positive for all the strain amplitudes indicating that primary hardening had occurred in each case irrespective of the strain amplitude at which the specimens were cycled. Such a linear variation in H_e values with the applied strain amplitude has previously been reported in other austenitic stainless steels such as SS 316, and SUS304-HP [57] in addition to SS 304L

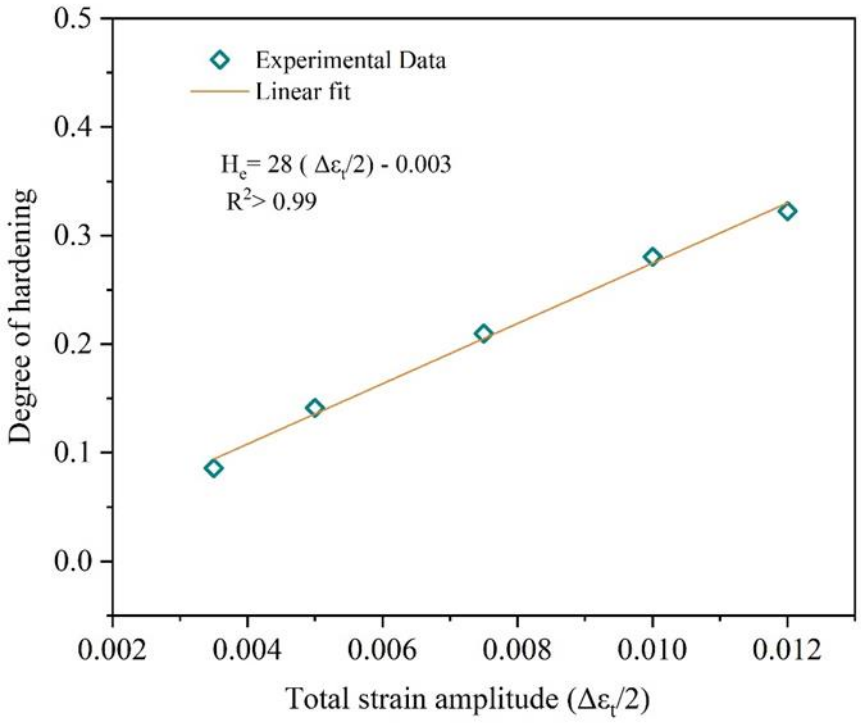

. **Fig 4.19:** Dependence of the degree of cyclic strain hardening on the imposed strain amplitude

4.5.8 Hysteresis Loops

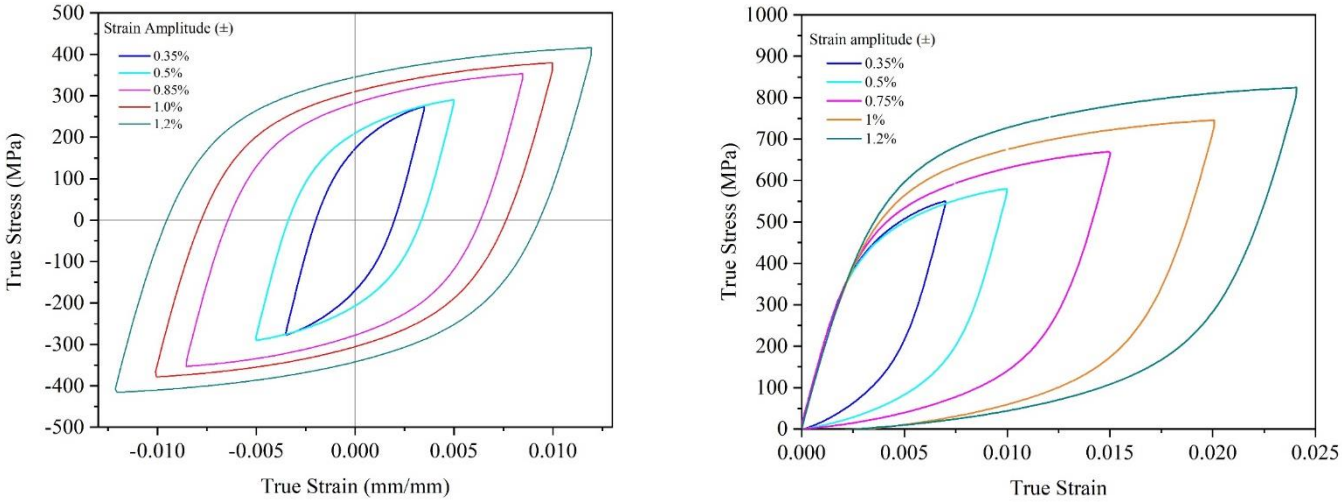

Fig 4.20: (**a)** Stress strain hysteresis loops of SS 304L at different strain amplitudes **,(b)** Stable stress strain hysteresis loops with their compressive tips shifted to the origin

The stable stress strain hysteresis loops for different strain amplitudes corresponding to the 40th cycle have been represented in **Fig 4.20(a)** It is evident that the area by the loops increase with an increase in strain amplitude

4.5.9 Masing characteristics

To study the masing characteristics of SS 304L, the compressive tips of the stable hysteresis loops corresponding to each strain amplitude were shifted to a common origin.
From **Fig 4.20(b**) it can be seen that the material displays a non-masing behaviour at room temperature for the multi-specimen loading scheme. Similar results on SS 304LN were reported by Sivaprasad [55] who observed that the material exhibited non-masing behaviour for each of the three loading schemes, namely for constant amplitude cycling, decremental step test and incremental step test, where only the degree of deviation from masing behaviour seemed to differ. It has been pointed out by Christ and Mughrabi [88] that phase stability is one of the vital requirements for a material to display masing behaviour. Here stability implies both microstructural stability as well as a stable dislocation substructure. Masing behaviour is also dependent on the prior loading history of a material as evidenced by the display of Masing behaviour in 304LN after being 30% cold rolled prior to being tested [64].
In light of the above discussion it can be inferred that the metastable nature of the austenitic phase contributes to the non-masing behaviour which is observed in SS 304L at room temperature.

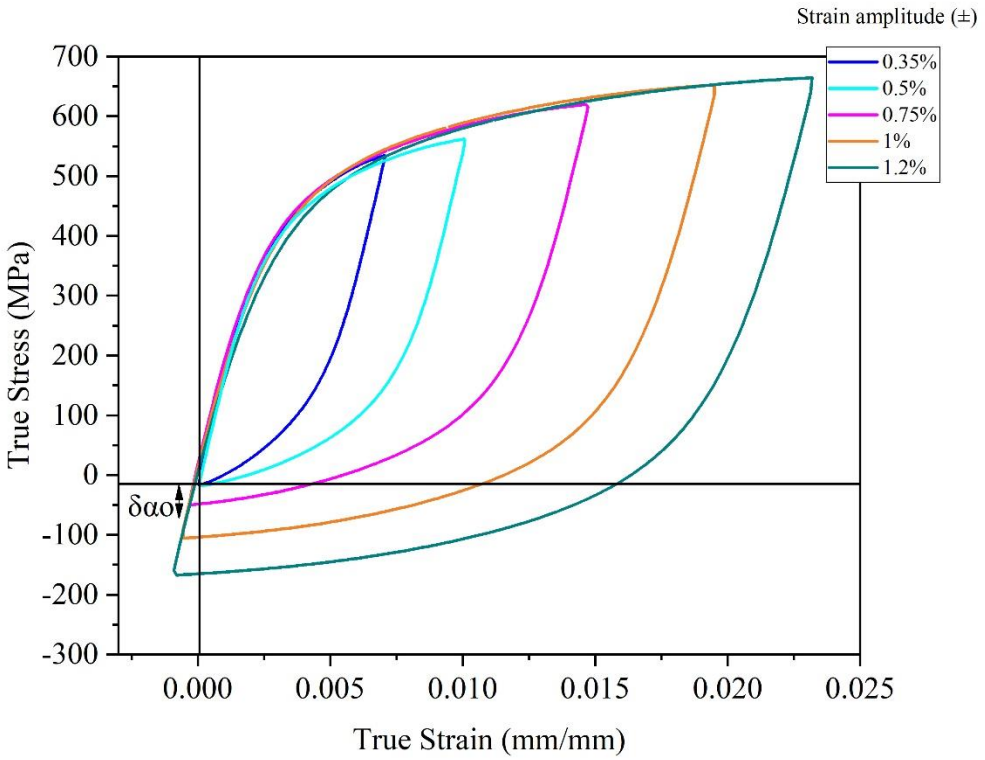

Fig 4.21: Loops translated along the elastic portion of the lowest strain amplitude loop so that the loading branches of all the loops coincide into a single curve

To find the degree of deviation from masing behaviour, the loading branches of all the stable

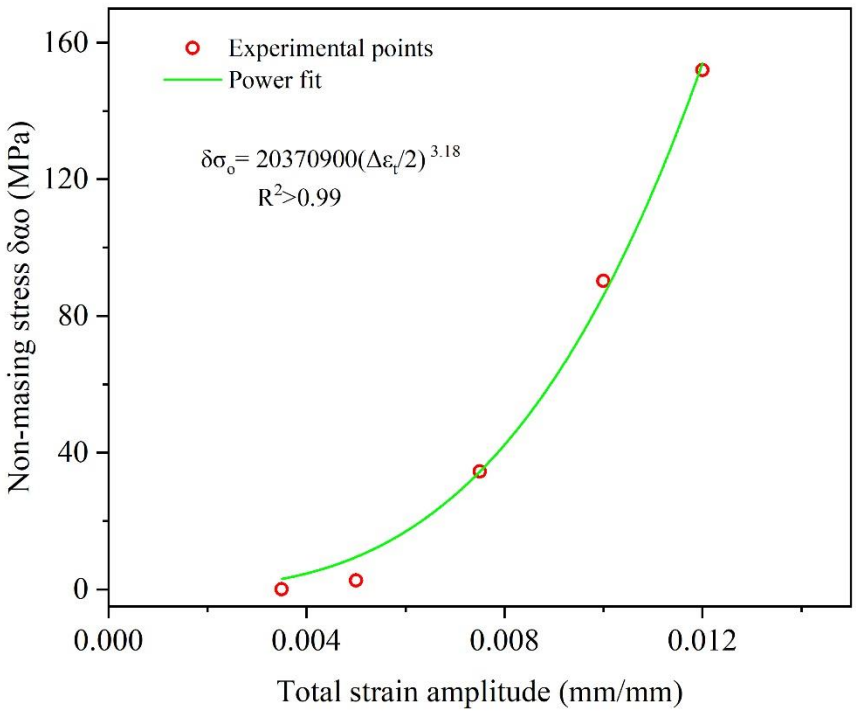

Fig 4.22: Variation of non-masing stress with strain amplitude

hysteresis loops were translated along their linear elastic portions until they merged into a single curve.
The magnitude or the amount of translation required to make the loading branches of the loops coincide corresponds to the non-masing stress $\delta\alpha_o$,which represents the increase in proportional stress range of the material with increasing strain amplitude.
It can be seen from **Fig 4.21** that a single master curve can be drawn which encompasses the loading branches of the translated hysteresis loops.

The equation of the master curve referred to the translated coordinate system is given as $\frac{\Delta\varepsilon^*}{2} = \frac{\Delta\sigma^*}{2E} + \left(\frac{\Delta\sigma}{2K^*}\right)^{\frac{1}{n}^*}$, where the values of K^* and n^* which were established through curve fitting have been listed below

Table:4.10 Master curve parameters for SS 304L

K^*(MPa)	670
n^*	0.15

Table: 4.11 The measured values of non-masing stress $\delta\alpha_o$ at different strain amplitudes are listed below:

Strain Amplitude (%)	Non-masing stress (MPa)
0.35	0
0.5	2.57
0.75	34.55
1	90.3
1.2	152.016

Fig 4.22 shows that the non-masing stress increases with strain amplitude in a non-linear fashion, following a power law relationship. Similar observations were made by Sivaprasad [55] on the variation of non-masing stress with strain amplitude in SS 304LN. It can also be qualitatively seen from **Fig 4.20 (b)** that the difference between the loading branches of the hysteresis loops increase as the strain amplitude increases, resulting in higher non-masing stress values at higher strain amplitudes. Furthermore, it is important to note that at low values of strain amplitude (0.35% and 0.5%) the material displays a near masing behaviour.

4.5.10 Plastic Strain Energy Density

Cyclic plastic strain energy density (PSED) is defined as the average plastic strain energy which is absorbed by the material per unit volume in each cycle.

The PSED values have been calculated from the actual area of the hysteresis loops at selected cycles and are plotted against the cycle number, for each strain amplitude in **Fig 4.23**

It can be seen that the PSED (ΔW_p) values are relatively constant over the entire range of cycles for all the strain amplitudes, except at 1.2% in which there appears to be a marked increase in the energy absorbed at higher cycles. This increase may be due to secondary hardening brought about by martensitic transformation at a later stage. Similar observations pertaining to the cyclic plastic strain energy density has been made by Xiaoyan et al.[69] who reported that the ΔW_p value does not vary significantly with life in fully reversed strain-controlled low cycle fatigue tests.

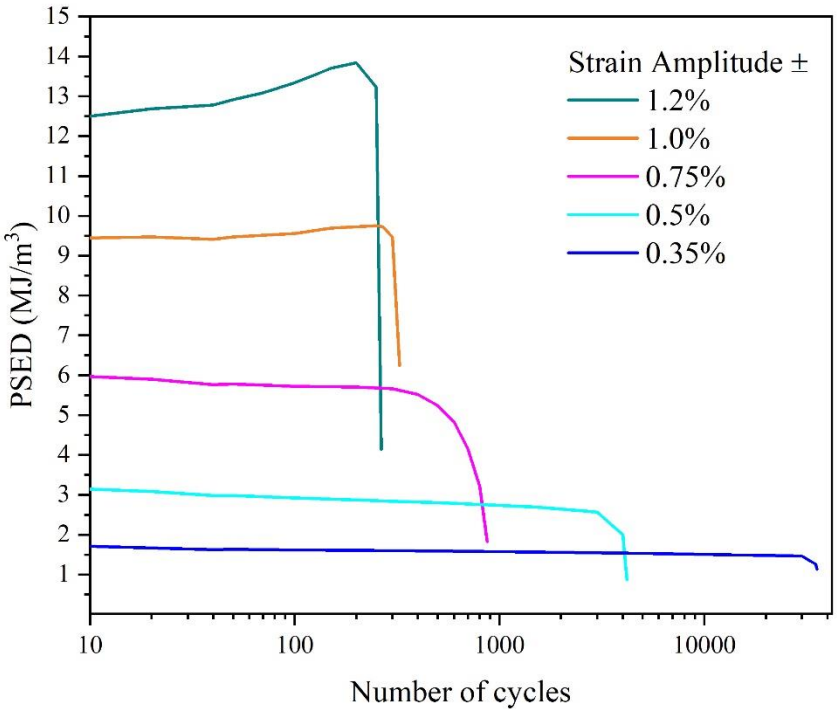

Fig 4.23. Variation of PSED with cycle number

Lee et al. [89] has demonstrated that the plastic strain energy approach can be effectively used for materials which do not attain cyclic stability, and continue to undergo cyclic softening or hardening when cyclically strained.

This is due to the fact that the ΔW_p value remains unaffected by changes in stress response brought about by mutual interaction between dislocations, increase in dislocation density, formation of dislocation cell structures etc. and is known to stabilize within 10% of the total fatigue life.

4.5.11 Average plastic strain energy density

The average strain energy density $\Delta \bar{W} p$ is often used as a parameter to characterise fatigue damage and is useful in predicting the fatigue life of a component. The importance of using energy as a parameter for characterising fatigue damage was put forward by Morrow and Feltner [66] and by later Halford [90].

Analytical expression for $\Delta \bar{W} p$ predict that a Coffin-Manson type power law relationship exists between $\Delta \bar{W} p$ and the fatigue life which can be expressed as:

$\Delta \bar{W}_p = W_f'(2Nf)^{\omega}$

Where W_f' is the fatigue toughness coefficient, and ω is the plastic strain energy exponent.

Table 4.12

W_f'	ω	b+c
261	-0.49	-0.46

Morrow and Tuller [91] have analytically established the relationship $\omega = b + c$ between ω and the exponents c and b appearing in the C-M and Basquin relationships. Their values have been compared in **Table 4.12** and both are in good agreement with each other.

The values of W_f' and ω have been determined by fitting equation **2.16** to the experimental

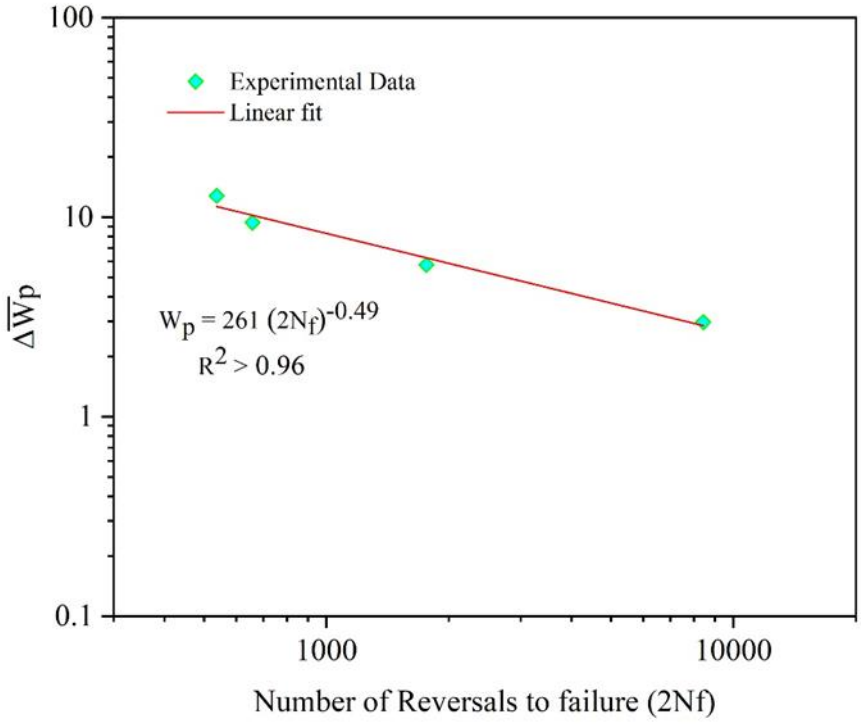

Fig 4.24: Average plastic strain energy. plotted against the number of reversals to failure

values of $\Delta\overline{W}_p$. An interesting pattern is observed in **Fig 4.24** as it is found that the average plastic strain energy density increases as the fatigue life decreases at higher strain amplitudes, implying that more energy is absorbed by the material per cycle.

4.5.12 Fatigue Toughness

Another parameter which has been used to characterise fatigue damage is the cumulative or total strain energy that is absorbed by the material until fracture which is termed as the fatigue (W_f). The fatigue toughness of a material serves a measure of its internal resistance to damage against fatigue loading.

For the present analysis, the W_f values have been estimated by multiplying the average cyclic plastic strain energy density $\Delta\overline{W}_p$ with the number of cycles to failure (N_f) at each strain amplitude. An interesting observation which can be made by comparing Figures **4.24 & 4.25** is that while the average plastic strain energy absorbed per cycle decreased with the increase in fatigue life (or the decrease in strain amplitude a reverse trend is observed for the variation in fatigue toughness values, implying that the accumulation of plastic strain energy was higher at lower strain amplitudes.

It is known from previous research works [92] that the fatigue crack initiation phase marked by stable ΔW_p values, occupies a significant portion of the fatigue life (>80%) for each strain amplitude. It can thus be concluded that higher cumulative plastic strain energy is required for fatigue crack initiation at lower strain amplitudes.

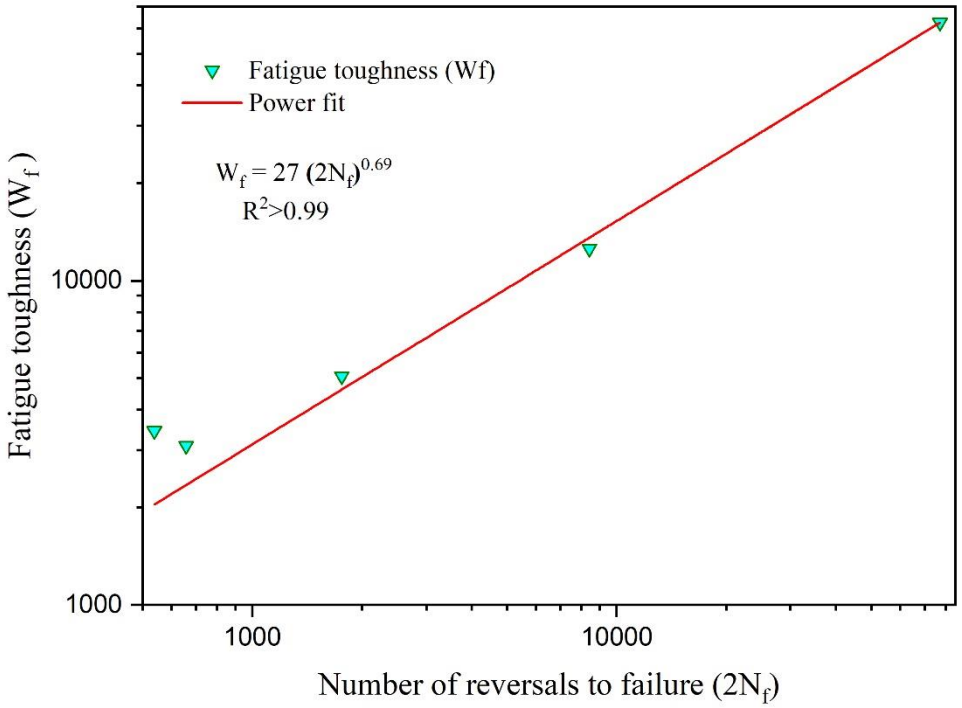

Fig. 4.25: Variation in fatigue toughness (W_f) values with the number of reversals to failure

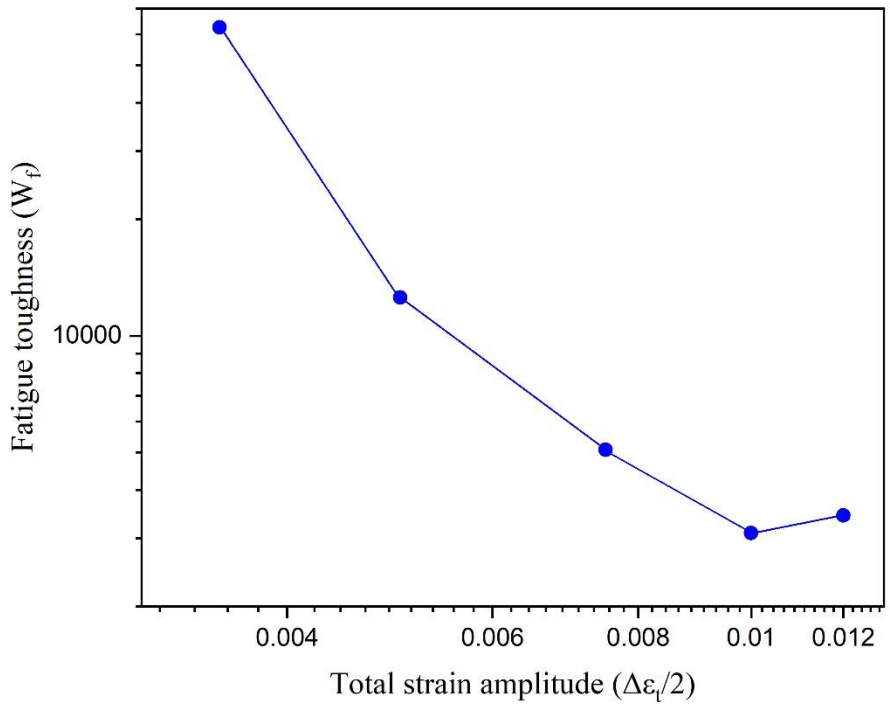

Fig 4.26: Changes in fatigue toughness (W_f) values with strain amplitude

The experimental $\Delta\bar{W}_p$ values for SS 304L have been compared with the values that are calculated on the basis of various semi-empirical relationships that have been established by Morrow and Halford [93], Levebre & Ellyn [68], and Quesnel [67]. The corresponding equations can be referred to from the Literature review section (Chapter **2**) of the present thesis.

Table 4.13 Comparison between strain energy density $\Delta\bar{W}_p$ values for SS 304L as predicted by different models

Strain amplitude $(\Delta\varepsilon_t/2)$	$\Delta\bar{W}_p$ (Experimental) (MJ/m^3)	Morrow and Halford	Quesnel	Levebre & Ellyn
0.0035	1.622	1.259	1.617	1.586
0.005	2.980	2.249	3.165	2.838
0.0075	5.767	4.243	5.905	5.449
0.01	9.408	6.746	9.089	8.882
0.012	12.779	9.036	11.722	12.17

It can be seen from **Table 4.13** that the Morrow and Halford model which is based on the assumption of masing behaviour, underpredicts the $\Delta\bar{W}_p$ value at all strain amplitudes. Whereas both the Quesnel and Levebre & Ellyn's model are in close agreement with the experimental values. It may be pointed out that the Levebre & Ellyn's model is applicable for non-masing materials, whereas Quesnel's[15] and Morrow's [13] semi analytical expressions are based on the premise of masing behavior.

4.5.13 Deformation induced martensite formation in fatigue tested specimens

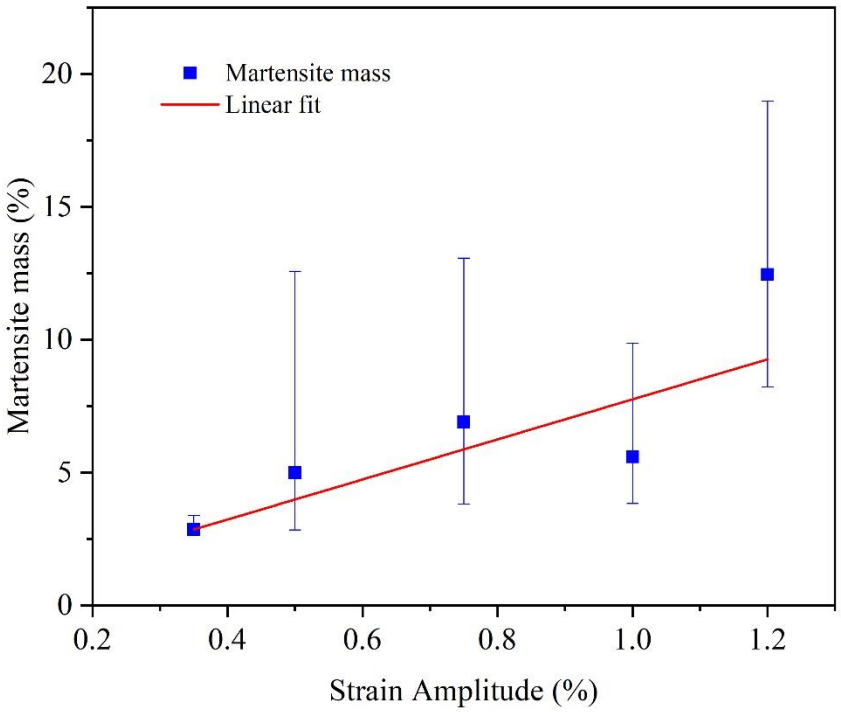

Fig 4.27: Variation of martensite mass fraction with strain amplitude

It is well known for strain induced martensitic transformations to occur in metastable austenitic stainless steels such as SS 304L. In the present study the average martensite mass fractions have been determined through ferritoscopic measurements made along the gauge length of each of the failed specimen which were cyclically strained at different strain amplitudes. The values obtained terms of the ferrite number (FN) have been converted to their corresponding mass fractions by multiplying a factor of 1.7 (Talonen's correlation factor).

A linear dependence of martensite phase fraction on the applied strain amplitude has been found from the present study. In **Fig 4.27** the average weight fractions have been represented by the square dots while the maximum and minimum values obtained from the set of measurements for each strain amplitude have been shown as vertical bars. A similar variation in martensite phase fraction with increasing strain amplitude was observed by Das et al. [94] based on his experimental results on 304LN stainless steel.

Sadough [95] had reported in his doctoral thesis that deformation induced martensite formation in SS 304L initially increased with strain amplitude but displayed a tendency to attain saturation at the later stages.
Several researchers [96,97] have independently found that there exists a critical cumulative plastic strain threshold which has to be overcome in order for martensitic transformation to occur at any given strain amplitude. Baudry and Pineau [97] have further shown that this critical cumulative plastic strain value decreases for higher strain amplitudes. This, in conjunction with

the fact that there is effectively very little plastic strain accumulation at lower strain amplitudes can successfully explain the general trend of increasing martensite phase fractions that are obtained at higher strain amplitudes, as depicted in **Fig 4.27**.

4.6 Fractography of fatigued specimens:

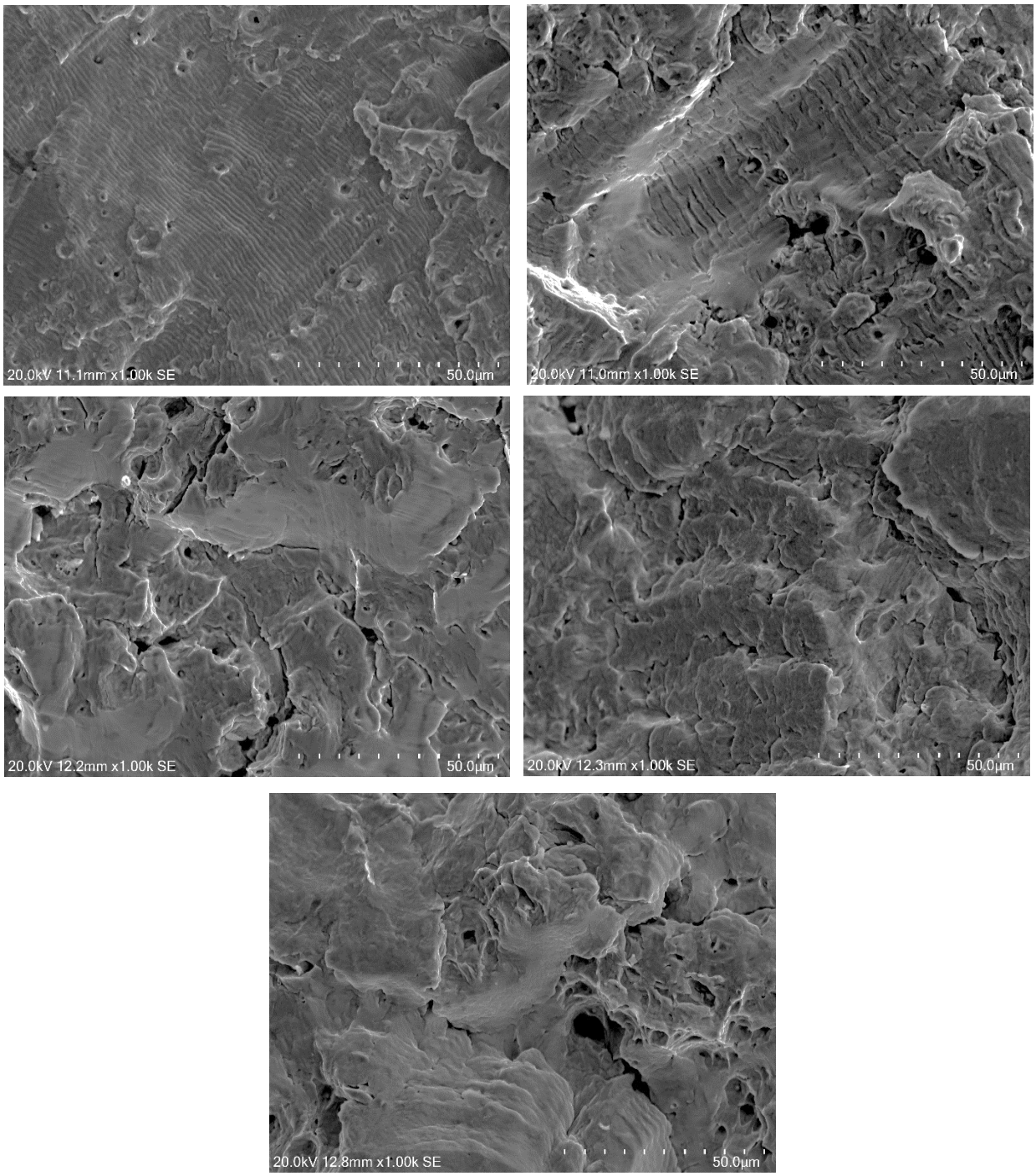

Fig 4.28: SEM micrographs of specimens failed by LCF at a strain amplitude of (**a)** ±0.35 % (**b)** ±0.5% (**c)** ± 0.75%, (**d)** ±1% (**e)** ±1.2%

The fracture morphologies of the fatigue tested 304L steel tested at various strain amplitudes indicate the presence of fatigue striations. The striations marks are clearly visible in the specimen micrographs for $\pm$0.35% and $\pm$0.5%, and although the striation spacing has not been measured in the current study, qualitative observation reveals that the striation spacing increases with increase in strain amplitude. It may noted , that the striation marks are no longer visible at high strain amplitudes of $\pm$1% and above, this finding is consistent with the observations made by Arpan et al [71] while studying the fracture morphology of 304LN stainless steel. In addition, transgranular cracks can be seen in the micrographs that indicate the brittle nature of fatigue fracture.

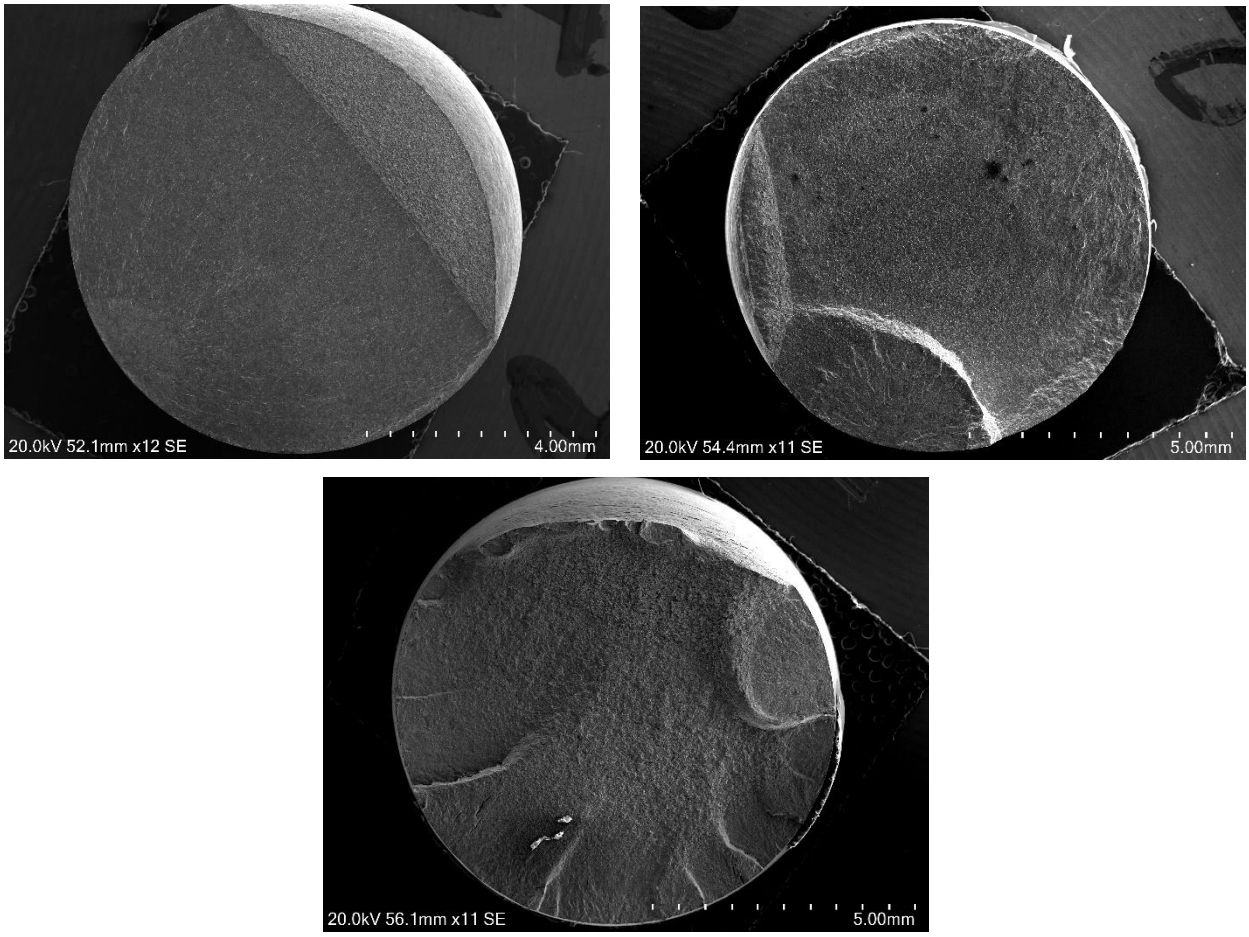

Fig 4.29: SEM macrographs of specimens failed by LCF at a strain amplitude of (**a)** $\pm$0.35 % (**b)** $\pm$0.5% (**c)**$\pm$1%

A comparison between the specimen macrographs in **Fig 4.29** further reveals that the number of crack initiation sites increase with increasing strain amplitude, which is consistent with the fact that the fatigue life of 304L stainless steel is significantly reduced at higher strain amplitudes.

4.7 Corrosion properties of SS 304L

4.7.1 Monotonically deformed samples:

Immersion type pitting corrosion tests were carried out for the present material after performing interrupted tensile tests in which the material was monotonically loaded at a constant strain rate of 10^{-3} s^{-1} upto a certain strain value before being unloaded.

3.5wt.% standard NaCl solution was used as an electrolyte for carrying out the tests, and all tests were performed under potentiodynamic polarisation mode.

The purpose of these tests was to determine the corrosion properties of SS 304L and to gauge the influence of deformation on the variation of these properties.

The corrosion properties for each of the deformed specimen along with the base sample are listed in **Table 4.14**

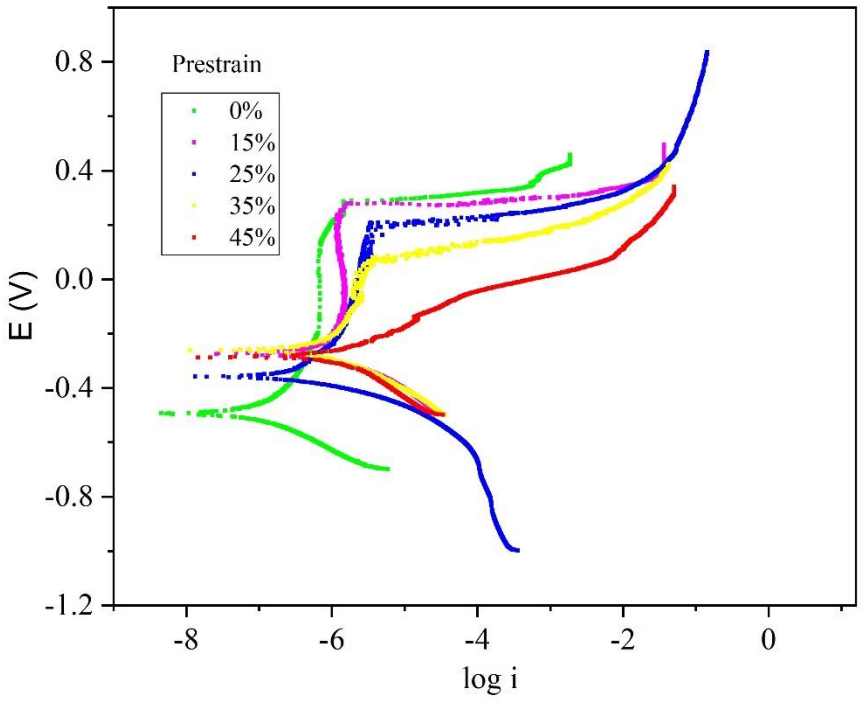

Fig 4.30 Tafel plots for SS 304L under different conditions of prestrain

Table 4.14: Corrosion properties of SS 304L under various prestrain conditions

Sample condition	E_{corr} (V)	i_{corr} (μA/cm^2)	Corrosion rate (mm/yr)	β_a (V/dec)	$\lvert\beta_c\rvert$ (V/dec)	E_{pit} (V)
Base sample (Solution annealed)	−0.491	0.029	0.00030	0.03	0.05	0.287
16.18% prestrain	−0.271	0.203	0.00241	0.05	0.04	0.279
28.4% prestrain	−0.357	0.293	0.00306	0.19	0.03	0.208

41.9% prestrain	−0.270	1.137	0.0118	0.12	0.13	0.067
56.8% prestrain	−0.283	1.47	0.0174	0.09	0.18	−0.05

Fig 4.30 shows the anodic polarization curves of SS 304L obtained by carrying out potentiodynamic linear polarization tests with the help of a potentiostat.
The E values were measured with respect to a standard calomel electrode, and i is the current density in A/cm^2. The effect of tensile deformation on the corrosion properties can be seen from **Table 4.14** Increasing the prestrain value or deformation applied prior to the test had an effect of decreasing the pitting potential (E_{pit}) of the steel. The corrosion rate for the deformed samples were one to two orders of magnitude higher in comparison to the base sample, indicating that plastic deformation had an effect of decreasing the corrosion resistance of the steel. The range of passivity also decreased considerably for the deformed samples. The region of passivity was practically absent for the sample with the highest prestrain value (56.8%).
The corrosion rates in mm/yr were calculated using the formula r =$0.00327\frac{aj}{nD}$, where $\frac{a}{n}$ is the equivalent weight of the steel calculated to be 25.25, j is the current density and D is the average density of the steel calculated to be 7.9g/cm^3. **Fig 4.31** illustrates the procedure for calculating the corrosion potential, the corrosion current density and the pitting potential values from the polarization curve. The linear portions of the cathodic and anodic branches were approximated by straight lines that were extrapolated until they intersected at a point (tafel extrapolation). The x and y coordinates of this point corresponds to the values of i_{corr} and E_{corr} respectively. In most cases the linearity for the anodic branch could not be discerned from the experimental curve and the anodic curve was generated from the cathodic data by plugging in the values of $i_{c,applied}$ and i_c into the equation $i_c - i_{c,applied} = i_a$ for E values near E_{corr}. Here $i_{c,applied}$ represents the applied current density which was directly obtained from the experimental curve and i_c and i_a denote the cathodic and anodic current densities that were obtained from the approximated straight lines for the corresponding branches.

Pitting potential values were obtained from the point at which the current densities increased rapidly after the breakdown of passivity. This portion appears as a near horizontal straight line in **Fig 4.31** For the 56.8% strained specimen no distinct pitting potential value could be ascertained from its polarization curve and the potential value at which the current density exceeded 80 μA/cm^2 was recorded as the pitting potential.
The β_a and β_c values are the slopes of the linear portions of the anodic and cathodic branches that have been approximated by straight lines.

The variation in pitting potential values with the percentage of prestrain has been shown in **Fig 4.32** The lowering of pitting potential values in SS 304L with increase in percentage of prior deformation increases the vulnerability of the steel to localised corrosion attack. Corrosion studies on 316L austenitic stainless steels by Kamachi [98] have shown that the pitting potential initially increases with the percentage of cold work upto 20% but starts diminishing thereafter .They attributed the initial increase of Epit to the presence of nitrogen which increases the friction stress of the material making it energetically favourable for deformation twins to form. The present observations for SS 304L in the current study can be supported by the fact that strain induced martensite formation, generation of surface residual stresses, and an overall increase in dislocation density with deformation significantly alters the localised corrosion resistance of the steel by increasing the number of active sites on the surface that undergo anodic dissolution to form pits. The effect of cold work on stainless steels has also been studied by other researchers [99] who found that both the average pit size and the number density of

pits increased with the increase in percentage of deformation indicating a greater susceptibility of the steel to undergo localised corrosion in a cold worked condition.

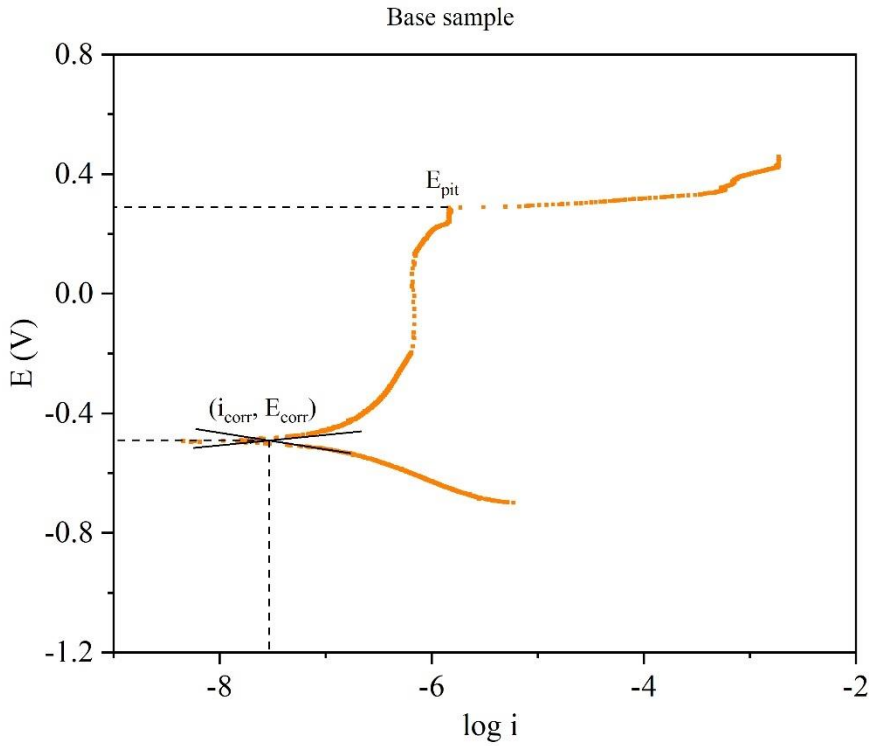

Fig 4.31 Procedure for determining E_{corr}, i_{corr}, and E_{pit} values from the polarization curves of SS 304L

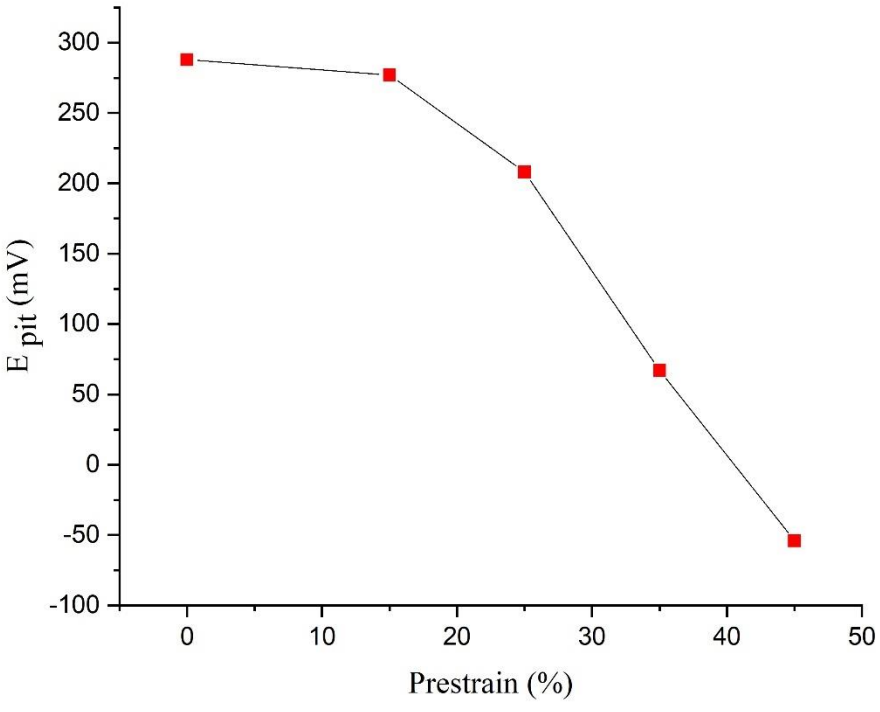

Fig 4.32 Variation in pitting potential values of 304L steel with different levels of prestrain

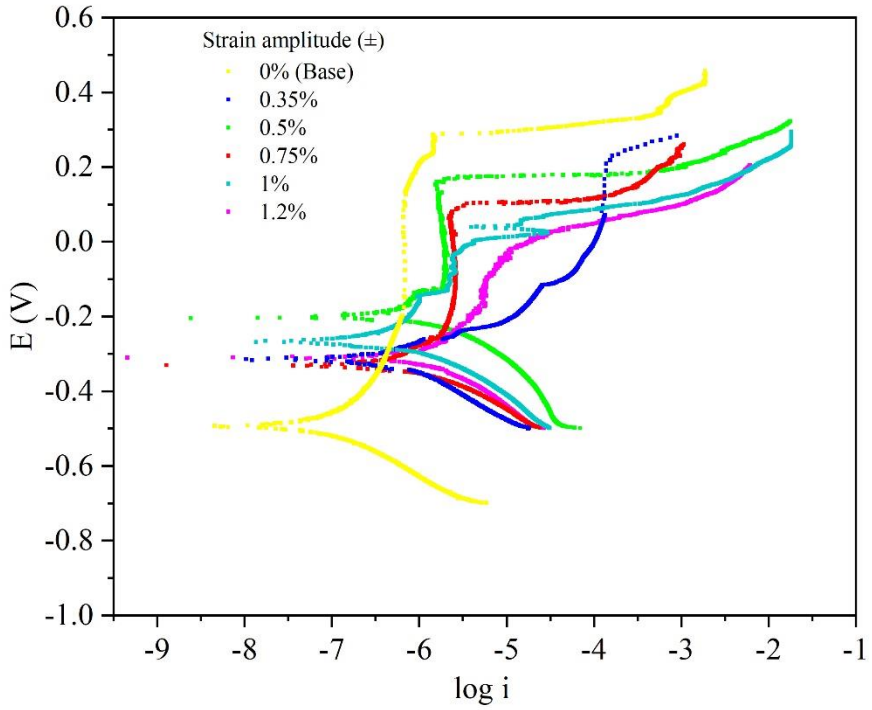

Fig 4.33 Tafel plots of SS 304L specimen cycled at different strain amplitudes

4.7.2 Cyclically deformed samples:

Immersion corrosion tests were performed on stainless steel samples that were fatigue tested at different strain amplitudes under strain control. The purpose of these tests were to determine the effect of strain amplitude on the corrosion properties of SS 304L.

Table 4.15: Corrosion properties of cyclically deformed samples

Sample condition	E_{corr} (V)	i_{corr} (μA/cm^2)	Corrosion rate (mm/yr)	β_a (V/dec)	$\lvert\beta_c\rvert$ (V/dec)	E_{pit} (V)
Base	−0.491	0.029	0.00030	0.03	0.05	0.287
0.35%	−0.308	0.572	0.00598	0.4	0.13	0.230
0.5%	−0.200	0.347	0.00363	0.08	0.03	0.159
0.75%	−0.332	0.326	0.00341	0.10	0.04	0.103
1%	−0.274	1.035	0.0108	0.07	0.13	0.058
1.2%	−0.306	1.256	0.0131	0.2	0.04	0.011

The data for the cyclically deformed samples clearly shows that the pitting potential of the steel decreases with an increase in strain amplitude. This decreasing resistance to pitting corrosion may be due to the increase in martensite fraction at higher strain amplitudes. According to Fang et al. [100] the corrosion potential of the martensite phase is more negative than that of austenite, due to which it undergoes selective corrosion when exposed to an aggressive environment, thus ultimately leading to a reduction in both the general and the pitting corrosion resistance of the steel.

The martensitic transformation is a displacive transformation which is accompanied by large plastic strains, along with the generation of dislocations. Deformation induced martensite often

occurs in the form of laths having high dislocation densities due to which they become preferred sites for Cl^- ions to get adsorbed by the protective oxide film at the surface. Upon adsorption, complex compounds and adsorbates are formed that reduce the effectiveness of the oxide film ultimately causing local dissolution and pit initiation.

Another plausible argument is that the passive oxide film which forms during the course of the test loses its efficacy or adherence due to the intrusions and extrusions that are created at the surface of the specimen during cyclic straining. This is in line with the fact that the corrosion resistance deteriorates if the surface roughness of the specimen is high, which is especially true for the fatigue tested specimens since fatigue damage initiates at the surface.

The passive region of the polarization curve of the sample which was cycled at a strain amplitude ±1% shows fluctuations or current transients. These can be attributed to the formation of metastable pits which were initiated at potential values lower than the critical pitting potential but were subsequently repassivated before they could propagate.

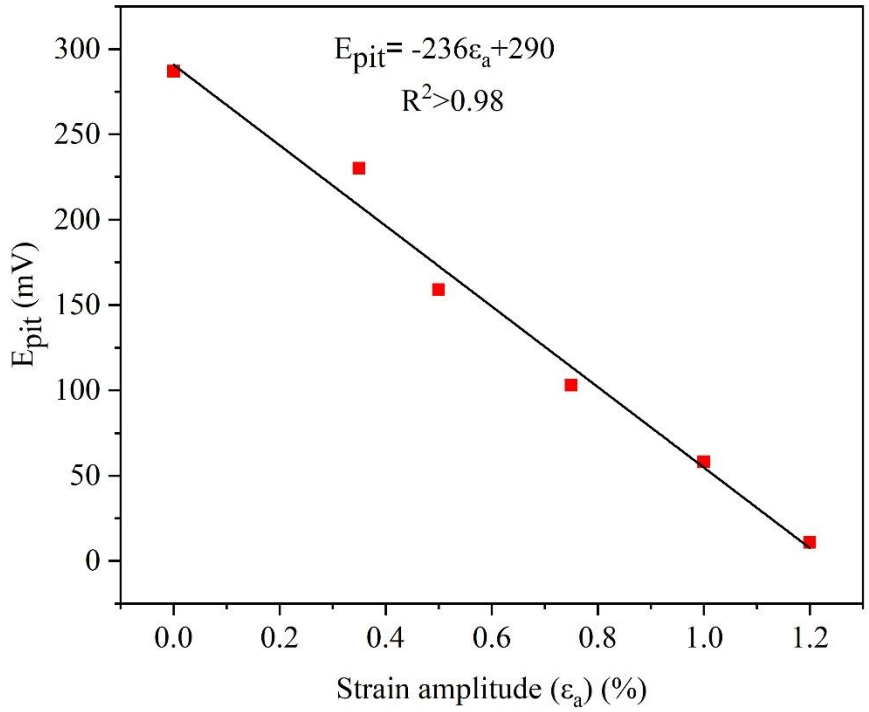

Fig 4.34 Variation of pitting potential values with different strain amplitude levels

Fig 4.35 shows that the pitting potential values for the fatigue tested specimen decrease with increasing strain amplitude in a linear fashion.
Pitting potential values obtained for various prestrain levels have been plotted against the martensite volume fraction formed at that strain level.
A distinct exponential trend has been observed for both the precycled and prestrained specimens which clearly highlight that martensite formation negatively impacts the resistance against pitting corrosion in 304L stainless steels.
Furthermore, the similar nature of variation in both cases suggest that Epit is not affected by the mode of deformation but only depends upon the amount of martensite being formed at that

strain level. A closer look at the exponent and coefficient values which appear in the equations describing the variation of pitting potential with the percentage of martensite reveal that they almost remained unchanged despite the difference in which prior deformation was applied, which further strengthens the above argument.

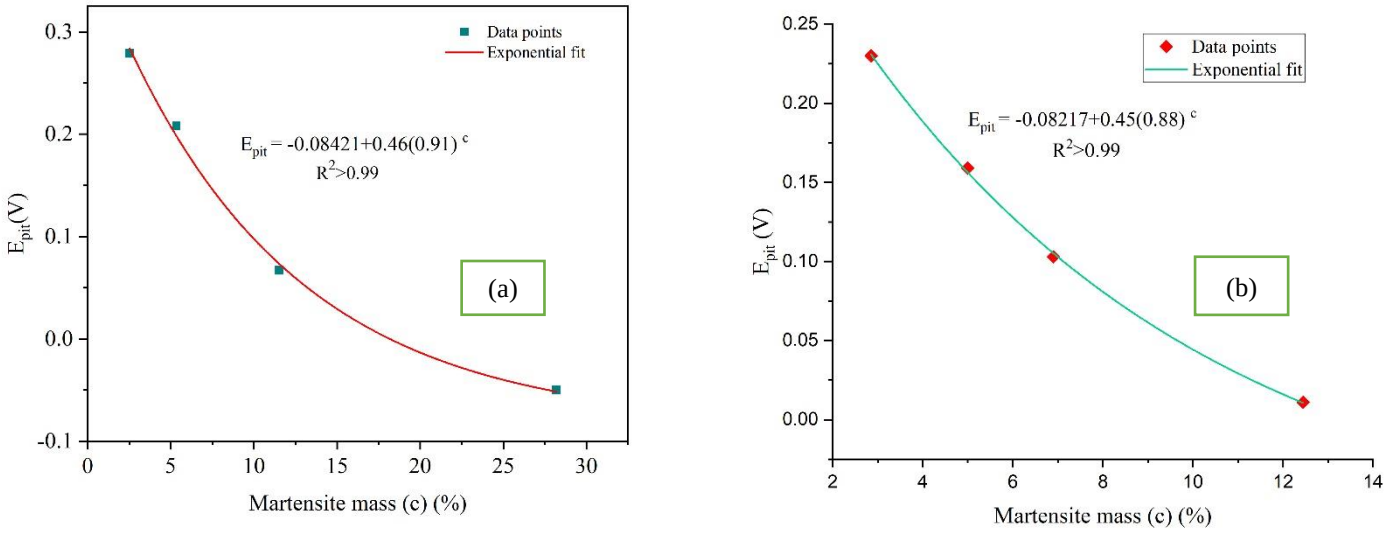

Fig 4.35 Variation in pitting potential values with martensite mass fraction for **a)** monotonically deformed samples **b)** cyclically deformed samples

Chapter 5

Conclusion

Based on the results of the experimental work on 304L Stainless Steels that have been carried out ,the following key findings may be highlighted and the following conclusions may be drawn:

1. Tensile test parameters such as the UTS and %EL of the specimen decreased slightly at the higher strain rate, whereas there was an increase in the YS value. The decrease in UTS value was found to be the direct consequence of thermal softening as a result of adiabatic heating of the material, and the formation of a lesser amount of martensite, which decreased the work hardening capability of the steel.
2. All the work hardening models which were analysed in this study predicted multi-stage work hardening behaviour of the steel, with different deformation mechanisms and microstructural changes governing each stage. Planar slip was found to dominate at low strain levels whereas activation of secondary slip systems and cross-slip was observed at higher strain values.
There was an increase in the mass fraction of Deformation Induced Martensite (DIM) with monotonic tensile deformation, with higher mass fractions being obtained at higher strain values.
3. The cyclic stress response curves for SS 304L showed significant secondary cyclic hardening at the later stages for strain amplitude levels of $\pm 0.5\%$ and above. The degree of secondary hardening was directly correlated with the amount of martensite phase being formed. The primary hardening stage which was present for all the strain amplitudes was followed by a stage of stable stress response which could be observed at the intermediate strain amplitudes ($\pm 0.5\%$ to $\pm 0.35\%$). Cyclic softening was only observed for the strain amplitude of $\pm 0.35\%$, whereas at $\pm 1.2\%$ continuous hardening occurred.
4. The martensite mass fractions were found to increase in a linear fashion with increasing strain amplitudes
5. The stress-strain hysteresis loops displayed a non-masing behaviour for the multi-specimen low cycle fatigue tests that were carried out in the present study, with the degree of deviation from masing behaviour increasing with strain amplitude.
6. A bilinear cyclic stress strain curve was obtained for the present material, which could be attributed to substantial martensite formation at strain amplitudes of $\pm 0.5\%$ and above.
7. The cyclic plastic strain energy almost remained constant throughout the fatigue life of the material for all the strain amplitudes except at $\pm 1.2\%$ where it displayed a sudden increase.
8. The pitting potentials for the pre-strained samples were found to decrease with increasing values of pre-strain which was applied prior to performing the immersion corrosion tests. The corrosion rates for the strained samples were found to be 10 to 100 fold higher than the unstrained samples. Indicating that deformation and martensite formation had a negative impact on the corrosion resistance of the material.
9. A similar observation was made for the pre-cycled specimens were the pitting potential values decreased with strain amplitude. Interestingly distinct linear pattern was obtained by plotting the pitting potential values against the applied strain amplitude.

Chapter 6

Suggestions for future work

1. Electron Backscattered Diffraction**(EBSD)** studies may be carried out in order to determine the average grain size and the grain size distribution of the base samples.

2. Transmission Electron Microscopy **(TEM)** of the samples can be carried out in order to understand the changes in dislocation structures and dislocation arrangements with progressive deformation of the material. Orientation of the martensite habit planes may also be determined from the SAD patterns obtained from TEM.

3. X Ray Diffraction of the monotonically, cyclically deformed samples can be carried out in order to predict or quantify martensite volume fractions with greater accuracy. Presence of intermediate phases like ε-martensite can also detected with the help of this technique.

4. Asymmetric stress cycling may be carried out in order to study the ratcheting behavior in 304 L stainless steels.

5. Electrochemical Impedance Spectroscopy **(EIS)** may be performed to determine the corrosion resistance of the deformed samples.

6. High temperature tensile tests may be performed in order to study the DSA phenomenon.

References:

[1] Handbook of Stainless Steels (Outokumpu)

[2] SOLOMON H. D., LEVINSON L. M. "Mössbauer effect study of 475ºC embrittlement of duplex and ferritic stainless steels", Acta Metallurgica, vol. 26, no. 3, p. 429-442, 1978.

[3] Welding Metallurgy and Weldability of Stainless Steels (John C. Lippold, Damien J. Kotecki)

[4] A. Pardo *, M.C. Merino, A.E. Coy, F. Viejo, M. Carboneras, R. Arrabal: *Influence of Ti, C and N concentration on the intergranular corrosion behaviour of AISI 316 Ti and 321 stainless steels*

[5] Wasnik DN, Kain V, Samajdar I, Verlinden B, De PK. Acta Mater 2002;50:4587

[6] Min KS, Nam SW. J Nucl Mater 2003;322:91.

[7] Hall EL, Briant CL. Metall Trans A 1984;15:793

[8] Hall EO, Algie SH. The sigma phase. Metallurgical reviews. 1966; 11:61-88.

[9] Zucato, I., Moreira, M. C., Machado, I. F., Lebrão, S. M. G., (2002). Microstrucutural Characterization and the effect of phase transformations on toughness of the UNS S31803 duplex stainless steel aged treated at 850ºC. *Materials Research*, 5, 385-389

[10] E. C. Bain and W. E. Griffiths, Trans. Amer. Inst. Alin. Met. Eng., 1927, 75, 166

[11] Comparative study on sigma phase precipitation of three types of stainless steels: austenitic, superferritic and duplex D. M. E. Villanueva, F. C. P. Junior, R. L. Plaut and A. F. Padilha*

[12] *Steels: Microstructure and Properties* (Harry Bhadeshia, Robert Honeycombe)

[13] Talha, M., Behera, C. K., Sinha, O. P., (2013). A review on nickel-free nitrogen containing austenitic stainless steels for biomedical applications. *Materials Science and Engineering C*., 33, 3563–3575

[14] Tofaute, W., Schottky, H., (1940). Zur Frage des Ersatzes von Nickel in korrosionsbeständigen Chrom-Nickel-Legierungen durch Stickstoff (*Replacement of nickel in austenitic chromium-nickel steels with nitrogen*) Technische Mitteilungen Krupp, 3, 103-110

[15] Speidel, M. O., (1990). Properties of high nitrogen steels. In: Stein, G. and Witulski, H., ed High Nitrogen Steels 90. Verlag Stahleisen, Düsseldorf. 128-131

[16] Reed, R. P., (1989). Nitrogen in austenitic stainless steels. *The Journal of the Minerals, Metals and Materials Society*. 41, 16-21

[17] Mehran Maalekian (2007) The Effects of Alloying Elements on Steels (I).*TU Graz*

[18] An Introduction to Metallurgy, Cottrell, Sir Alan

[19] Copson, H.R. 1959. *Physical Metallurgy of Stress-Corrosion Fracture, Interscience*, New York, p. 126

[20] Floreen, S., and Hayden, H.W. 1968.*Transactions of the American Society for metals*, 61:489-499

[21] R. J. BRIGHAM, E. W. TOZER; Effect of Alloying Additions on the Pitting Resistance of 18% Cr Austenitic Stainless Steel. *CORROSION* 1 May 1974; 30 (5): 161–166.

[22] *Effects of alloying elements on σ phase precipitation in δ-γ duplex phase stainless steels* Y. Maehara, Y. Ohmori, J. Murayama, N. Fujino, and T. Kunitake

[23] J.W. Simmons, *Overview: high-nitrogen alloying of stainless steels*

[24] *Austenitic Stainless Steels: Microstructure and Mechanical properties* (P. Marshall)

[25] Schaeffler, A.L. 1949.Constitution diagram for stainless steel weld metal *Metal Progress*, 56(11): 680-680B

[26] Pickering, F.B., ***International Metals Reviews,*** 1976, **p.** 227

[27] Irvine K.J. et. al., *Journal of Iron* & *Steel Institute*, 207, 1969, **p.** 1017

[28] F.B. Pickering, Physical Metallurgy and The Design of Steels, Applied Science Publishers, 1978.

[29] T. Angel, J. Iron Steel Inst. 177 (1) (1954).

[30] G. E. Dieter and D. J. Bacon, *Mechanical metallurgy* vol. 3: McGraw-hill New York, 1986

[31] De, A.K., Speer, J.G., Matlock, D.K. *et al.* Deformation-induced phase transformation and strain hardening in type 304 austenitic stainless steel. *Metall Mater Trans A* **37**, 1875–1886 (2006)

[32] C.J. Guntner and R.P. Reed: Trans. ASM, 1962, vol. 55, pp. 399-419

[33] Chengsi Zheng, Wangwei Yu, *Effect of low-temperature on mechanical behaviour for an AISI 304 austenitic stainless steel, Materials Science and Engineering: A, Volume 710,2018*

[34] Muhamed, G.A.; Gündüz, S.; Erden, M.A.; Taştemur, D. Dynamic Strain Aging Behaviour in AISI 316L Austenitic Stainless Steel under As-Received and As-Welded Conditions. *Metals* **2017**, *7*, 362.

[35] A.H. Cottrell, Theory of dislocations ,Progress in Metal Physics, Volume 4,1953

[36] J.P. Bressanelli and A. Moskowitz: *Trans. ASM*, 1966, vol. 59, pp. 223-39

[37] van Tol, R.T., Kim, J.K., Zhao, L. *et al.* α′-Martensite formation in deep-drawn Mn-based TWIP steel. *J Mater Sci* **47**, 4845–4850 (2012)

[38] J.W. Brooks, M.H. Loretto, and R.E. Smallman: *Acta Metall.*, 1979, vol. 27, pp. 1839-47

[39] S.S. Hecker, M.G. Stout, K.P. Staudhammer, and J.L. Smith: *Metall.Trans. A*, 1982, vol. 13A, pp. 619-26.

[40] Talonen, J., Hänninen, H., Nenonen, P. *et al.* Effect of strain rate on the strain-induced $\gamma \rightarrow \alpha'$-martensite transformation and mechanical properties of austenitic stainless steels. *Metall Mater Trans A* **36**, 421–432 (2005)

[41] Iwamoto T, Tsuta T, Tomita Y (1998) Int J Mech Sci 40:173

[42] S.G.S. Raman, K.A. Padmanabhan, Mat. Sci. and Tech. 10 (1994) 614–620

[43] J. H. Hollomon, "Tensile deformation," *Aime Trans*, vol. 12, pp. 1-22, 1945

[44] J. R. Low and F Garofalo: *Proc. Soc. Stress Anal.*, 1947, vol. 4 p. 16

[45] Ludwigson, D.C. Modified stress-strain relation for FCC metals and alloys. *Metall Trans* **2**, 2825–2828 (1971)

[46] Singh, K. K. (2004). Strain hardening behaviour of 316L austenitic stainless steel. *Materials science and technology*, *20*(9), 1134-1142.

[47] P. Ludwik, "Elemente der Technologischen Mechanik, Julius Springer, Berlin," *CrossRef Google Scholar*, p. 32, 1909

[48] Haasen, P. (1958). Plastic deformation of nickel single crystals at low temperatures. *The Philosophical Magazine: A Journal of Theoretical Experimental and Applied Physics*

[49] Mader, Siegfried, Alfred Seeger, and Christoph Leitz. "Work hardening and dislocation arrangement of FCC single crystals. I. Plastic deformation and slip line studies of nickel single crystals." *Journal of Applied Physics* 34.11 (1963): 3368-3375

[50] Kocks, U. F. and Heinrich Mecking. “Physics and phenomenology of strain hardening: the FCC case.” *Progress in Materials Science* 48 (2003): 171-273.

[51] Rollett AD, Kocks UF, Doherthy RD. In: Sachdev AK, Embury JD, editors. Formability and metallurgical structure. The Metall. Society; 1987. p. 211

[52] Gurson, A.L., 1977. Continuum theory of ductile rupture by void nucleation and growth: Part I – Yield criteria and flow rules for porous ductile media. ASME Journal of Engineering Materials and Technology 99, 1–15.

[53] Anderson, T.L., 1995. Fracture Mechanics: Fundamentals and Applications, third ed. CRC Press, Boca Raton, New York. 265

[54] Das, Arpan, et al. "Correspondence of fracture surface features with mechanical properties in 304LN stainless steel." *Materials Science and Engineering: A* 496.1-2 (2008): 98-105.

[55] Paul, S. K., Sivaprasad, S., Dhar, S., & Tarafder, S. (2010). Cyclic plastic deformation and cyclic hardening/softening behavior in 304LN stainless steel. *Theoretical and Applied Fracture Mechanics*, *54*(1), 63-70.

[56] Xingfei Xie, Dong Ning, Jian Sun, *Strain-controlled fatigue behavior of cold-drawn type 316 austenitic stainless steel at room temperature*, Materials Characterization, Volume 120 ,2016

[57] Ye, Duyi & Matsuoka, Saburo & Nagashima, Noburo & Suzuki, Naoyuki. (2006). The low-cycle fatigue, deformation and final fracture behaviour of an austenitic stainless steel. Materials Science and Engineering: A. 415. 104-117.

[58] Dey, Rima & Tarafder, S. & Sivaprasad, S (2016). Influence of phase transformation due to temperature on cyclic plastic deformation in 304LN stainless steel. International Journal of Fatigue.

[59] Smith, R. W., Hirschberg, M. H., & Manson, S. S. (1963). *Fatigue behavior of materials under strain cycling in low and intermediate life range*

[60] O. Basquin, "The exponential law of endurance tests," in *Proc Astm*, 1910, pp. 625-630

[61] L. F. Coffin Jr, "A study of the effects of cyclic thermal stresses on a ductile metal," *trans. ASME*, vol. 76, pp. 931-950, 1954

[62] S. S. Manson, "Behavior of materials under conditions of thermal stress," 1954

[63] Sivaprasad, S. & Paul, Surajit & Das, Arpan & Narasaiah, Nayaka & Tarafder, S.. (2010). Cyclic plastic behaviour of primary heat transport piping materials: Influence of loading schemes on hysteresis loop. Materials Science and Engineering A. 6858-6869.

[64] S.G.S. Raman, K.A. Padmanabhan, Int. J. Fatigue 18 (1996) 71–79

[65] Sanjeev Singh Yadav, Samir Chandra Roy, J. Veerababu, Sunil Goyal,
Type-I to Type-II non-Masing behavior of 304L SS under low cycle fatigue: Material's internal changes, International Journal of Fatigue,Volume 175,2023

[66] Feltner, C. E., and Morrow, J. D. (March 1, 1961). "Microplastic Strain Hysteresis Energy as a Criterion for Fatigue Fracture." ASME. *J. Basic Eng*. March 1961; 83(1): 15–22

[67] D.J Quesnel, M Meshii, *The response of high-strength low alloy steel to cyclic plastic deformation, Materials Science and Engineering*, Volume 30, Issue 3,1977, Pages 223-241

[68] Lefebvre, D., and F. Ellyin. "Cyclic response and inelastic strain energy in low cycle

[69] Hao, TONG Xiaoyan WANG Dejun XU. "Cyclic hysteresis energy of carbon and alloy steels." (1990)

[70] Li, D. M., W. J. Nam, and C. S. Lee. "A strain energy-based approach to the low-cycle fatigue damage mechanism in a high-strength spring steel." *Metallurgical and Materials Transactions A* 29 (1998): 1431-1439.

[71] Das, A., 2019. Cyclic plasticity induced transformation of austenitic stainless steels. Materials Characterization, 149, pp.1-25

[72] Jones, Denny A. "Principles and prevention." *Corrosion* 2 (1996): 168.

[73] May L. Martin, Petros Sofronis, Hydrogen-induced cracking and blistering in steels: A review, Journal of Natural Gas Science and Engineering, Volume 101,2022

[74] Wang, Yanfei, et al. "Ductility loss of hydrogen-charged and releasing 304L steel." *Frontiers of Mechanical Engineering* 8 (2013): 298-304.

[75] Ryuichiro Ebara,Corrosion fatigue crack initiation behavior of stainless steels, Procedia Engineering, Volume 2, Issue 1,2010,Pages 1297-1306

[76] Y.C. Lu, M.B. Ives, C.R. Clayton, Synergism of alloying elements and pitting corrosion resistance of stainless steels, Corrosion Science, Volume 35, Issues 1–4,1993

[77] N.D. Tomoshav, G.P. Chernova and O.N. Markova, Zashchita Metallov, **7(1971),** p. **104**

[78] Iris Alvarez-Armas,Suzanne Degallaix-Moreuil, *Duplex Stainless Steels*

[79] Hibner, E.L., Materials Protection and Performance, 26(3) (1987)

[80] A. Moskowitz et. **al** ASTM STP 418, American Society for Testing Materials, Philadelphia, USA, 1967. p. 3.

[81] B.E. Wilde, Corrosion, 42 (1986), p. 147

[82] A. Pardo, M.C. Merino, A.E. Coy, F. Viejo, M. Carboneras, R. Arrabal, *Influence of Ti, C and N concentration on the intergranular corrosion behaviour of AISI 316Ti and 321 stainless steels*, Acta Materialia, Volume 55, Issue 7,2007

[83] Kotecki D.J. 1989. Heat treatment of duplex stainless steel weld metals, *Welding Journal* 68(11): 431s-441s

[84] Lichtenfeld, J. A., Tyne, C. J. V. and Mataya, M. C. (2006) "Effect of strain rate on stress–strain behavior of alloy 309 and 304L austenitic stainless steel". Metall. Mater. Trans. A, 37, 147–161

[85] Feaugas X (1999) Acta Mater 47:3617

[86] Arpan Das, Soumitra Tarafder," *Experimental investigation on martensitic transformation and fracture morphologies of austenitic stainless steel*", International Journal of Plasticity, Volume 25, Issue 11,2009

[87] Basu, K., Das, M., Bhattacharjee, D., & Chakraborti, P. C. (2007). Effect of grain size on austenite stability and room temperature low cycle fatigue behaviour of solution annealed AISI 316LN austenitic stainless steel. *Materials Science and Technology*, *23*(11), 1278–1284.

[88] H. Mughrabi, H.J. Christ, ISIJ Int. 37 (1997) 1154–1169

[89] Keum-Oh Lee, Seong-Gu Hong, Soon-Bok Lee, "A new energy-based fatigue damage parameter in life prediction of high-temperature structural materials",Materials Science and Engineering: A,Volume 496, Issues 1–2,2008

[90] Halford, G. R. "The energy required for fatigue (Plastic strain hystersis energy required for fatigue in ferrous and nonferrous metals)." *Journal of materials* 1 (1966): 3-18.

[91] Morrow, J., and Tuler, F. R. (June 1, 1965). "Low Cycle Fatigue Evaluation of Inconel 713C and Waspaloy." ASME. *J. Basic Eng*. June 1965; 87(2): 275–289.

[92] H.J Kim, C.S Lee, S.H Park, D.H Shin. "Quantitative analysis on low cycle fatigue damage: a microstructural model for the prediction of fatigue life", Materials Science and Engineering: A,Volume 379

[93] J. Morrow, "Cyclic plastic strain energy and fatigue of metals," in *Internal friction, damping, and cyclic plasticity*, ed: ASTM International, 1965

[94] Das, A., Sivaprasad, S., Chakraborti, P. C., & Tarafder, S. (2011). Morphologies and characteristics of deformation induced martensite during low cycle fatigue behaviour of austenitic stainless steel. *Materials Science and Engineering: A*, *528*(27), 7909-7914.

[95] A. Sadough, Doctoral Thesis Universite Paris VI. 1985

[96] Colin, J., Fatemi, A., and Taheri, S. (February 18, 2010). "Fatigue Behavior of Stainless Steel 304L Including Strain Hardening, Prestraining, and Mean Stress Effects." ASME. *J. Eng. Mater. Technol*. April 2010; 132(2): 021008.

[97] G. Baudry, A. Pineau, “Influence of strain-induced martensitic transformation on the low-cycle fatigue behaviour of a stainless steel,” Materials Science and Engineering, Volume 28, Issue 2,1977

[98] Fang, Z., Wu, Y.S., Zhang, L. and Li, J. (1997), “Effect of deformation induced martensite on electrochemical behaviors of Type 304 stainless steel in the active state”, Corrosion Science and Protection Technology, Vol. 9 No. 1,p.75

[99] U. Kamachi Mudali, P. Shankar, S. Ningshen, R.K. Dayal, H.S. Khatak, Baldev Raj,On the pitting corrosion resistance of nitrogen alloyed cold worked austenitic stainless steels, Corrosion Science,Volume 44, Issue 10,2002,Pages 2183-2198

[100] Wu, Gaoxiang, and Preet M. Singh. "Effect of plastic deformation on pitting mechanism of SS304." *Metallurgical and Materials Transactions A* 50 (2019): 4750-4757.